Towards Hands-On Cooperative Control for Closed-Loop MRI-Guided Targeted Prostate Biopsy

by

Marek Wartenberg

A dissertation submitted to The Worcester Polytechnic Institute in conformity with the requirements for the degree of Doctor of Philosophy.

Worcester, Massachusetts

May, 2018

Approved by:

Prof. Gregory S. Fischer, Advisor
Worcester Polytechnic Institute

Prof. Zhi Li, Committee Member
Worcester Polytechnic Institute

Prof. Loris Fichera, Committee Member
Worcester Polytechnic Institute

Dr. Junichi Tokuda, Committee Member
Brigham and Women's Hospital, Harvard Medical School

Abstract

Intra-operative imaging is sometimes available to assist in needle biopsy, but typical open-loop insertion does not account for unmodeled needle deflection or target shift. Robotic closed-loop compensation for deviation from an initial straight-line trajectory can reduce the targeting error, using image-guidance for rotational control of an asymmetric bevel tip. When incorporating robotics into interventional procedures, often physician interaction with the patient is reduced and tactile feedback typically used for anatomical localization is lost. By pairing closed-loop trajectory compensation with a hands-on cooperatively controlled needle insertion, a physician's control of the procedure can be maintained while incorporating benefits of robotic accuracy.

This system was implemented on a needle placement robot suitable for use in the MR environment and capable of holding a typical clinically used biopsy gun. The robot consists of the 4-DoF clinical alignment base with a 2-DoF needle driver developed specifically for cooperatively controlled needle insertion with continuous closed-loop needle rotation. The robot and custom controller were tested for their effect on the Signal-to-Noise ratio (SNR) of MR images, and the results showed an

approximate drop of only 12% in signal when the robot was present, and no additional signal drop when the robot was powered on or moving.

During cooperative insertion, providing a haptic response upon detection of a membrane puncture event can provide additional sensory input for perceived needle localization relative to anatomy. A system for membrane puncture detection was developed using localization from preoperative MR images paired with real-time needle insertion force data. In-lab experiments were performed to evaluate the puncture detection algorithm during cooperatively controlled needle insertions into layered tissue phantoms, characterized to elicit needle forces typical in prostate interventions. It was found that puncture detection degrades at deeper membrane locations due to increased overall force seen on the needle, and that success of puncture detection at deeper membrane depths was more difficult when transitioning from a softer to stiffer material, than from stiffer to softer.

Using the same robotic system, a method of closed-loop active compensation for unmodeled deflection and target shift during targeted needle insertion was developed. This system is agnostic to the type of imaging providing needle tip and target information one-way downstream via the OpenIGTLink network communication protocol. This system was tested in-lab using perpendicularly mounted cameras to act as a proxy for multi-planar MR imaging. Under cooperatively controlled needle insertion performed by five test subjects, the system autonomously rotated a bevel tipped needle towards the direction of desired compensatory effort. These results showed no

statistically significant difference ($p > 0.05$) in the targeting accuracy between any user, with average targeting accuracy of $3.56mm_{rms}$.

The hardware and software subsystems were developed for clinical translation, and after each was validated in the lab they were integrated into the clinical environment to mimic the workflow of MRI-guided targeted biopsy. The full system was evaluated in-bore at Brigham and Womens Hospital, performing experiments to test puncture detection as well as a series of MR image-guided targeted needle insertions under cooperative control. Results showed successful membrane detection in each case except a single deep ($> 50mm$) membrane location and the overall targeting accuracy was $3.42mm_{rms}$, comparable to in-lab trials.

A cooperatively controlled robotic biopsy is more likely to gain acceptance by physicians over teleoperation due to maintaining proximity to the surgical site, but regulatory hurdles regarding robotic needle insertion still exist. The current robotic system framework is suitable for clinical use as it was fully validated in-bore, but some modifications could be made to increase the likelihood of regulatory approval. With these modifications the system could be ready for cadaver and pre-clinical animal trials within one year, and ready for in-human clinical trials in the next two to three years.

Acknowledgments

I would first like to thank my advisor Professor Gregory S. Fischer for taking me on as one of his PhD Students. I came from a background of biomedical engineering and Prof. Fischer's guidance through a full-systems approach to robotic development has left me a confident roboticist ready to contribute beyond this degree.

In addition, I'd like to thank the rest of my doctoral committee, Professor Loris Fichera, Professor Zhi Li and Dr. Junichi Tokuda for their reviews of this dissertation and guidance throughout my research. I would like to give a special thanks to Dr. Tokuda for his assistance in numerous clinical experiments at Brigham and Women's Hospital, several of which lasted very late into the night.

I would like to address the most sincere thanks to my lab mates in the Automation and Interventional Medicine Laboratory, especially Chris Nycz, Paulo Carvalho, Katie Gandomi and Joe Schornak. It is simply not enough to state how important your collaboration was in completion of this dissertation and how much I've learned from each of you.

I would like to thank Dr. Nirav Patel and Dr. Gang Li, graduates from the AIM

Lab ahead of me who taught me early on what is required of PhD level work, and who's own work much of my research was built upon.

From Brigham and Women's Hospital I would like to thank Dr. Pedro Moreira, Prof. Clare Tempany and Prof. Nobuhiko Hata for their insights and feedback throughout my research. In addition, I would like to thank Prof. Iulian Iordachita from Johns Hopkins University for his continued feedback on my research as well.

Finally I would like to thank the robotics engineering staff for all their help over the last several years, specifically Deborah Baron, Katherine Crighton, and Teresa Hemple.

This research was funded by NIH R01 CA111288, NIH R01 CA166379 and NIH R01 EB020667.

Dedication

This dissertation is dedicated to my parents. The opportunities you provided me and your continued support is what made completion of this work possible.

Contents

List of Tables

List of Figures

Acronyms

AAPM American Association of Physicists in Medicine

ABS Acrylonitrile Butadiene Styrene

ACR American College of Radiology

ASTM American Society for Testing and Materials

CAD Computer Aided Design

CPR Counts Per Revolution

CURV Continuous Rotation and Variable-curvature

CT Computed Tomography

DOF Degree of Freedom

DICOM Digital Imaging and Communications in Medicine

EMI Electromagnetic Interference

FBG Fiber Bragg Grating

FDA Food and Drug Administration

FPGA Field Programmable Gate Array

GUI Graphical User Interface

IGT Image-Guided Therapy

LPS Left-Posterior-Superior

MRI Magnetic Resonance Imaging

NEMA National Electronic Manufacturers Association

NIH National Institutes of Health

PID Proportional-Integral-Derivative

PSA Prostate-Specific Antigen

PVC Polyvinyl Chloride

RAS Right-Anterior-Superior

RF Radio Frequency

RMS Root Mean Square

RTOS Real-Time Operating System

SOM System on Module

SNR Signal-to-Noise Ratio

TRUS Transrectal Ultrasound

TSE Turbo Spin Echo

US Ultrasound

VF Virtual Fixture

Chapter 1

Introduction

1.1 Background and Motivation

Prostate cancer is the second leading cause of cancer related death among men in the United States [1]. It is estimated that there will be about 164,690 new cases of prostate cancer and about 29,430 deaths from prostate cancer in 2018 [2]. Furthermore, in the United States there are approximately 1 million biopsies each year, with twenty-percent of positive diagnoses requiring at least two biopsies [3], resulting in over 200,000 avoidable procedures in the United States alone. The prostate gland sits underneath of bladder and is part of the male reproductive system. Figure 1.1 shows the location of the prostate in the body as well as how it surrounds the urethra. [4].

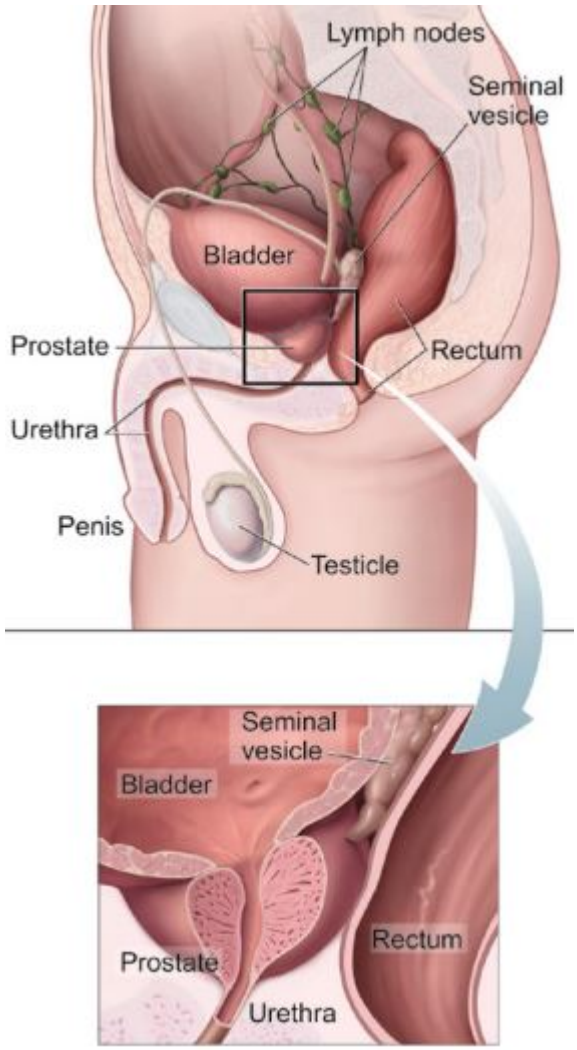

Figure 1.1: The male pelvic anatomy. Top: The location of the prostate within the male pelvic region, Bottom: a close up view of how the prostate surrounds the urethra. ©National Cancer Institute

A healthy prostate gland is approximately the size of a walnut. It is commonly split into three zones, the Peripheral Zone (PZ), the Central Zone (CZ) and the Transitional Zone (TZ) as seen in Fig. 1.2. There are distinct histological differences

between each zone and cancer affects these zones at different rates [5]. In a study of 1,703 men whose zonal origin of prostate tumor could be identified, Cohen et al. found a total of 2,494 tumors, with 1,589 (63.7%) in the PZ, 842 (33.8%) in the TZ and only 63 (2.5%) in the CZ [6].

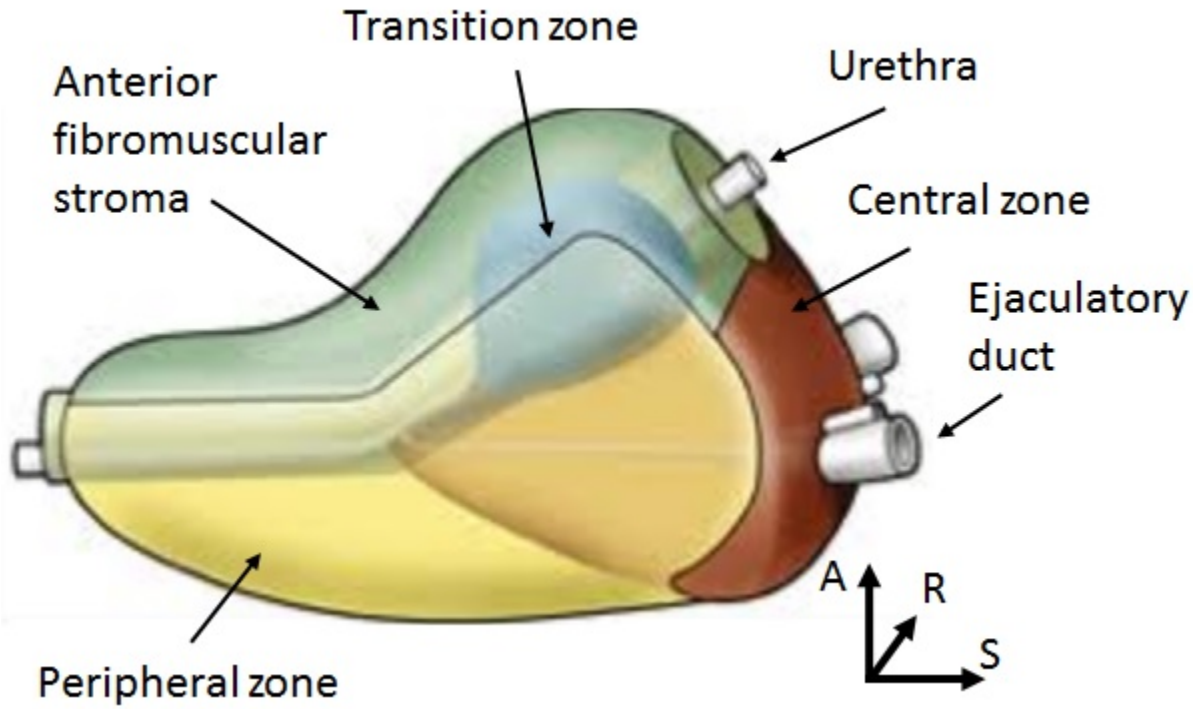

Figure 1.2: The anatomical zones of the prostate and their location relative to the urethra and ejaculatory duct. [7]

1.1.1 Using Image-Guidance in Prostate Cancer Diagnosis

Image-guidance in medicine is typically provided using Magnetic Resonance Imaging (MRI), Ultrasound (US) or Computed Tomography (CT), and can be used for pre-, intra-, or postoperative validation or in real-time to assist in interventional procedures. For typical diagnosis, Trans-Rectal Ultrasound (TRUS) has been used to facilitate sampling of between twelve and twenty biopsy cores in men with elevated levels of Prostate-Specific Antigen (PSA). Routine sampling in this manner is performed because low image quality limits the ability to target specific lesions [8, 9]. Furthermore, due to variable prostate size even twenty cores can be considered under sampled, which has led to both repeat biopsy procedures as well as under diagnosis of clinically significant prostate cancer [10]. Figure 1.3 is a diagram showing methodology for typical TRUS-guided biopsy using a template guide with $5mm$ spaced holes.

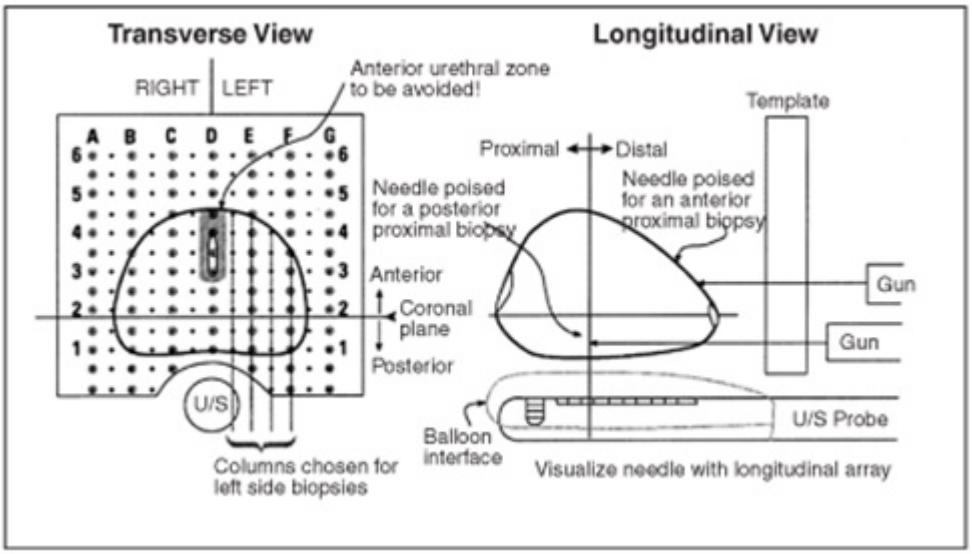

Figure 1.3: The typical approach to transrectal ultrasound guided prostate biopsy. A template guide with $5mm$ spaced holes is used to guide the needle to different locations with in the prostate ©Diagnostic Imaging

As opposed to TRUS, MRI provides much higher tissue contrast and the ability for multiparametric imaging such as diffusion tensor imaging (DTI), dynamic contrast enhanced (DCE) and blood oxygen level-dependent (BOLD). This leads to higher-quality images of suspicious lesions for targeted biopsy, without the ionizing radiation required in CT [11]. The use of MRI for Image-Guided Therapy (IGT) was pioneered in the 1990's, using information from medical imaging to improve treatment through intraoperative localization and control of surgical and interventional procedures [12–14].

Moving from TRUS to to MRI for prostate interventions, higher image quality allows for procedures with fewer needle insertions via direct lesion targeting. A study

using computer simulation to reconstruct models of prostatectomy specimens found that applying biopsy criteria for 12-core TRUS biopsy classified only 24% of clinically significant cancers as high risk, compared to 74% when using four targeted cores under typical MRI-guidance qualification. [15]. Figure 1.4 shows the difference in image quality of the pelvic region between ultrasound and MRI. When shifting to an MRI-guided targeted biopsy with manual insertion the same template guide with $5mm$ spaced holes can be used, with examples of manual needle insertion under MRI-guidance seen in [16–18]. Targeting techniques not using the template guide have also been employed and a clinical overview of MR-guided prostate biopsy is given in [19].

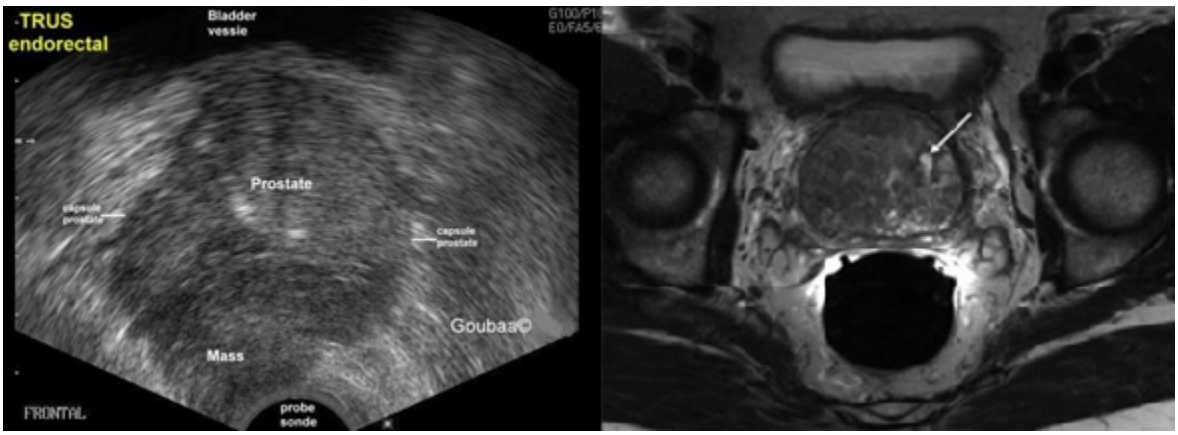

Figure 1.4: A comparison of TRUS and MRI images of the pelvic region. Left) TRUS ©Medical Echography, Right) MRI ©Indian Journal of Radiology and Imaging

Multi-modal imaging is also an option, such as MR-US fusion which combines the diagnostic accuracy of MR imaging for detecting suspicious lesions with the cost-effectiveness and familiarity of TRUS biopsy [20]. In a study of 500 men, randomized

between targeted biopsy using MR-US fusion and the TRUS-guided approach, it was found that the targeted biopsy was superior to the standard TRUS approach for cancer detection in men at clinical risk of prostate cancer who had not undergone biopsy previously [21]. Interestingly, Filson et al. described the importance of systematic biopsy in addition to targeting suspicious lesions under MR-US fusion. In a study of 463 men, they showed 26% of patients had cancers outside the targeted region that were found in systematic biopsy [22]. Overall, outcomes of MR-US fusion biopsy are superior to standard TRUS approach, with studies showing the most powerful predictor of significant cancer was the degree of suspicion on MRI images [23, 24]. There may be an added benefit to procedures under real-time MRI over MR-US fusion, as this technique allows for intraoperative deformable registration, which is not possible in the MR-US fusion case where only preoperative MR images are used.

1.1.2 Manual MRI-Guided Targeted Biopsy

The procedure used in a manual insertion targeted MRI-guided biopsy is presented as a baseline in which to compare the proposed workflow using a robotic system for the procedure under cooperative control. The methods are described below, with a complete description of the clinical study provided by Penzkofer et al. [25].

To begin, a set of preoperative images taken days prior to the procedure are reviewed by the radiologist and the locations of suspicious lesions are marked. On the day of the procedure the patient is placed in the supine position with legs elevated for

transperineal access. Other methods of biopsy have been explored such as transrectal [26–29] and transgluteal [30, 31], but a transperineal biopsy mimics the preoperative imaging pose of the patient for better intraoperative registration, and provides better access to the peripheral zone where most cancers are found [7].

The skin was prepared and draped then the template needle guide was introduced. A registration scan was taken to located the template guide in the scanner coordinates and nonrigid registration maps the location of predetermined suspicious lesions onto the patient's current pose within the MRI. During the procedure a target is selected, the correct $5mm$ spaced hole in the template is used for alignment and the needle is inserted to the target depth. A confirmation image is taken and if the needle tip has reached the target with sufficient accuracy a biopsy is taken and the next target is selected. Figure 1.5 shows the in-bore view during a manual needle insertion targeted MRI-guided biopsy.

Figure 1.5: An in-bore view during manual insertion MRI-guided targeted biopsy. The white arrows show the patient table and foot rests while the template guide is shown with the white arrowhead and the inserted needle with the black arrowhead [25]

1.1.3 Robotic Systems in the MRI-Environment

Despite the benefits of directly targeting lesions under MRI, adoption of MRI-guided needle interventions remains limited. This is primarily due to procedural cost, high clinical demand of scanners, ergonomics of performing these procedures inside the MR bore (Typically $55 - 70cm$ diameter), and in cases such as the presented work

there are technical issues with electromagnetic interference (EMI) of mechatronic systems within the MRI environment. Regarding the placement of such items within the high magnetic field (up to 3 Tesla) of the MRI, Fig. 1.6 describes the American Society for Testing and Materials (ASTM) classification [32] for three types of devices as:

- **MR Safe** The device or implant is completely nonmagnetic, nonelectrically conductive, and nonradiofrequency reactive, therefore eliminating all the primary potential risks during MRI scanning.
- **MR Conditional** The device or implant may contain magnetic, electrically conductuve or radiofrequency-reactive components that are safe for operation in proximity to the MRI, provided the conditions for safe operation are defined and observed (both the for MR scanner and the device itself).
- **MR Unsafe** Objects that are significantly ferromagnetic and pose a clear and direct threat to persons and equipment within the magnet room.

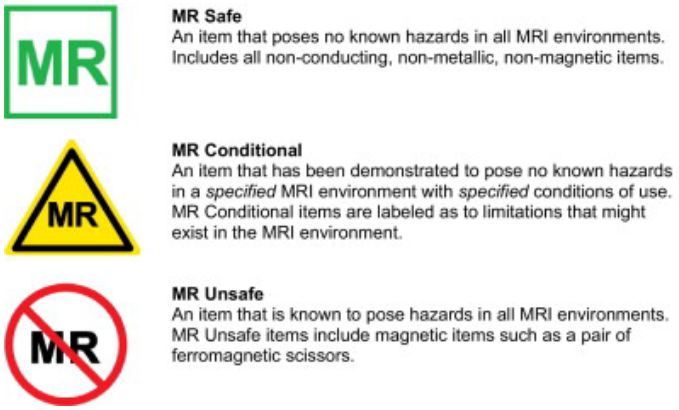

Figure 1.6: American Society for Testing and Materials (ASTM) classifications for materials near the MRI environment. ©ASTM

1.1.4 Overview of Proposed Work

Regardless of imaging type, accuracy of needle tip placement for biopsy core retrieval remains an issue due to unmodeled needle deflection and target shift caused by tissue deformation. [33]. Positive clinical outcomes for deep percutaneous needle based procedures such as targeted biopsy are dependent on the accuracy of needle tip placement. If a target is not reached with sufficient accuracy a physician often retracts the needle without taking a sample and must restart with a new attempt, lengthening procedure time, increasing cost and causing unnecessary discomfort to the patient. Additionally, error in needle placement can cause false-negative biopsy, further complicating diagnosis and leading to additional, unnecessary procedures. Although intra-operative imaging is sometimes available to assist in these procedures, open-loop insertion trajectories wherein image-based feedback is not used to adjust

the trajectory during the insertion, do not account for unmodeled needle deflection or target shift due to tissue deformation. One approach to compensate for unmodeled error is to robotically control the rotation of a bevel-tipped needle to induce corrective deflection towards the desired trajectory. Paired with real-time needle tip tracking, closed-loop image-guided active compensation can be accomplished.

A system controlling robotic needle rotation also requires accurate control needle insertion position; however, incorporating a robot to actuate needle insertion typically either removes a physician completely through autonomous insertion, or distances them from patient interaction through teleoperation. Although teleoperated systems with haptic feedback keep the physician in the loop, there is often significant insulation between the physician and patient not limited to physical separation from the procedure site. Instead, a cooperatively controlled system would keep the physician directly at the surgical site with full control of the procedure, while maintaining the advantages of robotic precision and restoration of tactile feedback. Cooperative control is defined as the direct robotic guidance of a tool that is also held and controlled by the user, which may have wider acceptance by the medical community than a teleoperated counterpart [34].

In our case, cooperation becomes a hands-on robotic needle insertion, where the user applies an input force directly onto the robot to initiate a needle insertion velocity. The system is capable of hands-on cooperative control of needle insertion, with closed-loop autonomous control of needle rotation to perform active compensation of

deflection from the initial straight-line trajectory. Additionally, the robotic system collects needle interaction forces and provides feedback to the user of forces seen on the needle during insertion. An augmented haptic response can be provided at detection of a desired membrane puncture event as well. The robotic needle placement system used in this work is illustrated in position to perform an in-bore MRI-guided prostate biopsy in Fig. 1.7.

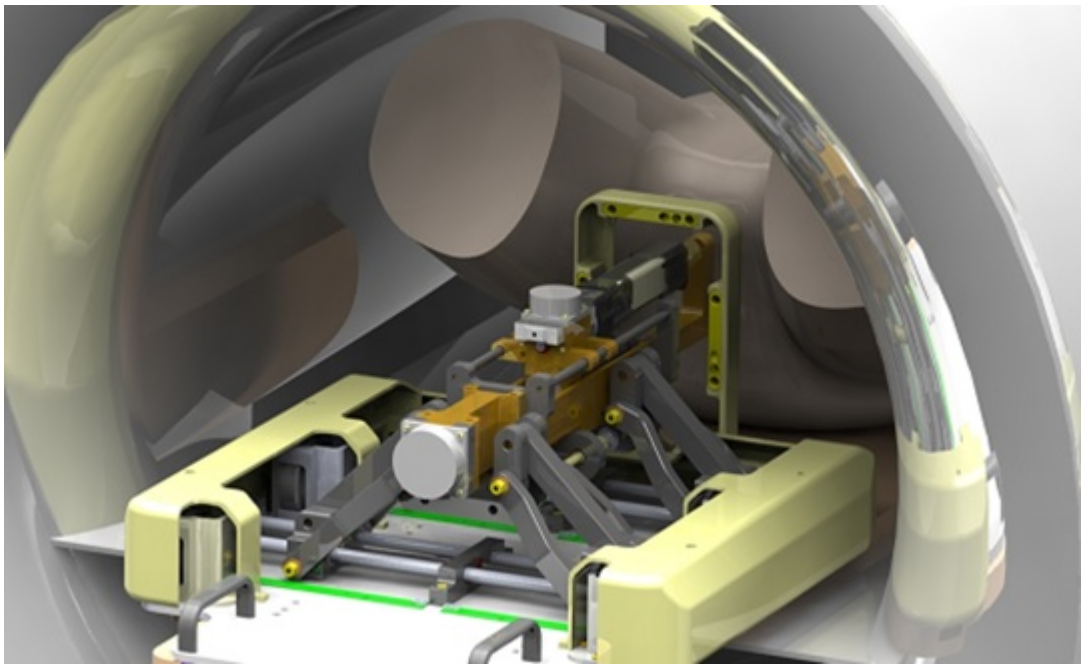

Figure 1.7: A render of the needle placement robot in position to perform an in-bore MRI-guided targeted prostate biopsy.

1.1.5 System Work Flow

The workflow for retrieving a targeted biopsy core using continuous image-guided feedback under cooperative control is illustrated in Fig. 6.11. The workflow follows

that of the manual biopsy, where alignment of the robot base takes the place of selecting which $5mm$ spaced hole on the template guide to insert through, and rather than the physican inserting the needle by hand, to robot holds the needle and the physicians applies an input force to advance the needle forward.

The workflow begins with registration, using a marker or fiducial to register the robot to the scanner coordinate frame, similar to what was done for the template needle guide. After a target feature is selected in imaging, the robot positions the needle at the skin surface and aligns the insertion axis towards the target for a straight line insertion trajectory. Unlike the template guide, this system provides the ability for angulated-entry straight-line insertions, to better target difficult lesions such as those behind the pubic arch. Insertion begins under cooperative control and continues until the target depth is reached or an error condition occurs, such as the needle sufficiently deflecting into a configuration where the target would not be reachable with suitable accuracy. The tip and target features are localized in imaging during insertion and homogeneous transforms describing their location and orientation are passed to the robot controller. The localization information along with robot kinematics and force sensor readings are used to determine the cooperative insertion velocity as well as the bevel rotation required to compensate for any deviations from the initial straight-line trajectory. Insertion continues until the target depth is reached, where a biopsy core is taken if the needle tip has reached the target with sufficient targeting accuracy.

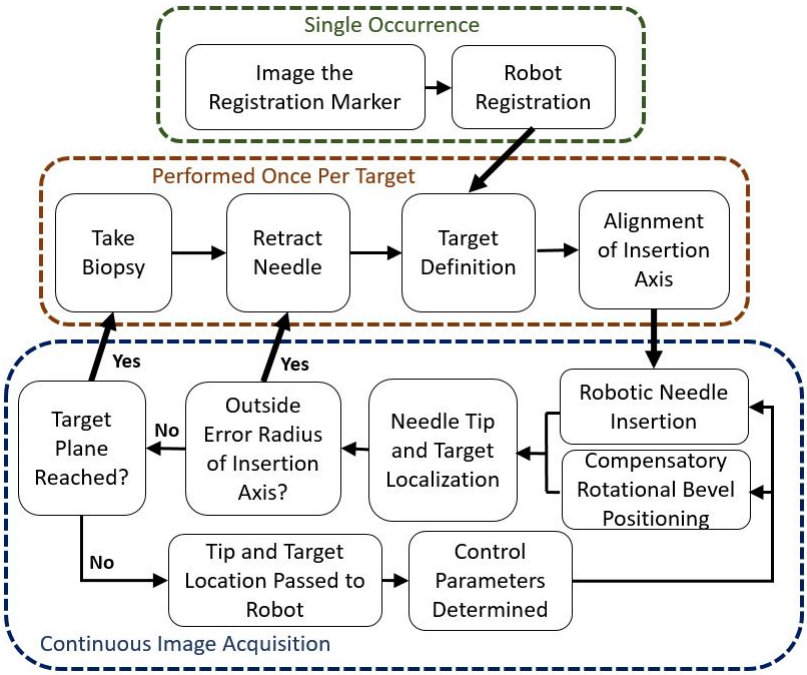

Figure 1.8: The complete system work flow for collecting an image-guided targeted biopsy using cooperatively controlled needle insertion with active compensation for unmodeled needle deflection and target shift.

1.1.6 Motivation for this Work

Motivation for this work came as our research group performed clinical trials of MRI-guided robot-assisted prostate biopsy using the robot seen in Fig. 1.9. This system employed robot assistance for target alignment but was still dependent on manual needle insertion along the robotically aligned axis [35]. As a result, even though initial alignment was performed robotically, the manual insertion still suffered from loss of targeting accuracy due to unmodeled needle deflection and target shift.

Targeting accuracy across all clinical trials was $6.5 \pm 5.1mm$ with an average of 2.2 insertion attempts per biopsy core taken [36]. Figure 1.10 shows the robot in place inside the MR-bore during a clinical trial as well as an annotated render of the robot and patient showing how the robot was positioned with respect to the patient.

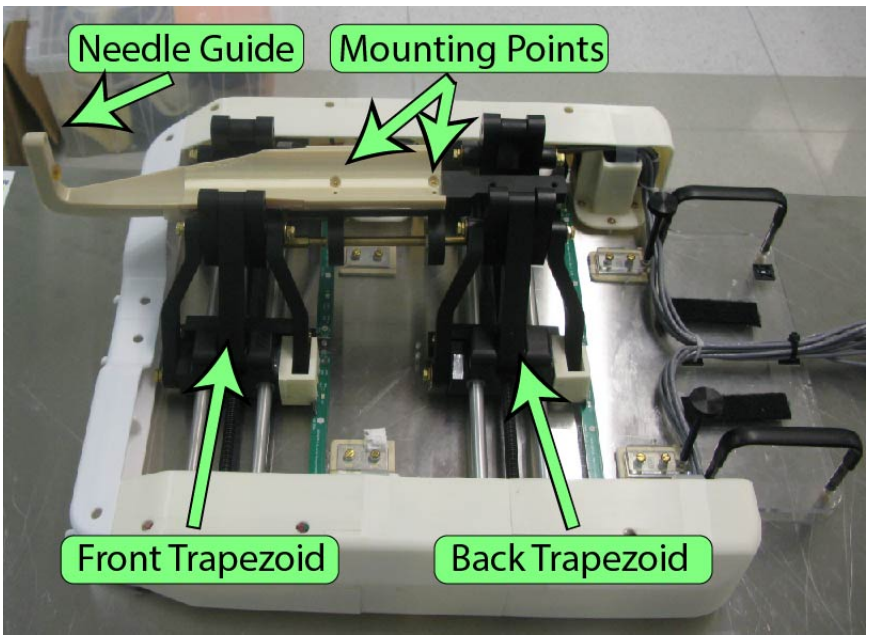

Figure 1.9: The 4-DoF robot used by our research group in clinical trials of robot-assisted prostate biopsy. The base aligns the needle guide to an initial straight line insertion trajectory to the target, with the needle inserted manually through the needle guide.

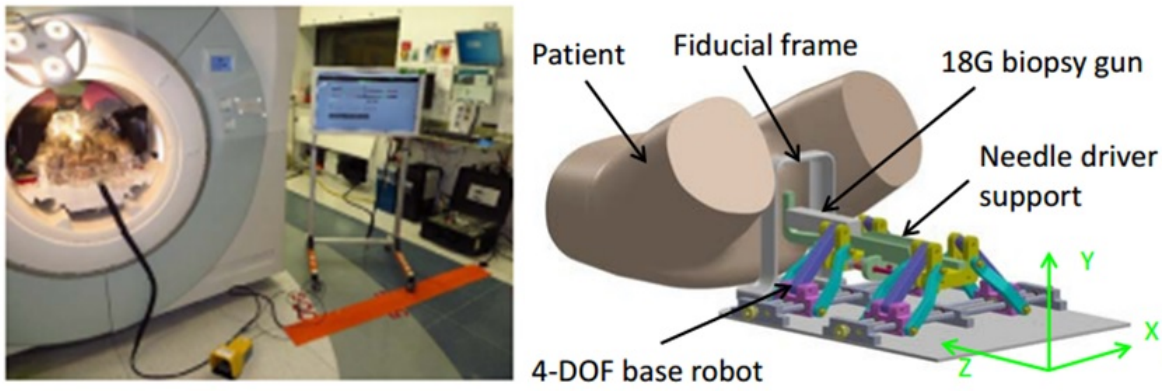

Figure 1.10: A description of how the 4-DoF robot was used in clinical biopsy. Left) The experimental setup for clinical trials of robot-assisted prostate biopsy at Brigham and Women's Hospital, Right) a render showing the robot position relative to the patient.

1.2 Literature Review

As shown through the background and motivation for the presented work, this research is mostly focused on prostate cancer intervention. More specifically, focus is on minimally invasive robotic interventions using MR imaging as feedback, with an overview of MRI-guided robotic prostate interventions given in [33]. Due to the constraints of mechatronic systems within the MR environment, pneumatic and piezo-electric actuators are the two primary types of actuation which have been used. A literature review of the past robotic implementations in MRI is presented, mostly fo-

cused on prostate interventions with a few other examples included when relevant. A description of needle insertion and steering methods is presented, as well as research related to needle-tissue interaction forces and membrane puncture detection. Any related work completed by our research group is described in section 1.2.6.

1.2.1 Pneumatically Actuated Biopsy Robots

Pneumatic cylinders have been explored in MRI applications because of their low cost, high force/volume ratios, and the absence of significant heat or magnetic field generation. For instance, a pneumatic piston-cylinder for needle insertion was developed by Comber et al. [37] and can be seen in the top right of Fig. 1.11, compensating for reaction force of the tissue on the needle. A hybrid pneumatic-hydraulic robot described by van den Bosch et al. [38] and seen in the bottom of Fig. 1.11 employs a tapping device to pneumatically insert the needle an adjustable stepwise distance, stopped each time by a hydraulic cylinder. Building on this, Lagerburg et al. [39] showed that the tapping technique created less tissue deformation than manual needle insertion. Stable control of in-bore pneumatic actuation with long ($9m$) plumbing was shown by Yang et al. [40] for breast biopsy under continuous MRI. A pneumatic stepper motor was developed by Stoianovici et al. [41] and employed in a completely MRI-safe robot for transperineal prostate biopsy [42] and endorectal prostate biopsy [43], seen in the top left of Fig. 1.11. Another pneumatic stepper motor was developed by Chen et al. [44], but is considered MR-Conditional as it con-

tains two pneumatic cylinders with conductive components. A transgluteal approach using pneumatics was implemented in a cadaveric study by Zangos et al. [45], which was extend into clinical trials with patients [46].

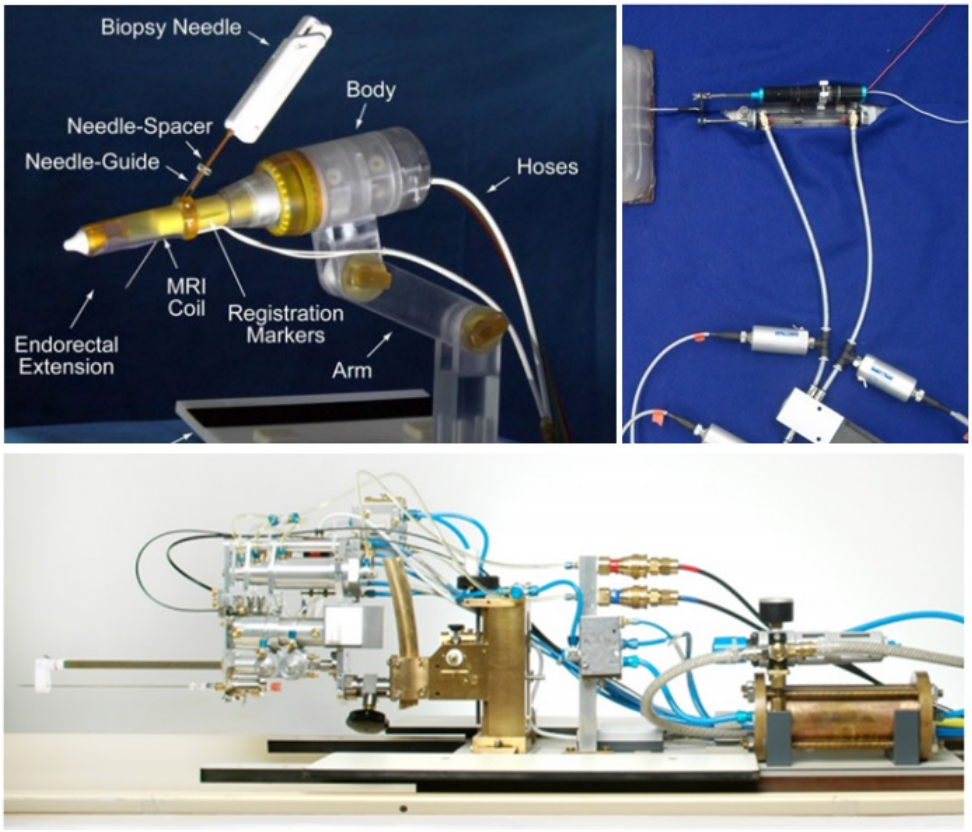

Figure 1.11: Pneumatically actuated robots in literature. Top left) An MRI safe robot for endorectal prostate biopsy [43], Top right) Needle insertion into a phantom using a pneumatic piston [37], Bottom) a hybrid pneumatic-hydraulic system for MRI guided prostate biopsy [38]

1.2.2 Piezoelectrically Actuated Biopsy Robots

Piezoelectric approaches have been explored as well, such as the system described by DiMaio et. al [47] for prostate biopsy in an open MRI scanner architecture, illustrated on the right in Fig. 1.12. Additionally, Goldenberg et al. [48] developed a 6 degree of freedom (DoF) robot for prostate interventions primarily made from aluminum, initially tested for laser ablation. A transrectal approach using piezoelectrics was developed by Elhawary et al. [27], with a Cartesian base and actuated 2-DoF needle motion for needle insertion and biopsy collection seen in the middle of Fig. 1.12. Another transrectal implementation was described by Krieger et al. [26], showing targeting accuracy comparable to the manual case. Piezoelectric acutation have been used in teleoperation to provide haptic feedback in the MR environment as well. Teleoperated needle insertions have great potential as haptic feedback could relay the forces seen on the needle, with the ability to incorporate virtual fixtures (VF) as well as augment or enhance the forces seen while puncturing through tissues of different mechanical properties. A biopsy unit was presented by Tse et al. [49], using PiezoLEGS motors (Piezomotor Inc, Upsala, Sweden), where physicians reported realistic force reconstruction in the master device. A render of this device attached to a transrectal ultrasound probe can be seen on the right of Fig. 1.12. Piezoelectric actuation allows for a fast control response with high accuracy of positioning, but significant effort must be placed on improving MRI-compatibility. Previous research groups have seen significant degradation in MR image quality, with Song et al. [50]

reporting 44% loss and Koseki et al. [51] reporting 93% signal loss in a 0.3T open MRI scanner.

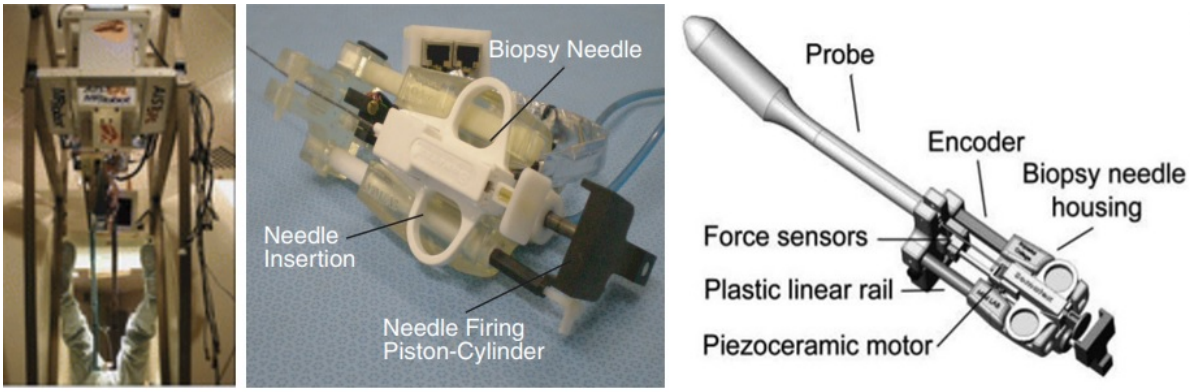

Figure 1.12: Piezoelectrally actuated robots in literature. Left) a robot for prostate biopsy implemented in an open MRI scanner [47], Middle) A transrectal approach for prostate biopsy using piezoelectric actuation [27], Right) A render of biopsy unit for prostate biopsy using PiezoLEGS motors [49].

1.2.3 Cooperatively Controlled Robots

Regarding teleoperated systems, many were developed to keep the physician in the procedural loop. In reality, teleoperation still removes the physician from direct access to the patient. Instead, a cooperatively controlled system would keep the physician directly at the surgical site with full control of the procedure, while maintaining the advantages of robotic precision. In cooperative control, the user initiates motion and the robotic system can augment the motions imparted by the user but cannot

initiate motions itself, providing haptic cues that can be used to improve physician's performance [52, 53].

Cooperative devices include the ROBODOC seen at the left of 1.13, used in hip replacement and showed a statistically better fit and positioning of the femoral component [54]. The ACROBOT was designed for bone preparation in total knee replacements [55] and can be seen in the bottom right of 1.13, and the Steady Hand Robot [56] shown in the top right of Fig. 1.13 was used to eliminate the effects of hand tremor in eye surgery. Another device was the PADyC which consisted of a manually actuated arm that dynamically constrains the authorized motions for accurate cardiac puncture [57]. This system showed adequate constrain of motion but with required forces much larger than typically seen for cardiac puncture.

In our case this becomes a hand's on needle insertion, where the surgical workspace is shared between the physician and the needle insertion robot. The physician applies an input force directly onto the robot controlling the needle insertion velocity, but the robot can augment the workspace based preoperative planning.

An example of a biopsy robot described to work synergistically with the physician was described by Megali et al. [58]. This system was considered synergistic in that the procedure had both robotic and manual input components. The alignment of the biopsy needle was done robotically followed by a manual needle insertion, much like the clinical version of our research group's biopsy robot previously described. The system described herein is different in that the cooperative aspect is hands-on synergy

between robot and physician during the insertion task.

Figure 1.13: Cooperatively controlled robots in literature. Left) The PADyC used for joint replacement [57], Top Right) The Steady Hand Robot for eye surgery [56], Bottom Right) The Acrobot used in knee replacement [55]

1.2.4 Active Compensation for Needle Deflection

Regardless of the needle insertion method, the rotational position a bevel tip is facing induces deflection in that direction if it is acting against a solid tissue. Deflection of an asymmetric bevel tip can be exploited for compensation, but the maximum needle tip deflection and consequently the degree of compensation attainable is limited by the mechanical properties of the needle. Using image-feedback, this position can be continuously updated to follow a desired trajectory and related work in literature

is primarily based on steering thin flexible needles. Modeling of flexible needles has been widely implemented using the kinematic bicycle model [59] shown in the top left of Fig. 1.14, as well as a modeled using a joint kinematic and dynamic system [60]. These were expanded using imaging for feedback by Abazid et al. [61] for evaluation of two models for flexible needle steering, one kinematics based and one based on needle-tissue interaction forces. A duty cycled approach for needle steering was introduced by Engh et al. [62], with needle curvature shown for three different duty cycles at the right of Fig. 1.14. This was expanded by Minhas et al. [63], with Vrooijink et al. [64] implementing this for 3D targeting using ultrasound imaging, illustrated in the bottom left of 1.14. The duty-cycled approach, although implemented widely with positive results, requires insertion and rotation to be very coupled so as to alternate between pure insertion and rotation during insertion, which would not be feasible in a cooperative approach. Other approaches such as concentric continuum tubes [65, 66], actuated flexible needles [67–69] and pre-curved needles [70] have been employed to accurately reach a target. Additionally, manipulation of the needle base [71, 72] or the tissue itself [73] has been tested as well. A hand-held device for seed placement in brachytherapy was introduced by Rossa et al. [74], rotating the needle autonomously during manual needle insertion. This system can be comparable to the work presented here in that rotation is autonomous while insertion is user directed, however; a cooperative insertion approach adds robotic accuracy to the insertion axis as well.

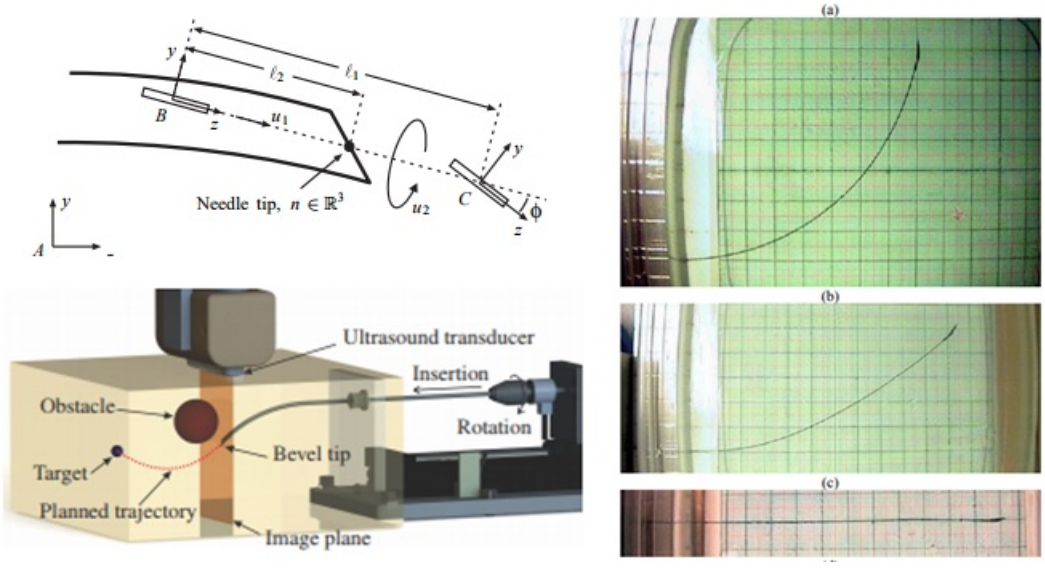

Figure 1.14: Needle steering and deflection compensation techniques in literature. Top Left) the non-holonomic bicycle model [59], Right) Three needle curvatures using the duty cycled approach [62], Bottom Left) implementation of the duty cycle approach using ultrasound for image feedback [64].

1.2.5 Needle Interaction Forces

Tactile forces felt during manual needle insertion are often used by physicians for anatomical localization and mental registration of the needle tip within the body. Some of this localization feedback is provided by detection of membrane puncture events during insertion. When substituting manual needle insertion for a cooperative robotic insertion, providing a haptic response at detection of a membrane puncture event can replace the feedback felt naturally, or a non-transparent augmented haptic response can provide additional information to the physician.

To provide any sort of feedback at a puncture event, the puncture must accurately be detected by the system. Needle interaction forces have been widely researched and several techniques for puncture detection have been proposed. Early work in force modeling by Simone et al. [75] and Okamura et al. [76] showed needle axial forces measured during insertion through a bovine liver with a capsule puncture, illustrated in Fig. 1.15. This work discussed application to robotic interventions, where tissue forces seen on the needle could be reflected back to a user such as in the system presented herein.

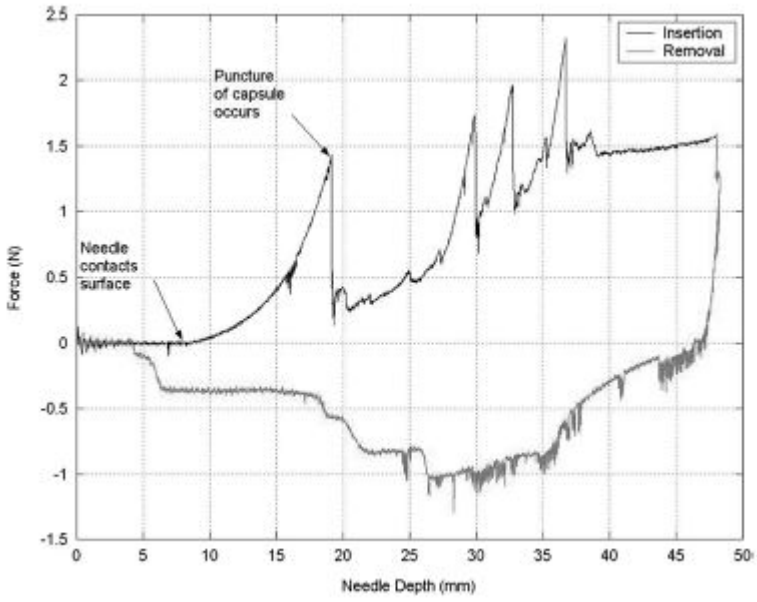

Figure 1.15: Needle insertion forces showing a typical force profile for puncture of a capsule [76]. Axial force steadily increases on the needle at interaction with the capsule, followed by a sharp drop at puncture.

Throughout needle insertion into soft tissue, different phases of interaction can be

identified: 1) No interaction, 2) boundary displacement, 3) tip insertion and 4) tip and shaft insertion as seen in Fig. 1.16. Each phase has been independently studied and the progression of insertion phases can be applied to the interaction at an external skin membrane as well as an internal capsule. During boundary displacement the needle is in contact with the membrane but has not yet penetrated the tissue layer, a situation referred to as tenting [77, 78]. As the load increases on the needle point the stress on the tissue crosses a certain critical point where a crack will be initiated and the needle will start to penetrate [79]. During tip insertion, the cut made by the tip of the needle expands either gradually to the size of cross section of the needle through cutting [80], or suddenly through rupture [81]. Tip and shaft insertion is characterized by a generally constant sized hole in the penetrated boundary, with increased friction force on the needle as it is advanced deeper into tissue [82]. A survey of needle-tissue interaction forces with experimental data is presented in [83].

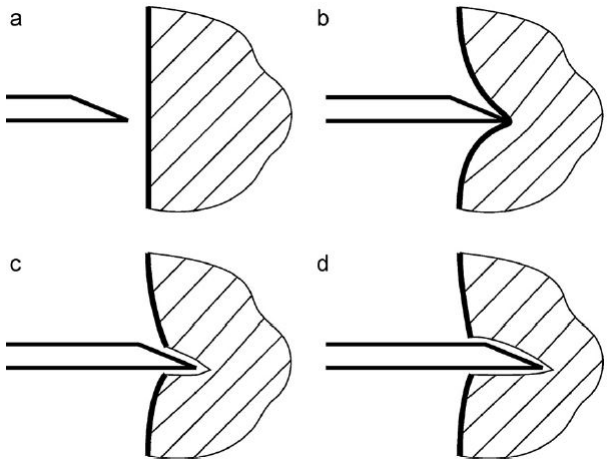

Figure 1.16: The four basic phases of needle-tissue interaction: a) no interaction, b) boundary displacement, c) tip insertion, d) tip and shaft insertion [83]

In this case we are interested in the transition from boundary displacement to tip insertion, and previous work has focused on both thresholding force data as well as implementation of probabilistic models to correctly identify when a true puncture event has occurred. For instance, Barbe et al. [84] employed a statistical model for fault detection originally developed for industrial processes, while Kobayashi et al. [85] developed a model based on needle force, velocity and position depth within a tissue.

Similar work as proposed here regarding puncture detection of membranes during robotic needle insertion was reported by Elayaperumal et al. [86], using a customized needle enhanced with Fiber Bragg Grating (FBG) sensors. This work was extended by Bae et al. [87], designing a teleoperated version suitable for use in the MR. These show meaningful results by separating cutting force on the needle tip from frictional force on the needle shaft, as forces seen on the needle are in fact comprised of three

components: the cutting force, the friction force, and the prepuncture stiffness force [76]. The research presented here differs as that work required a customized needle and is not possible with intent of bringing this system to pre-clinical and clinical trials. Therefore, our system differs both in the application of cooperative control as well as collecting the sum of all forces together behind the clinically employed biopsy gun, as to not alter the already regulatory approved device.

1.2.6 Preceding Work by our Research Group

Previous work by our research group has led incrementally to the development of the system presented in this dissertation. Several robotic systems have been designed and evaluated contributing to various aspects of robotic biopsy. For instance, Fischer et al. [3] showed a pneumatic robot for transperineal prostate needle placement, achieving an acceptable level of MR scanner interference while preserving the workflow of conventional TRUS-guided procedures. This system was adapted and used in other work, adapting the control system to a new manipulator [88], performing an accuracy study using a commercial optitrack system [89] and using the device as a slave manipulator for teleoperation [90]. Pneumatics were used in Tokuda et al. [91], a 4-DoF actuator for angulated needle placement. Angulation allows for pubic arch avoidance, leading to the ability to treat of large volume glands with locations unable to be accessed via TRUS-guided procedures. Additionally, piezoelectric motors were used in Su et al. [92], which can be seen in Fig. 1.17 for direct robotic needle

placement in the MRI.

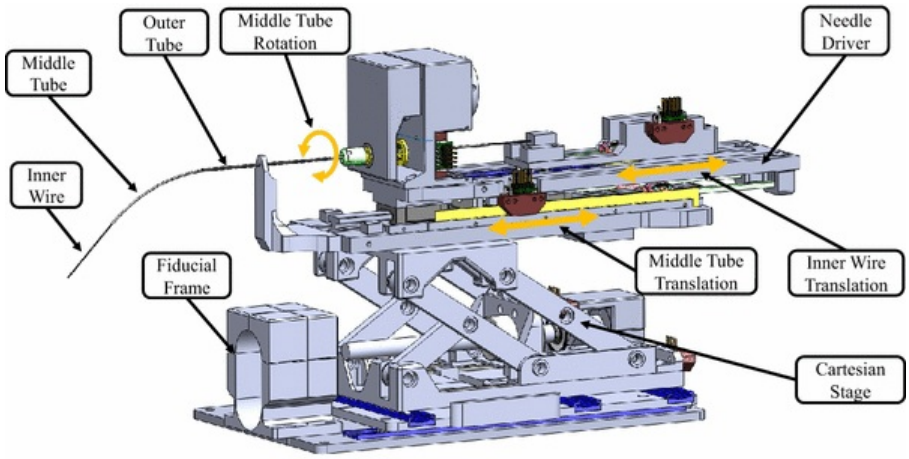

Figure 1.17: A robot developed by our research group for direct robotic needle placement in the MRI [92]. A cartesian stage aligns the needle axis towards the target and a needle driver inserts and rotates a needle for placement.

Additionally, this robot was adapted as a slave device showing acceptable in bore teleoperation with haptic feedback for needle placement [93], and used separately to show closed-loop needle steering during continuous multi-planar image acquisition [94] illustrated in Fig. 1.18

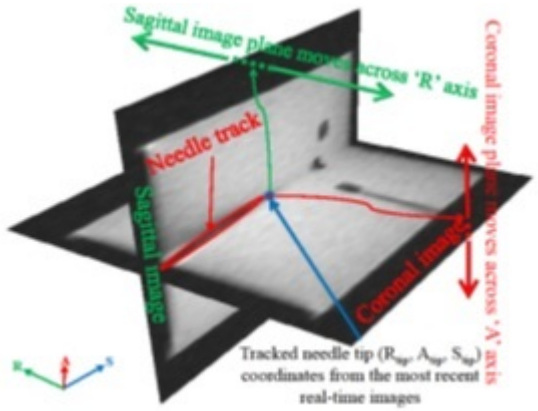

Figure 1.18: Needle localization using multi-planar MR images. The 3D coordinates of the needle tip are found by localizing the tip in two perpendicular images [94].

A robotic needle driver was developed by Li et al. [95], intended to work with the aforementioned robot base used in clinical trials. This system was controlled by a GUI with discrete buttons corresponding to $1mm$ or $5mm$ insertion, and rotation of the needle limited to $\pm 180^o$. To improve upon this system, interest in cooperative control insertions arose and work on this dissertation began.

1.3 Dissertation Contributions

In much of the literature present, the specialized thin flexible needles used for research in needle interventions are not approved by a regulatory agency for biopsy; in fact, they are mostly solid core and too thin to be used in a clinical scenario where a tissue sample must be retrieved. Research contributions on needle steering tend to be focused on obstacle avoidance or following trajectories of a predefined shape to a

target location, while teleoperated systems aim for stable control of needle insertion position with haptic feedback.

Here the work is focused on clinical translation, where translational research or translational medicine can be defined as combining disciplines, resources, expertise and techniques to promote enhancements in prevention, diagnosis and therapies [96]. More succinctly, it has been described as "benchtop to bedside" research, initiated with the goal of clinical implementation [97]. In this case, rather than manipulating a thin flexible needle, we're interested in active compensation for deviations from an initial straight-line trajectory using a typical 18G biopsy needle. More so, to perform this compensation during cooperatively controlled needle insertions to maintain a biopsy procedure directed by the physician at the procedure site. Another advantage of cooperative control is continuous and augmented haptic feedback to restore and enhance tactile information typically surrendered in favor of robotic accuracy.

The research contributions presented in this dissertation were all developed to improve the state of the art of clinical prostate biopsy. Many of these contributions are applicable to other scientific and engineering endeavors, but are summarized here in context of using image-feedback to robotically place a needle for biopsy collection while maintaining a physician's ultimate control of the procedure. The following contributions are split into scientific and engineering components, where scientific contributions reflect new work, knowledge and research, while engineering contributions are required for clinical translation.

- **Scientific Contributions**
  - **A Needle Placement Robotic System** A robotic needle driver suitable for use within the MR-bore was designed and fabricated. The system is configured for cooperatively controlled robotic needle insertion alongside closed-loop image-guided active-compensation for deviations from an initial straight-line needle insertion trajectory. The control system architecture was developed based on integration between a robot controller, the MRI scanner and surgical navigation software 3DSlicer using the open network communication protocol OpenIGTLink. The effect of the system on the Signal-to-Noise Ratio (SNR) of MRI images was evaluated.
  - **Cooperative Control Algorithm For Needle Insertion** A nonlinear algorithm for providing continuous haptic feedback through cooperatively controlled robotic needle insertion was developed. This control algorithm is based on the difference of user input and collected needle forces, scalable by an exponential decay constant to alter the sensitivity of the difference between input and needle forces on insertion velocity.
  - **Membrane Puncture Detection** Due to needle deflection and target shift, kinematic motion of the robot cannot guarantee a specific depth has been reached, but by pairing this with real-time needle force data, a window around the suspected membrane region can be monitored for a puncture event.

- **Engineering Contributions**
  - **An Image-Agnostic System For Active-Compensation** An imaging agnostic method of closed-loop active compensation for unmodeled deflection and target shift during targeted needle insertion was developed. Information of needle tip and target localization is passed one-way downstream from the image-guidance software to the robot controller via the OpenIGTLink communication protocol. The system autonomously rotates a bevel tipped needle towards the direction of desired compensatory effort.
  - **System Integration** Integration of hardware and software subsystems was performed to prepare for experimental validation in the clinical environment. The system hardware was designed to maintain a similar workflow as seen in the clinical trials of robot assisted biopsy and the needle driver design inherently maintained the sterilization techniques used. A web GUI was used for control of software subsystems, and this was integrated with the surgical navigation software and the MRI scanner console in the complete system architecture.
  - **In-bore System Validation** The full robotic system was tested inside the MR-bore. Targeted needle insertions were performed under cooperative control with autonomous rotational bevel tip positioning for active compensation, along with paired imaging and force sensor membrane puncture detection.

1.4 Dissertation Overview

The introductory chapter began with the background and motivation for the work performed in completing this dissertation. This was followed by a literature review of related work and the overall project evolution by our research team, leading to the direct contributions of this authors work.

Chapter 2 introduces the robotic needle placement system. The needle placement manipulator is presented along with its functional components of piezoelectric actuation, force sensing and clinical biopsy gun integration. In addition, the robot forward and inverse kinematics are presented.

Chapter 3 introduces the reconfigurable control system architecture. A description of the controller hardware and software architecture is presented, as well as the custom controller box developed to house the entire control system.

Chapter 4 introduces the paradigm for cooperatively controlled needle insertion. The formulation of cooperative control algorithms is described, which is based on user input and the collection of needle forces. Next, a technique is introduced for enhancing cooperatively controlled insertion with augmented event based haptic feedback at membrane puncture. Characterization of materials for tissue phantoms is then performed, to accurately mimic the mechanical properties of periprostatic tissue during insertion. Finally, in-lab validation tests for membrane puncture detection are then presented.

Chapter 5 focuses on targeting specific locations with the needle tip via image-

based feedback. Registration and feature localization are described within the particular laboratory setup used to develop the algorithms, followed by an image-agnostic technique for closed-loop active compensation based on rotational bevel tip positioning. In-lab validation results for targeting both stationary and shifted targets is presented.

Chapter 6 presents our system integration. A complete architecture for using this system in the clinical environment for cooperatively controlled prostate biopsy is given, including integration of individual software and hardware components to perform in-bore needle insertions. The effect of the system on the SNR of MR images is presented, then the final system is validated during in-bore experiments.

We conclude and discuss future work in Chapter 7.

Chapter 2

Needle Placement Manipulator For Prostate Biopsy

2.1 Introduction

This chapter introduces the robotic needle placement manipulator for performing transperineal MRI-guided targeted needle insertion under cooperative control. A major goal of this work was to identify components and design a system for safe and effective use in the MRI. The design requirements are given and the full 6-DoF system is presented. Additional focus is given to the 2-DoF needle driver specifically developed as part of this work, with functional components of piezoelectric actuation, force sensing and needle integration discussed. The kinematic parameters along with the forward and inverse kinematics of the system are then presented.

2.2 Design Requirements

The most important requirement for the robotic system was compatibility with the MR environment. This requires no ferromagnetic material and minimal use of other metals only where necessary, such as the use of brass hardware. Regarding the clinical trials performed using the robot base, an added needle driver should mount directly in place of the previous needle guide. The average targeting accuracy of the robot assisted clinical trials was $6.6 \pm 5.1mm$, but studies have classified targets to be any tumor foci greater than $0.2ml$ ($3.6mm$ radius) [15]. For instance, in a study of 96 men, 215 cancer foci were found and 90% were under $0.5mL$ ($4.9mm$ radius) and 79% were under $0.2mL$ ($3.6mm$ radius) [98]. Therefore, adding active compensation should aim to increase targeting accuracy by 50% to target tumor foci as small as $0.2ml$.

In addition, the needle driver must not interfere with the robot base function or limit its motion or work space in any way. The needle driver must be needle agnostic, requiring changing just a mounting bracket for a different needle or biopsy gun to be used. The needle driver must be capable of $150mm$ of needle insertion as this is the typical biopsy needle length. Insertion speed limited to $10mm/s$ allows for compensatory deflection to correct for deviations from a straight-line trajectory, while speed as low as $1mm/s$ is required for compensation under real-time MR imaging which can be as slow as $2Hz$. The needle driver should also be capable of a full 360^o of continuous uni- and bidirectional rotation to perform active compensation.

The system must be capable of performing cooperative needle insertion, collecting both a user input force and the forces seen on the needle behind the biopsy gun. The forces should be collected by sensors which do not adversely effect the SNR of the images, and do not suffer from interaction with the magnetic field. Finally, the work flow used in manual procedures which was extended to the clinical trials should be maintained as close as possible, including sterilization and draping of the robot during experiments and procedures.

2.3 The Robotic Mechanism

The needle placement robot that was developed throughout completion of this dissertation consists of the 4-DoF clinical alignment base described in [99], with a 2-DoF needle driver developed specifically for cooperative needle insertion. The needle driver mounts directly to the 4-DoF base in place of the manual needle guide and is configured for cooperatively controlled needle insertion with continuous closed-loop needle rotation. The bulk of the robotic components were machined from the high strength thermoplastic Polyetherimide, more commonly referred to as Ultem, with several smaller components 3D printed from Acrylonitrile Butadiene Styrene (ABS). An annotated image of the robotic needle placement manipulator is shown in Fig. 2.1.

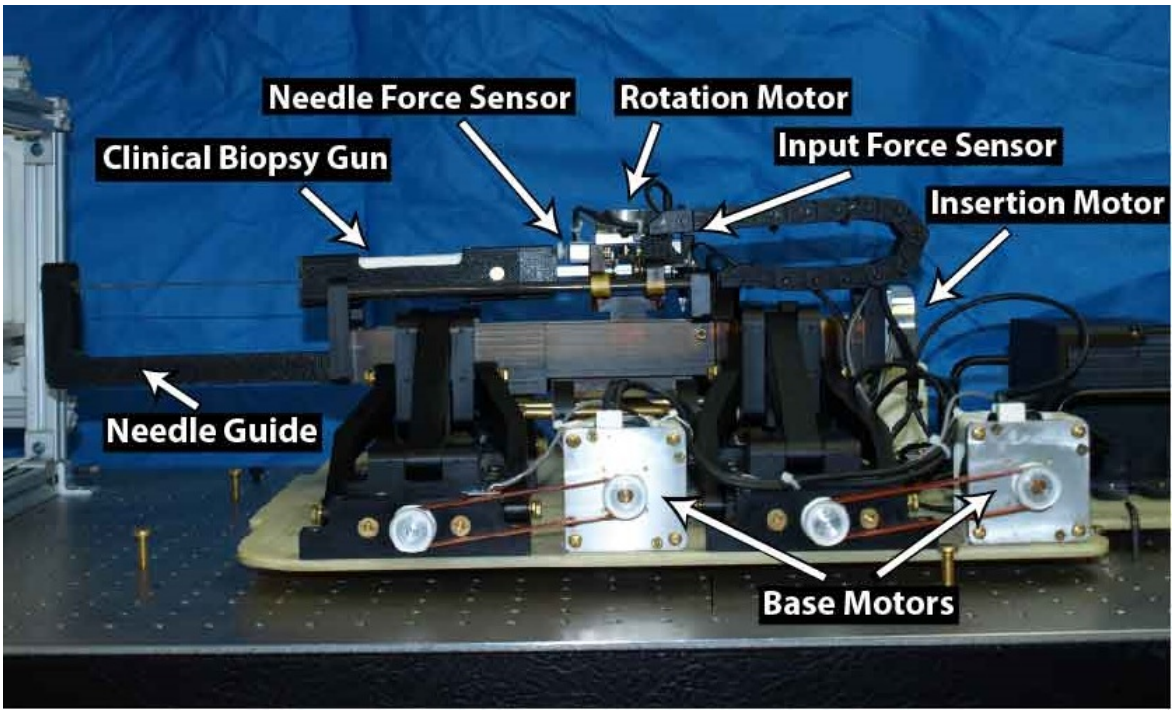

Figure 2.1: An annotated figure of the robotic needle placement manipulator. The robot is suitable for use in the MR environment with brass hardware and components primarily machined from Ultem. The robot is designed to align the insertion axis to a target, insert and rotate a biopsy gun using piezoelectraic actuation.

Slight modifications such as cable management were made to the clinical base, but the bulk of design and fabrication was performed on the needle driver. Figure 2.2 shows a series of renders of the needle driver design. The needle driver mounts directly to the 4-DoF base in place of the manual needle guide, is configured for cooperatively controlled insertion with 360^o of continuous closed-loop needle rotation.

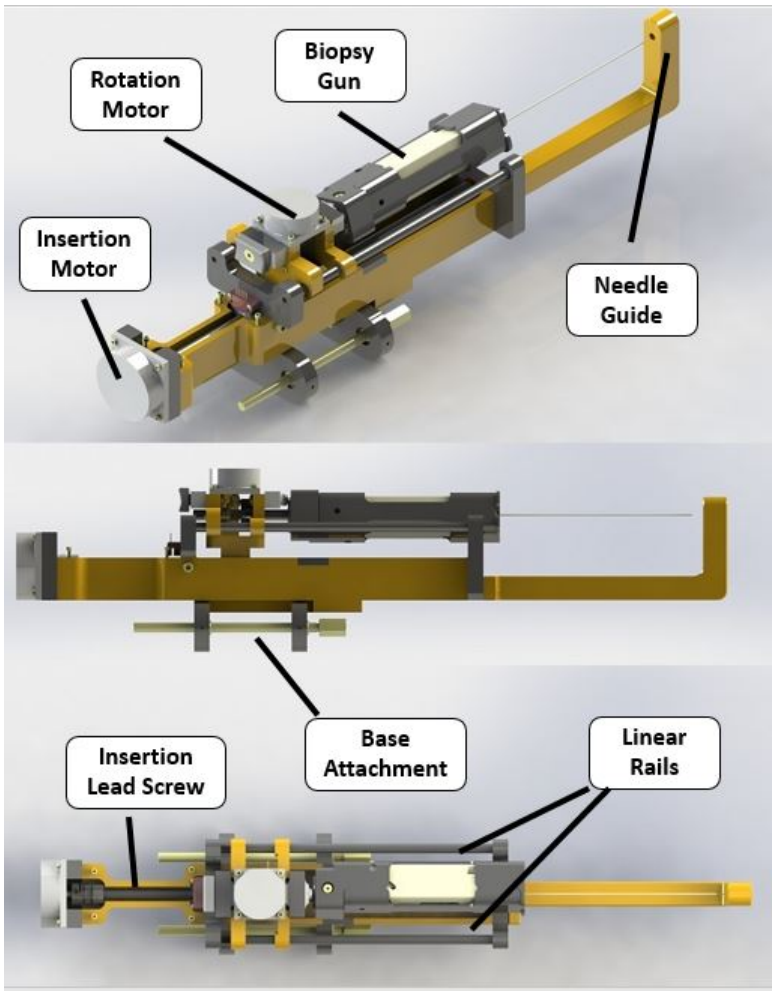

Figure 2.2: Three views of the needle driver specifically developed throughout work on this dissertation. The needle driver mounts to the clinical 4-DoF base in the same location as the manual needle guide.

An aluminum lead screw with a $12mm$ diameter and a $3mm/rot$ pitch from IGUS (Rumford, RI, USA) was used to move the sliding carriage forward with actuation of the insertion motor at the back of the needle driver. The sliding carriage moves along two aluminum linear rails and the the rotation motor was mounted directly to

the top of it. The rotating shaft connected to the biopsy gun is hollow to allow for a plunger to reach the firing pin at the back of the gun, and was coupled to the rotation motor via a set of brass bevel gears. All position feedback was achieved using optical encoders with 1250 counts per revolution (CPR) from US Digital (Vancouver, WA, USA), model EM-1-1250 with disks mounted on each rotating shaft. Figure 2.3 shows an annotated view of the carriage up close, while Fig. 2.4 shows the sliding carriage motion for needle insertion.

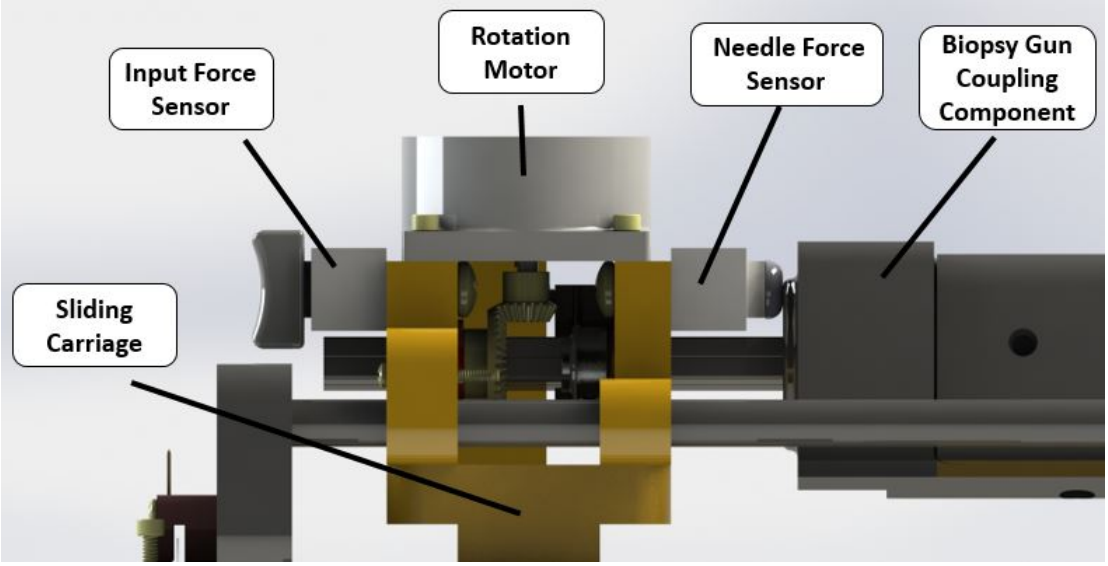

Figure 2.3: A close-up view of the needle driver sliding carriage showing the input and needle force sensors.

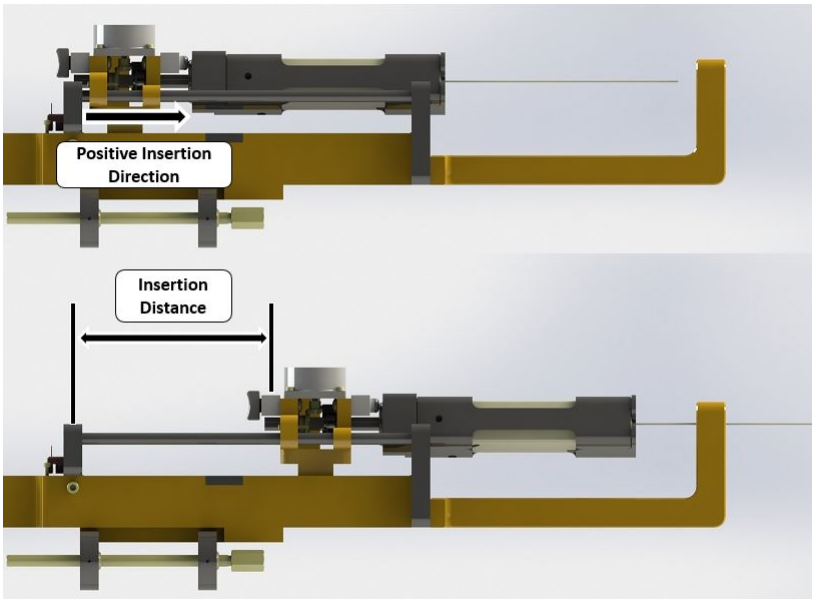

Figure 2.4: Movement of the sliding carriage for needle insertion. The positive direction corresponds to needle insertion.

2.3.1 Functional Components

2.3.1.1 Piezoelectric Actuation

Typical DC motors are inherently not compatible with the MRI environment. Instead, actuation for each axis is performed by non-magnetic harmonic drive piezoelectric motors, model USR-60 from the Shinsei Corporation (Tokyo, Japan), and models USR-45 and USR-30 from Fukoku Co Ltd. (Tokyo, Japan) respectively. Similarly to their DC counterparts, these motors are comprised of a stator and a rotor, but rather than using magnets the stator is a ceramic piezoelectric element bonded to a micro-deformable copper body. The rotor is aluminum and is coupled to the

stator through preloaded friction. When two sinusoidal waves with 90^o phase shift in the range of $47Khz - 51Khz$ are applied to the piezoelectric crystal, a traveling wave propagates to deform the copper body and spin the rotor. These motors were controlled with dedicated drivers from Shinsei Corporation, model D060. The labeled components of the piezo motor are detailed in Fig. 2.5.

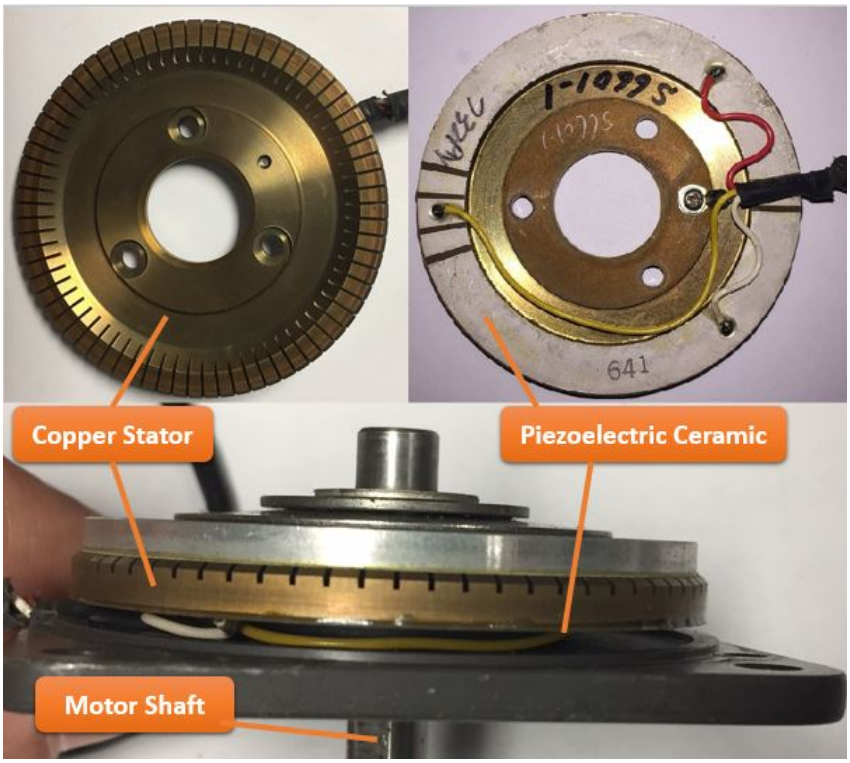

Figure 2.5: The components of the piezoelectric motor used in this system. Top Right) the copper stator, Top Left) the ceramic crystal is glued to the back of the stator, Bottom) the rotor is coupled via preloaded friction when the case motor is attached.

2.3.1.2 Force Sensing

If constructed properly, force sensing within the MRI can be accomplished using traditional load cell force sensors. Applications of strain gauge based implementations in MRI have been explored, such as a 3-DoF sensor by Sutherland et al. [100], or implementations for haptic feedback in teleoperated systems for needle based procedures by Kokes et al. [101] and Tse et al. [49]. A preferred option for use in the MRI would be fiber optic force sensing, as fiber optics are completely MRI-safe. Fiber optic implementations include force sensing through phase modulation, such a Fabry-Perot interferometer (FPI) [102], or wavelength modulation such as a customized needle embedded with Fiber Bragg grating [103].

As our design requirement was to maintain the integrity of in-use clinical biopsy needles, it was necessary to determine the needle force from behind the entire biopsy gun and this was done with a shielded aluminum cased load cell sensor MLP-10 from Transducer Techniques (Temecula, CA, USA). An identical sensor was used to capture user input and Figure 2.6 shows sensor data collected inside the MR bore during a needle insertion and how an input force is applied to the robot to create a cooperative insertion velocity. Functional use of the force sensors for cooperative inesrtion and membrane puncture detection is described in Chapter 4.

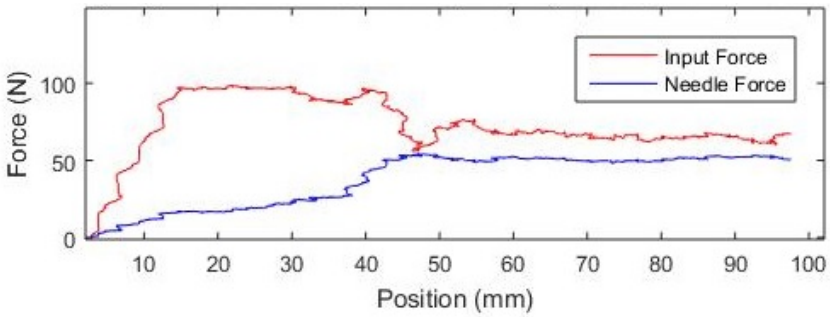

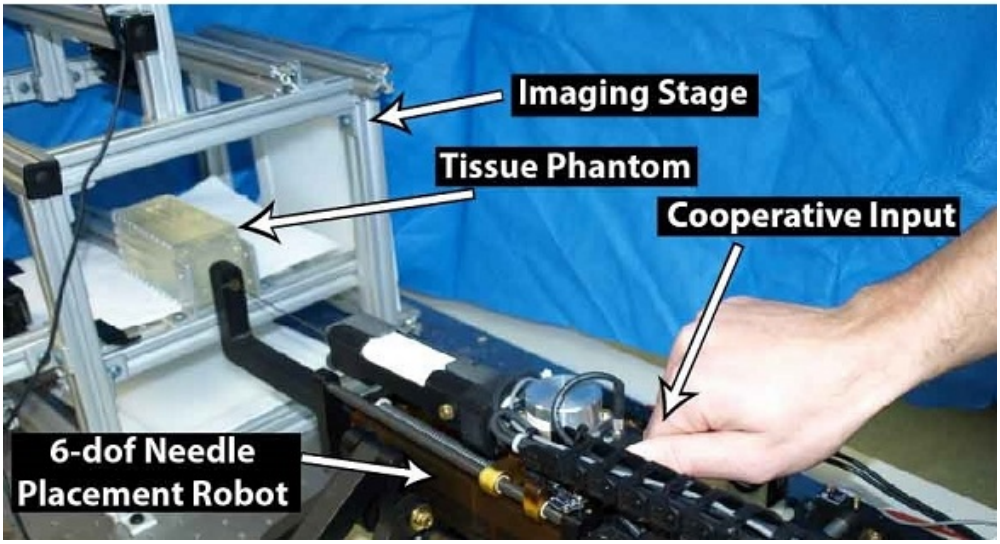

Figure 2.6: Top) Input and needle force data seen during a cooperative needle insertion inside the MRI. Bottom) A photo showing the application of a cooperative force input onto the needle placement robot.

2.3.1.3 Needle Integration

Through discussing with physicians on how the current techniques for manual biopsy can be improved through robotics, the requirement for incorporating robotic accuracy without altering in-use clinical biopsy guns was evident. Typical biopsy guns are an already regulatory approved device, and a robotic system that can manipulate

this already in-use tool has a much higher chance of succeeding in regulatory approval itself. Taking this into account the robotic system was designed to be needle agnostic, capable of inserting and rotating different biopsy devices with an alteration to just the coupling component. This component is 3D printed in ABS and can be easily altered for use with a different biopsy tool. Throughout this work a biopsy gun typically used in MR-guided clinical procedures was used, the Full-Auto Bx Gun 18G 175 mm from Invivo (Best, Netherlands). This biopsy gun along with its specific coupling component are shown in in Fig. 2.7.

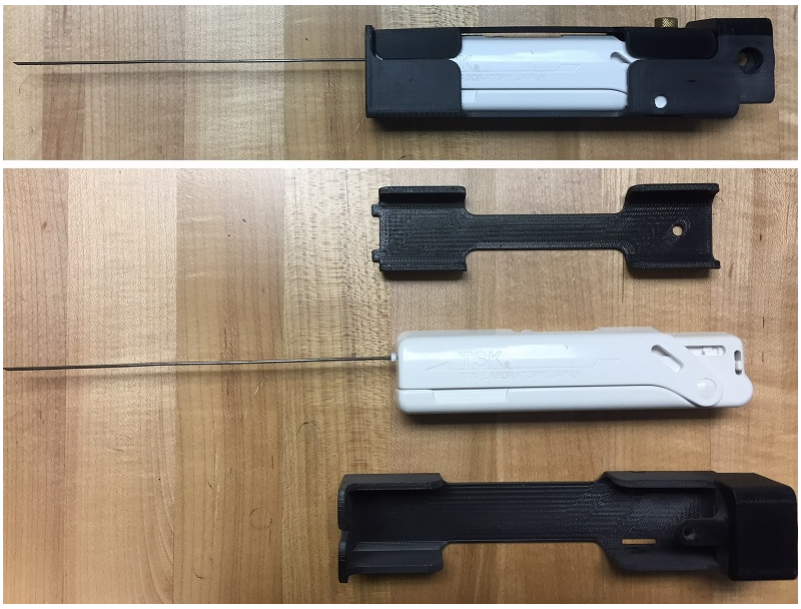

Figure 2.7: The clinical biopsy gun and the coupling assembly used to mount it to the robot. Top: the assembly of biopsy gun and coupling component used in the robot, Bottom: the individual pieces of the assembly

2.3.2 Robot Kinematics

The forward and inverse kinematics were implemented as described for the clinical base by Eslami et al. [99], with additional consideration for the added needle driver. Figure 2.8 shows a back and side view image of the robot describing kinematic parameters. Table 2.1 provides the values for these parameters and 2.2 describes the limits and resolution of motion for the developed needle driver.

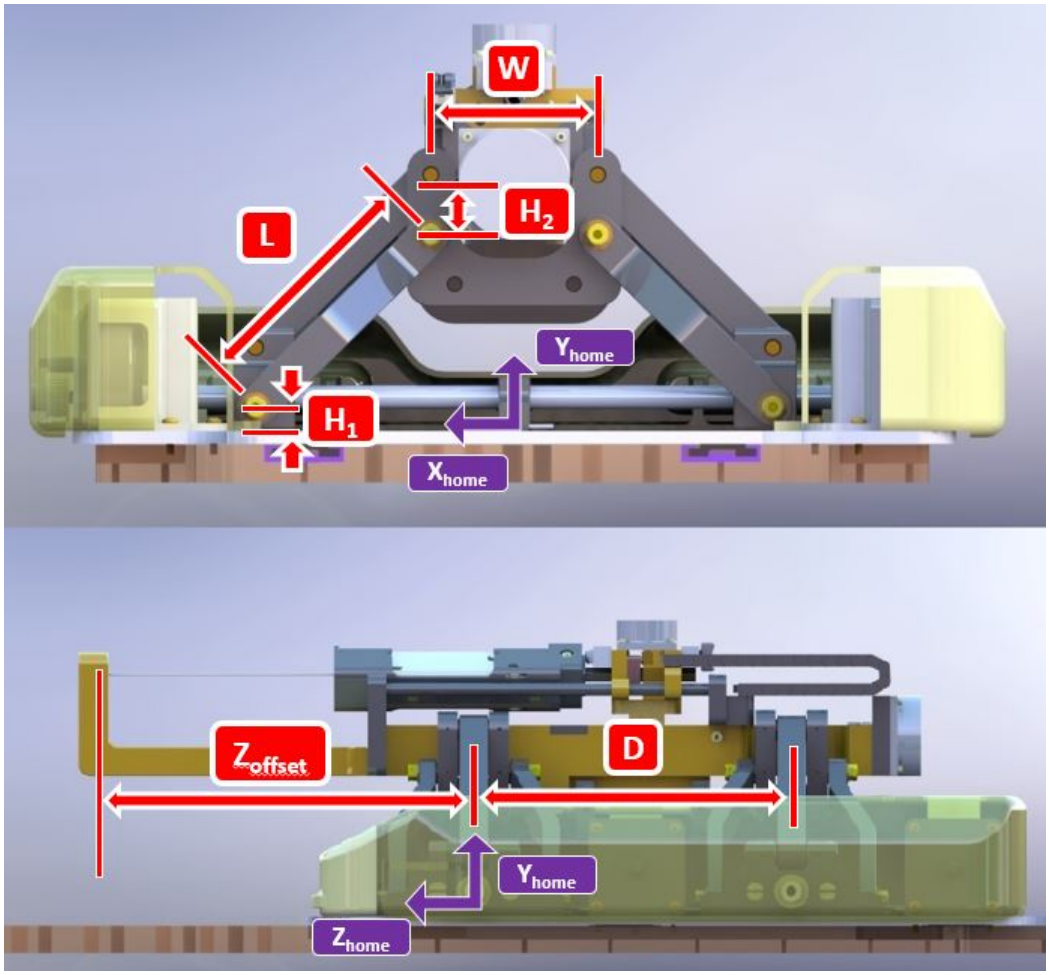

Figure 2.8: The kinematic parameters of the robot. The measurements used to determine the forward and inverse kinematics, with the values detailed in Table 2.1.

Table 2.1: Robot Kinematic Parameters

Parameter	**Specification**
L	$124mm$
W	$84mm$
H1	$12mm$
H2	$67.5mm$
D	$181.5mm$
Zoffset	$259.075mm$

Table 2.2: Needle Driver Specifications

Parameter	**Specification**
Insertion Range	$150mm$
Insertion Step Resolution	$1.2um$
Maximum Insertion Speed	$10mm/s$
Rotation Range	360^o
Rotation Step Resolution	0.072^o
Maximum Rotation Speed	$3rot/s$

2.3.2.1 Forward Kinematics

The forward kinematics describe the position and orientation of a robot's end effector with respect to each of the individual joint variables. In this case the needle tip position and orientation are described by the position of the four base joints: FrontLeft, FrontRight, BackLeft and BackRight, as well as the Insertion and Rotation joints of the needle driver. Each of these joints is labeled in Fig. 2.9.

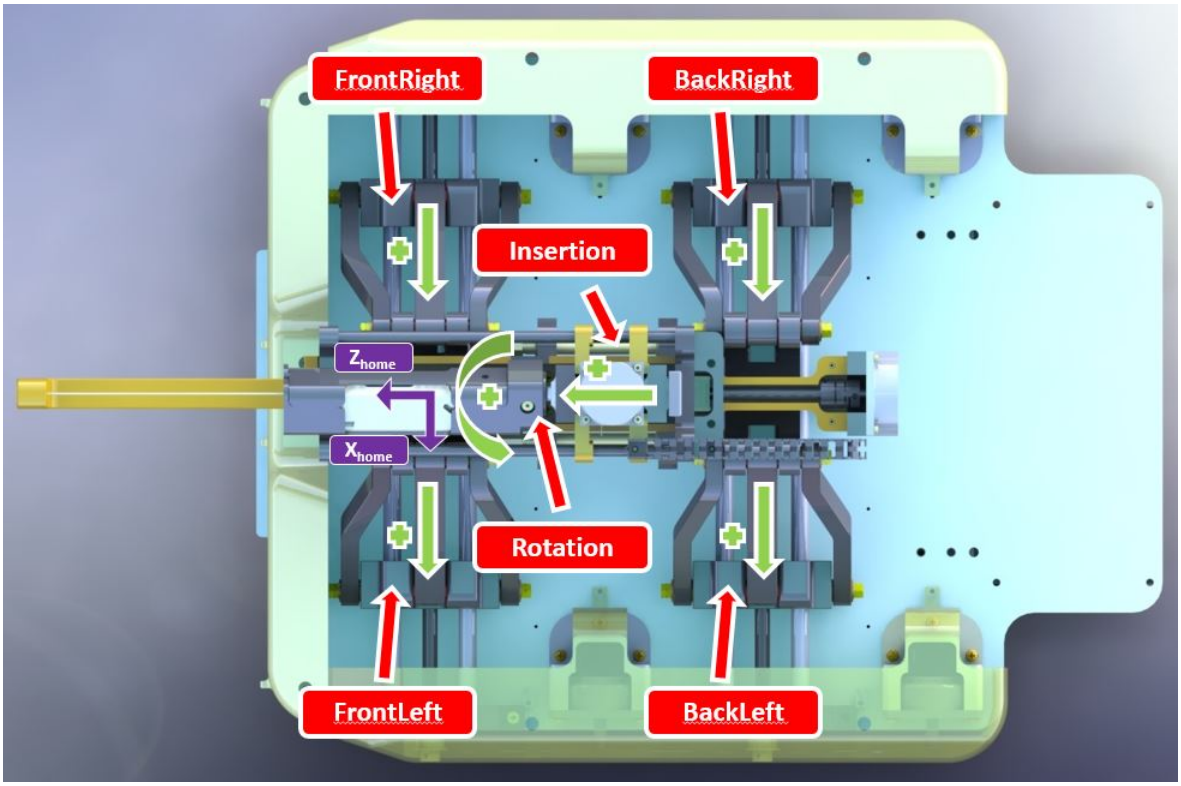

Figure 2.9: Each robot joint axis labeled with positive direction of motion. The projected robot base frame is also shown, with the positive X direction shown as robot base motion to the left, and the positive Z direction as needle insertion.

The forward kinematics were derived from the kinematic diagram shown in Fig. 2.10 [99]. Equations 2.1, 2.2 and 2.3 describe the location of the needle tip with respect to the robot home coordinate frame, labeled as "Front Origin" in Fig. 2.10.

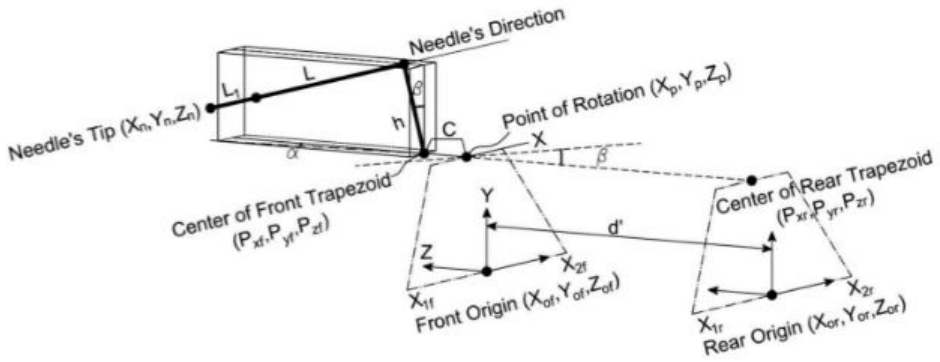

Figure 2.10: Kinematic Diagram of the 4-DoF robot base. [99]

For the four base joints, positive motion is described as movement to the left if looking along the needle axis from the robot to the needle tip. Needle insertion is described as positive movement for the Insertion joint, and counterclockwise rotation is described as positive motion for the Rotation joint. The kinematics for the robot base were implemented to allow for straight-line insertion trajectories, so positions of the FrontLeft and BackLeft joints are equal, as well as the FrontRight and BackRight joints. For this reason the joints FrontLeft and FrontRight are used to calculate the forward kinematics. Needle deflection will cause the tip-orientation to change throughout insertion, and compensating for this is covered in Chapter 5. Further kinematic analysis of the clinical 4-DoF base can be found in [99]

$$X_{tip} = \frac{(FrontLeft + FrontRight)}{2} \tag{2.1}$$

$$Y_{tip} = H_1 + H_2 + \sqrt{L^2 - (FrontLeft - FrontRight - W)^2} \tag{2.2}$$

$$Z_{tip} = Insertion + Z_{offset} \tag{2.3}$$

2.3.2.2 Inverse Kinematics

As opposed to forward kinematics, the inverse kinematics describes the required joint positions for placement of the end effector in a specific conformation. With a desired needle tip placement of $X_{desired}, Y_{desired}, Z_{desired}$ (along with a $3x3$ orientation matrix if an angulated insertion is desired), Equations 2.4, 2.5, 2.6, 2.7, 2.8 correspond to the joint variables for the FrontLeft, FrontRight, BackLeft, BackRight and Insertion axes respectively. Rotational position of the needle tip is directly set by the Rotation joint axis through image-feedback also described in Chapter 5.

$$FrontLeft = 0.5 * (2 * X_{desired} + W + 2 * \sqrt{L^2 + (Y_{desired} - H1 - H2)^2} \tag{2.4}$$

$$FrontRight = 2 * X_{desired} - FrontSlider1 \tag{2.5}$$

$$BackLeft = 0.5 * (2 * X_{desired} + W + 2 * \sqrt{L^2 + (Y_{desired} - H1 - H2)^2} \tag{2.6}$$

$$BackRight = 2 * X_{desired} - RearSlider1 \tag{2.7}$$

$$Insertion = Z_{desired} - Z_{offset} \tag{2.8}$$

2.4 Discussion and Conclusions

The needle placement system described in this chapter consists of a robotic manipulator suitable for use in the MR environment. The final design is a 6-DoF system consisting of a 4-DoF robot base and a novel 2-DoF cooperatively controlled needle driver configured for continuous hands-on needle insertion alongside closed-loop active compensation of deflection from an initial straight-line needle trajectory. The system was presented in consideration of design requirements for effective use in the MR bore with components such as piezoelectric actuation and aluminum cased load cells. The control system architecture is presented in the next chapter and the evaluation of the

entire system's effect on SNR is discussed in Chapter 6.

Chapter 3

An Adaptable Robot Controller Architecture

3.1 Introduction

This chapter introduces the robot controller architecture, an adaptable system for control of MRI-guided surgical robots. The design requirements for the controller are given, followed by how these were fulfilled by individual hardware and software subsystems.

3.2 Design Requirements

The requirements for the control system architecture included a controller capable of reconfigurable input/output robot control implementation, power management and communication between the control system and auxiliary software applications via the OpenIGTLink network communication protocol. It was throughout work on this dissertation that a shift to a new centralized architecture was required, as previous decentralized versions made synchronization between axes and implementation of accurate sensing and haptic feedback difficult. An additional requirement for reconfiguration was to ensure the controller was robot agnostic, applicable to future generations of this robotic manipulator and new systems altogether. The control box must enter the MR room with the robot so it must be adequately shielded, and a single shielded cable must be used to connect the controller to the robot.

3.3 Software Architecture

3.3.1 Robot Control

A reconfigurable control system for this robot was implemented on the sbRIO-9651 from National Instruments (Austin, TX, USA). This System on Module (SoM) contains an Artix-7 Field Programmable Gate Array (FPGA) from Xilinx (San Jose, CA, USA), as well as a proprietary Linux Real-Time Operating System running on an

ARM Cortex-A9 manufactured by National Instruments. This specific Reconfigurable Input/Output (RIO) architecture is based on a real-time operating system (RTOS) and the programmable hardware of an FPGA. The FPGA interfaces with the analog and digital I/O and communicates via a high-speed PCI bus to arm processor. This architecture is described visually in Fig. 3.1

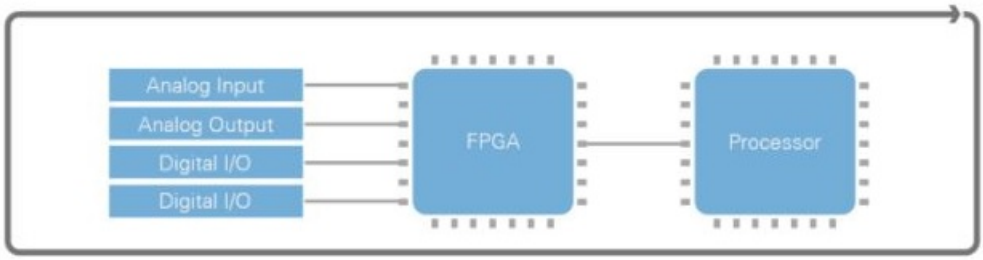

Figure 3.1: The National Instruments Reconfigurable Input/Output Architecture. The FPGA interfaces with the hardware for high-speed IO and communicates to the processor via PCI. ©National Instruments

The FPGA is programmed in National Instruments LabVIEW and and contains the low-level hardware I/O interface along with high-speed SPI communication. High-level robot command software can be programmed either in LabVIEW or in C/C++ on the RTOS as shown in Fig. 3.2, and in our case all high-level code was written in C++ with specific implementation discussed in Chapters 4 and 5.

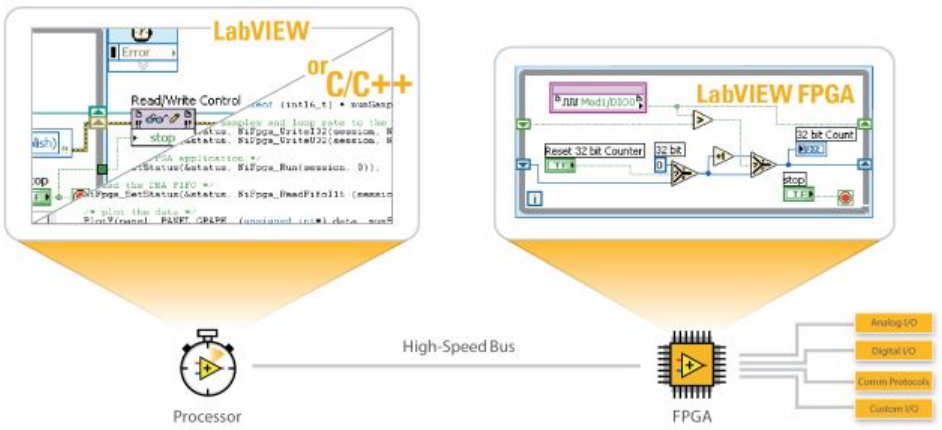

Figure 3.2: The programming options for the FPGA and ARM processor within the RIO architecture. ©National Instruments

3.4 Hardware Architecture

3.4.0.1 Circuit Assembly

The RIO architecture allows the system to be robot agnostic. An early implementation of the control system was based on a Compact Re-configurable Input/Output cRIO-9068 also from National Instruments. Similar to the sbRIO, the cRIO is a Linux based platform with an ARM Cortex-A9 processor running a RTOS and an on board Artix-7 FPGA for high-speed I/O. Instead of a SoM architecture, this system is part of a chassis which can interface with pre-built swappable modules which allow for high degrees of customization. The cRIO, along with several power supplies and a custom PCB for power distribution were built into the control box shown in

3.3. This system was not suitable for use in the MR environment, but allowed for proof-of-concept development using the RIO architecture.

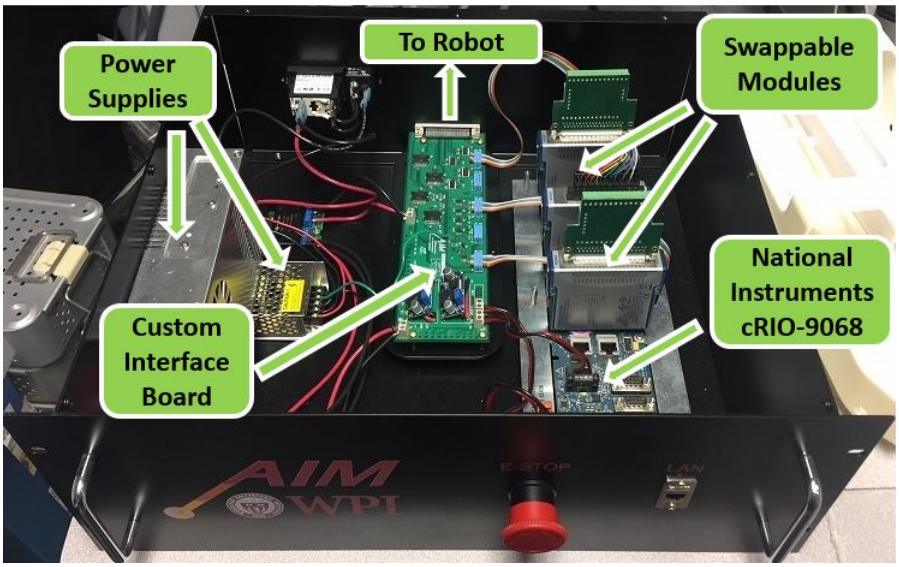

Figure 3.3: The first controller box developed, a non-dedicated non-MRI compatible version based on the cRIO-9068. This system from National Instruments uses the same FPGA/ARM processor architecture, instead using proprietary swappable modules for I/O.

With success of the cRIO based system, the sbRIO SoM was broken out on a custom backplane to develop a system suitable for use in the MR. The custom backplane contains 10 individual card slots, one corresponding to a daughter card for each functional robot axis. Figure 3.4 shows the layout of hardware architecture while 3.5 shows how this was realized in a PCB circuit assembly.

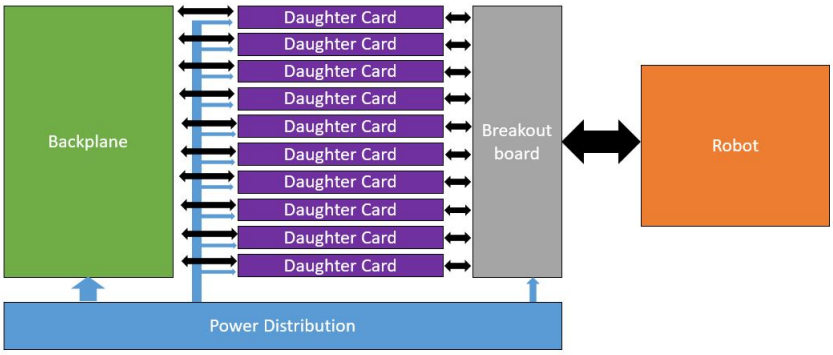

Figure 3.4: The hardware architecture in the robot controller. Swappable daughter cards correspond to each robot axis and can be rearranged to control different robot function.

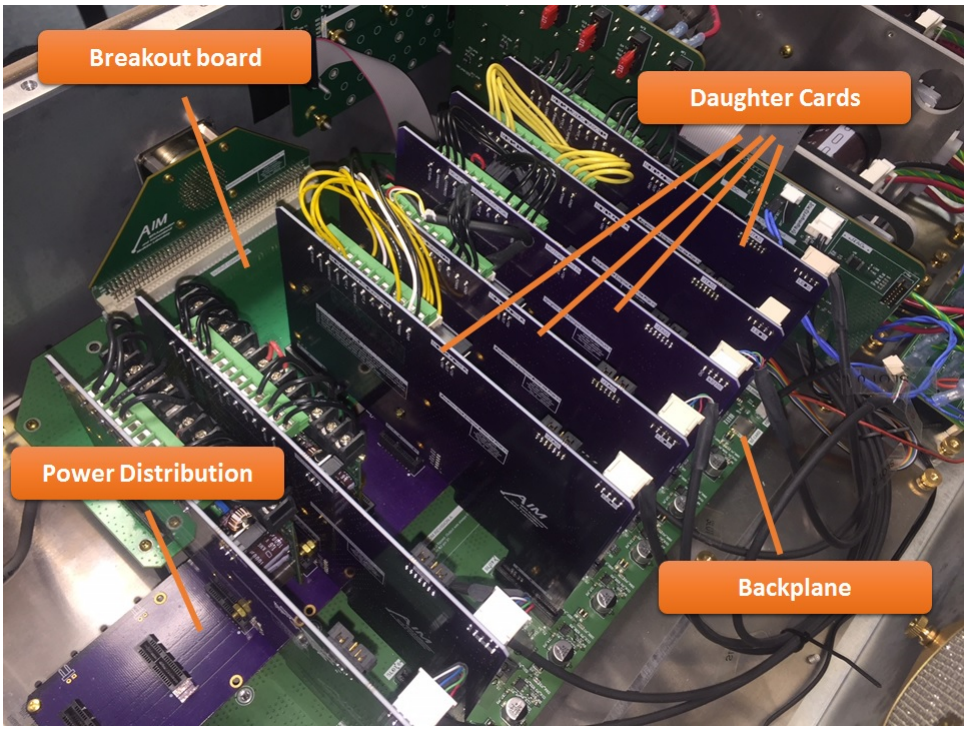

Figure 3.5: The realized circuit assembly inside the control box showing the backplane, power distribution board and swappable daughter cards.

The vertical daughter cards in figure 3.5 are the modular components of the control system architecture. Using the reconfigurable SoM broken out on a backplane, these cards can be replaced or rearranged to support control of any robot with up to 10 functional axes, where a functional axis is not limited to the motorized joint axes of the robot. In this system there are two types of functional axes implemented, motor control and force sensing, but additional types of daughter cards can be developed for new functionality such as control of interventional treatments directly. The two types implemented in this system can be seen in figures 3.6 and 3.7 for the motor card and sensor card respectively.

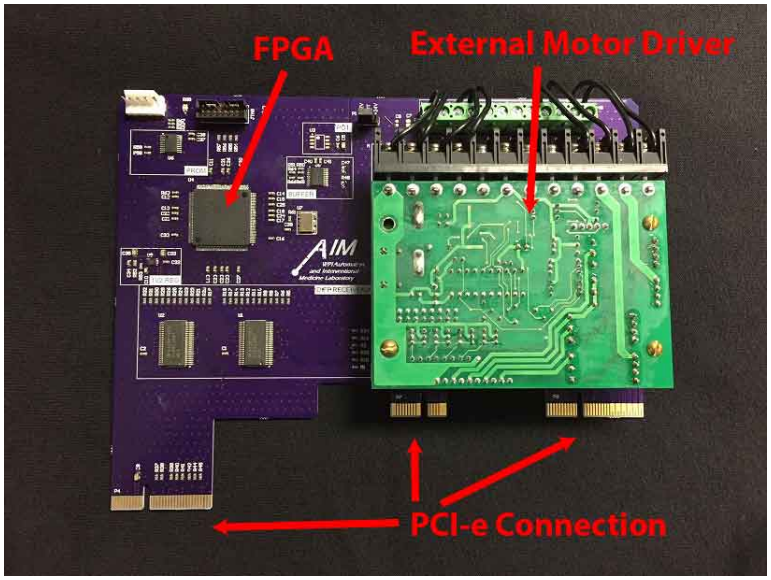

Figure 3.6: A type of motor control daughter card. This card has an FPGA which communicates to the backplane and uses an external Shinsei D060 motor driver.

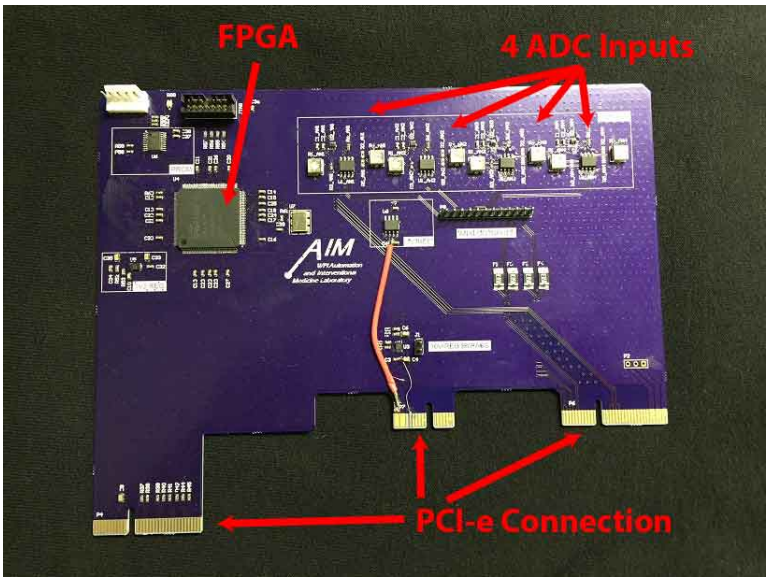

Figure 3.7: The force sensor daughter card. This card has an FPGA to communicate with the backplane and four ADC channels to input analog signals from the robot.

3.4.0.2 Power Requirements

Several levels of DC voltages are required to power each component of the system. To satisfy this requirement a set of low-noise switching power supplies were chosen to be placed directly inside the shielded controller box alongside the circuit assembly.

Three VIPAC Power Systems from Vicor Corp. (Andover, MA, USA) were selected to provide the necessary power to the robot and controller. These power systems have an AC/DC front end and up to 3 DC/DC converters to provide outputs are various voltage levels. An annotated image of the VIPAC power system is shown in Fig. 3.8. This system shows a configuration with three DC outputs.

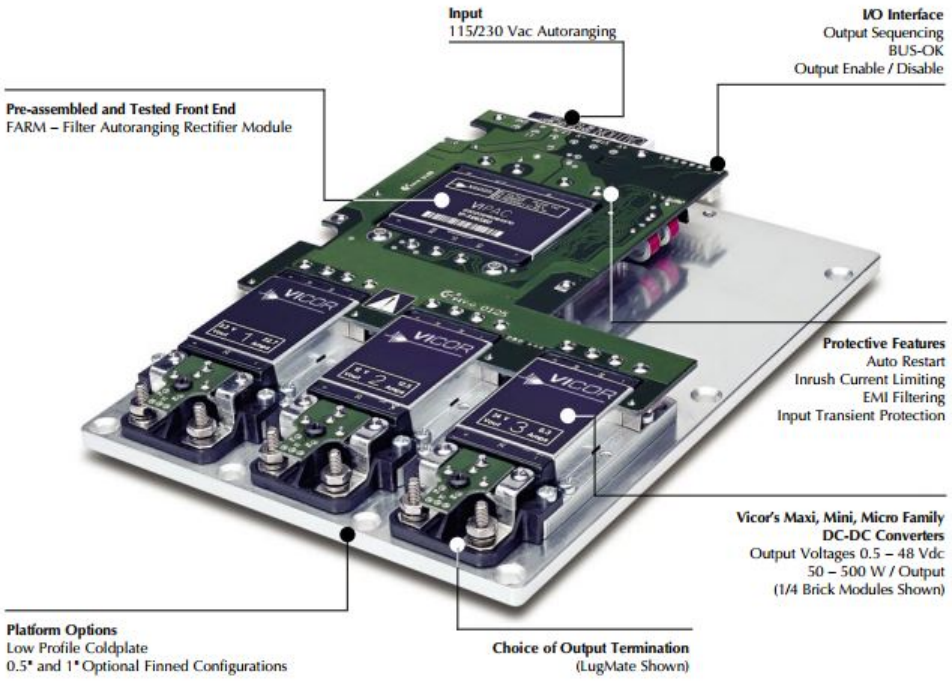

Figure 3.8: A description of the VIPAC power system. The system takes in an AC input and can provide between one and three DC outputs depending on the required specifications. ©Vicor Inc.

The VIPAC systems used in the control box to provide power are shown in Fig. 3.9 and consist of models: VP-A which has 3 DC outputs $5V, 12V, -12V$, VP-B which has outputs $24V$ and $24V$ to provide $24V$ and also used in series to provide $48V$, and VP-F which has a single $3.3V$ supply.

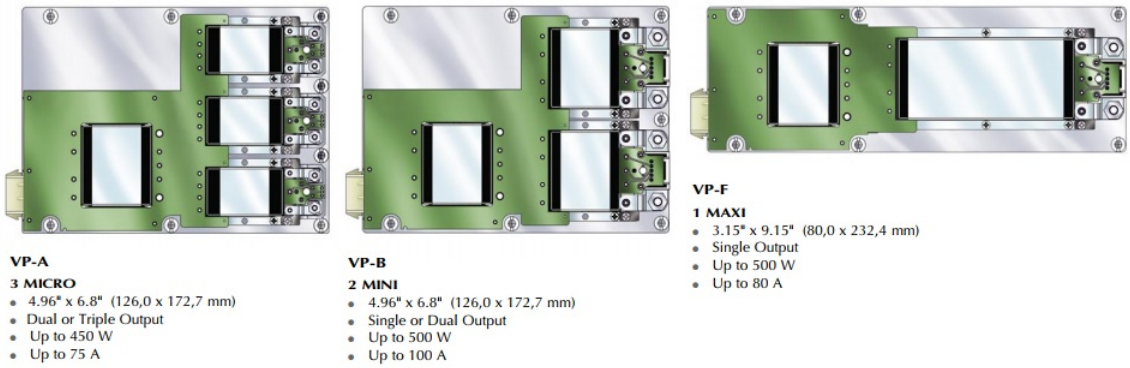

Figure 3.9: The three VIPAC power systems used in this system. The required voltages for the entire system are 48V, 24V, 12V, -12V, 5V and 3.3V. ©Vicor Inc.

3.4.1 MRI Compatible Controller Box

A custom shielded aluminum controller box was designed to house the circuit assembly, power supplies and peripheral components necessary to control the robot. The box enters the MR room with robot and stays outside of the 5 Gauss Line. Precautions were taken to limit EMI interference with the MR scanner by including specialized EMI blocking vents for heat dissipation and EMI gasketing along each the mating components. Each of the PCBs within the box had a a layer of shield on the top and bottom with via stitching connecting the layers along the entire PCB. In addition, the aluminum case was directly connected to shield creating a Faraday Cage around the control system. Communication to the control box from a host PC outside the MR room is achieved via a fiber optical cable through the scanner room

wave guide. A render of the design and photograph of the control box is shown in Fig. 3.10.

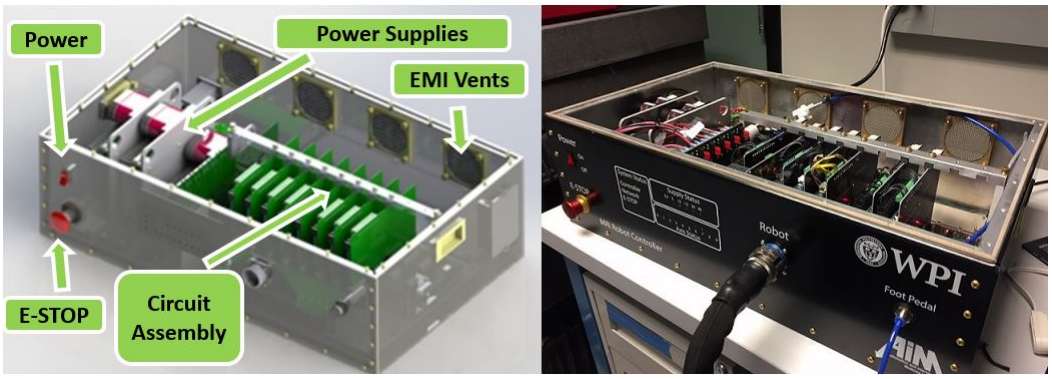

Figure 3.10: A render and photograph of the controller box developed throughout work on this dissertation. The controller contains the aforementioned power supplies and circuit assembly.

3.4.2 Custom Cable

A shielded connection between the controller and the robot was accomplished by a single $7.62m(25ft)$ long and 151 pin cable. This cable consisted of a set of smaller 12 conductor (6 twisted pair) cables for encoder and limit switch data, and 6 conductor (3 twisted pair) cable for motor actuation for each of the 10 possible robot axes. The encoder and motor cables were part numbers 78176 SL005 and 78173 SL005 from Alpha Wire (Leominster, MA, USA) respectively. Each end of the cable was fitted with a circular connector plug, part number TV06RF-23-151P-LC with gold contact pins 10-597331-735, both from Amphenol Aerospace Operations (Wallingford, CT,

USA). Figure 3.11 shows the cable at different stages of assembly.

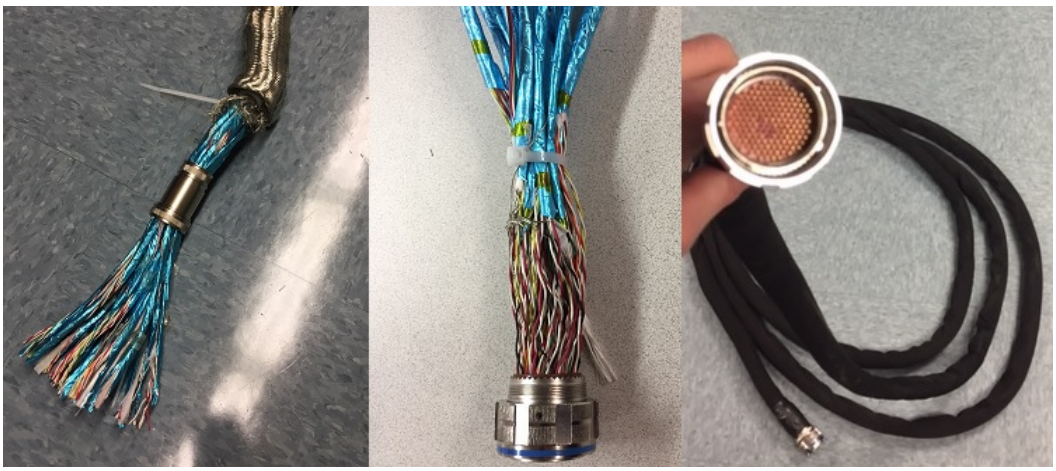

Figure 3.11: A series of photos showing assembly of the custom 151 pin cable which connects the controller box to the robot. The final product combines 16 smaller cables, 8 corresponding to motor function consisting of three sets of twisted paired wires, and 8 corresponding to encoder signals consisting of 6 sets of twisted paired wires.

3.5 Cross Platform Control of Stereotactic Neurosurgery

Throughout completion of this dissertation, the research group developed a separate robotic platform for MR-guided stereotactic neurosurgery, specifically closed-loop conformal thermal ablation of brain tumors [104–106]. This robotic system shares many of the same design requirements for use in the MR-bore as the needle

placement manipulator described in Chapter 2, and can be seen in position inside the scanner in 3.12. The reconfigurable controller presented in this chapter was required to control both the needle placement manipulator for prostate interventions, but also this MR-guided robot and other yet unrealized robotic systems.

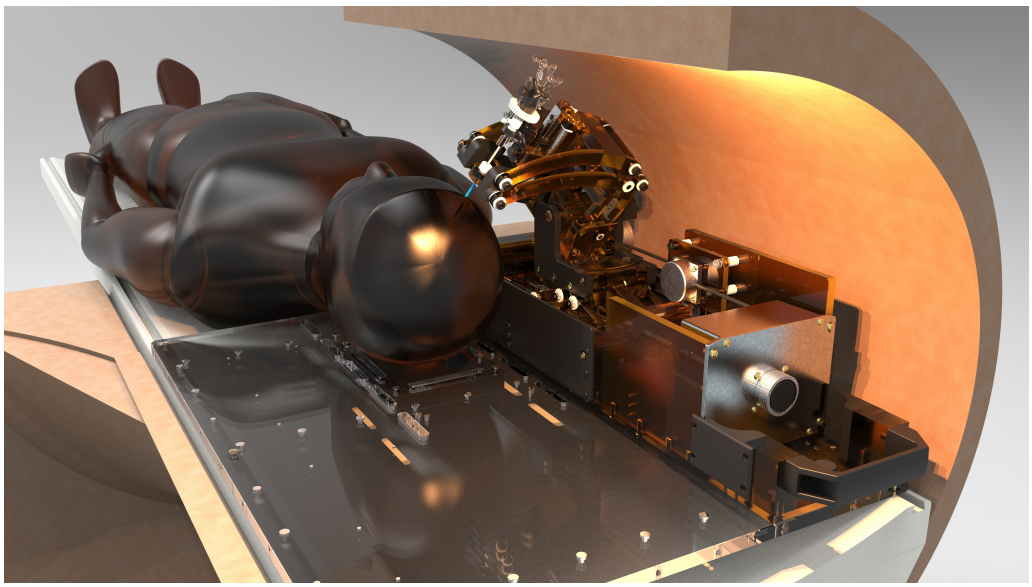

Figure 3.12: A render of a robot for MR-guided stereotactic neurosurgery in-development by the research group. The reconfigurable controller developed as part of this dissertation was required to be adaptable to both the needle placement manipulator described in Chapter 2 but also this MR-guided robot and others yet to be developed.

3.6 Discussion and Conclusions

The controller architecture is developed on a National Instruments SoM containing an FPGA and a RTOS running on an embedded Linux platform. This platform allows for rapid and reconfigurable development of algorithms as well as real-time deterministic execution of code. With high-speed I/O and low-level control loops running on the FPGA, high-level robot function is implemented in C++. The NI module sits on a custom backplane and circuit board assembly inside of an aluminum shielded control box and is connected to the robot via a shielded cable. The control system architecture was specifically designed for reconfigurability, with requirements to control both the needle placement robot for prostate interventions, and also a robot for MR-guided thermal ablation of brain tumors also development by the broader research group. The controller is paired with the needle placement robot for SNR evaluation in Chapter 6.

Chapter 4

Cooperative Control

4.1 Introduction

Physicians use tactile feedback throughout needle insertion to perceive needle tip localization within anatomical structures. A cooperatively controlled needle insertion would enable providing a physician with augmented haptic feedback to restore this perceived localization, without distancing the physician from the patient. The admittance based cooperative control algorithm is presented along with a description of the control strategy and how it was implemented for robotic needle insertion. A paired force-sensor and image-guided technique to provide augmented haptic feedback at membrane puncture is also presented. Furthermore, for valid research outcomes, phantoms used for needle insertions must accurately mimic the mechanical properties of pelvic tissue. Therefore phantoms were developed and characterized to match

mechanical properties using ultrasound elastography. Finally, the results of in lab experiments for membrane puncture detection under cooperative control are shown.

4.2 Hands-on Cooperative Insertion

4.2.1 Cooperative Control Algorithm

The technique for hands-on cooperative needle insertion is based on collecting user force input as well as forces seen on the needle during insertion. By collecting both the user input force, F_{input}, as well as the forces seen on the needle, $\sum F_{needle}$, continuous augmented haptic feedback can be provided during cooperative needle insertion by adjusting the insertion velocity as a function of the two.

The forces seen on the needle are comprised of three components: the cutting force, the stiffness on the tip, and the friction force along the length of the needle [76]. Separating these forces is possible, for instance by using Fiber Bragg grating [86], but this is not feasible in a scenario where altering an already regulatory approved clinical biopsy needle is not an option. Instead, these forces are collected as one collective measurement at the proximal end of the biopsy gun.

The implemented cooperative algorithm was developed based on a velocity curve with a decaying exponential, where the sensitivity of the difference of forces can be scaled by an exponential decay constant λ. With the difference of forces in $Newtons$ defined as F_δ in Equation 4.1, the cooperative control scheme showing the insertion

velocity in mm/s is described in Equation 4.2.

$$F_\delta = F_{input} - \sum F_{needle} \tag{4.1}$$

$$v_{insertion} = \begin{cases} v_{max}(1 - 0.9e^{-\lambda(F_\delta)}), & F_{input} > \sum F_{needle} \\ 0.1v_{max}, & F_{input} < \sum F_{needle}, F_{input} > 0 \\ 0, & \text{otherwise} \end{cases} \tag{4.2}$$

Increasing the magnitude of λ leads to an increased insertion velocity during initial insertion with higher sensitivity between F_{input} and $\sum F_{needle}$ as their values approach each other. The goal of this algorithm is not transparent haptic sensation, where the forces seen on the needle are accurately reflected to the user, but instead providing augmented feedback at event based boundary transitions. This algorithm gives the user control of insertion speed through a force input, while increasing the sensitivity of tactile feedback as the needle force approaches this input. This situation is typically seen at the transition between tissue boundaries when needle force spikes, and could allow sensing of boundary transitions that could not have been able to be felt by the user alone. This inherently makes the system non-transparent, instead allowing for additional augmented feedback to be implemented at event detection such as these boundary transitions or forbidden regions corresponding to specific

anatomical structures to avoid. Figure 4.1 illustrates a series of velocity curves for cooperative insertion based on varying the value of λ. The non-zero y-intercept along with the second condition of motion were added empirically to avoid discontinuities of movement while an intent of insertion was present if, for instance, needle force grew larger than the input force for the user.

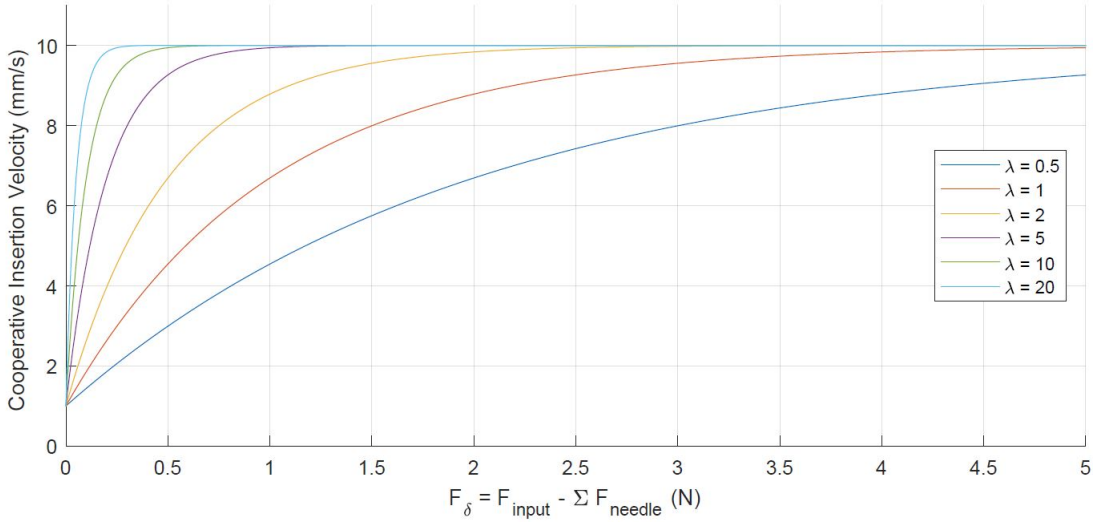

Figure 4.1: The velocity curve of cooperative insertion based on the exponential decay constant λ. As lambda increases the insertion velocity increases early during insertion and the sensitivity increases as the input and needle forces approach each other.

4.2.2 Cooperative Insertion Implementation

Cooperative needle insertion was implemented through admittance based closed-loop velocity control. Admittance control provides a velocity output to a force input, suited ideally for cooperative control. A block diagram describing cooperative inser-

tion is shown in Fig. 4.2. There are two inputs, a target depth and a user applied force input. First, F_δ is determined by subtracting the needle force from the applied input force. Then the current needle tip position is subtracted from the target depth to determine if the target depth has been reached. If it has then insertion stops, if it hasn't then F_δ is passed to the cooperative controller to determine the insertion velocity based on Equation 4.2. An inner proportional-integral-derivative (PID) control loop with velocity feedback maintains the desired set point insertion velocity based on the cooperative controller output. An insertion velocity produces an increased insertion position that is fed back to make the supervisory control loop decision. Finally, as the needle inserts deeper into the tissue the force seen on the needle increases, and this needle force is fed back to the beginning of the control loop in determination of F_δ.

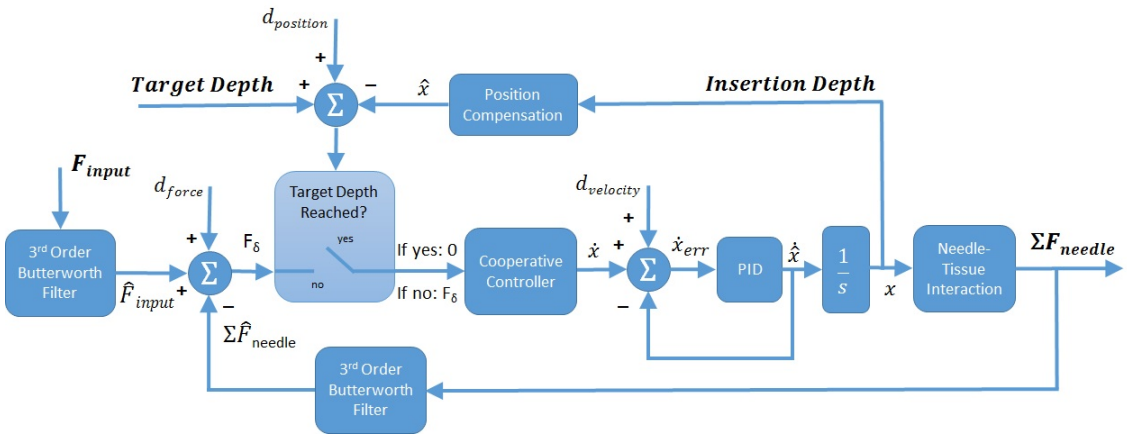

Figure 4.2: A block diagram showing the implementation of cooperative needle insertion. Closed-loop velocity control maintains a setpoint based on force values with a supervisory position loop to cease insertion at the target depth.

Sensor noise or mechanical disturbances can affect the control decision in each instance where feedback is used. A PD controller is implemented to maintain the desired velocity, while position compensation is performed via the image tracking software. In the case of force collection, both the input and needle force readings are filtered using a third order embedded Butterworth filter. A third order filter was chosen empirically to minimize delay with acceptable smoothing of the raw signal.

4.3 Membrane Puncture Detection

Through adaptation of a robotic needle insertion, the tactile forces typically used for anatomical localization are lost. By implementing membrane puncture detection this information can be provided to the physician in the form of an enhanced augmented haptic feedback during cooperatively controlled needle insertion.

Several options are available for providing an enhanced feedback response to the user at the puncture event. Most simply, the robot could be made to stop at a detection, or perhaps withdrawn slightly to account for tissue relaxation. Vibrotactile feedback could be implemented with the use of an additional actuator, or during cooperative insertion a short ($< 100ms$) freeze of the insertion axis can provide a haptic response related to the puncture. Furthermore, auxiliary feedback such as visual or audio cues can be implemented to inform the user of a puncture event, as experiments have shown humans reacting faster to sound [107], although [108]

showed vibrotactile feedback may be the most suitable for haptic systems using the same channel for input and output, which most closely reflects the system presented herein.

4.3.1 Detection Algorithm

Continuous augmented force feedback is presented to the user via an input velocity dependent on input force and needle-tissue interaction, but an additional haptic response can be provided to the user at the detection of a membrane puncture event. This system uses imaging to localize the depth of a membrane and provide a window to monitor the needle force data for detection of a puncture event. Anatomical structures seen in imaging can provide baseline information for the location of a membrane such as the prostate capsule. Furthermore, typical imaging sequences used in MRI interventions cannot determine puncture in real-time and can only verify puncture in a confirmation image. Robotic insertion to a depth cannot guarantee a puncture has occurred due to tissue deformation and needle deflection realizing a needle tip location that cannot be accurately described exclusively by robot kinematics.

In our case, the system can take advantage of its inherent workflow within the MRI to localize a predicted puncture location. Membrane and capsule depths within the insertion plane will be visible in pre- and intra-operative imaging, and depth information can be sent to the robot when registered to the scanner coordinate frame. If real-time needle force sensing is added in compliment, a windowed estimate for the

desired membrane depth can be paired with sensor data to look for a puncture event around that location.

In cases of multiple membranes or noisy sensor data, probabilistic models can perform better than simple thresholding to separate a true puncture event from other needle-tissue interactions [84]. A more complex model may not be necessary when searching for a puncture event in real-time, if the location of expected puncture can be narrowed as is done here. While within the expected window, simple membrane puncture can be identified by observing the square of the derivative of the needle force measurement:

$$((\sum F_{needle(k)} - \sum F_{needle(k-1)})/\Delta T)^2 \tag{4.3}$$

A graph of needle force and the square of the derivative through two puncture events in a phantom are illustrated in Figure 4.3. Within the window puncture is detected by double thresholding as shown in Equations 4.4 and 4.5. Detection begins with the square of the derivative crossing the puncture threshold, $T_{puncture}$, shown in the figure in red and determined experimentally based on the mechanical properties of tissue.

$$(\Delta F_{needle})^2 > T_{puncture} \tag{4.4}$$

Once the puncture threshold has been crossed, the square is multiplied by the sign

of the derivative to allow for zero crossing to be detected. When the zero crossing is detected the puncture has occurred.

$$sgn(\Delta F_{needle})\text{x}(\Delta F_{needle})^2 < 0 \tag{4.5}$$

In Fig. 4.3, thresholding would detect the punctures shown at depths of $36.66mm$ and $65.84mm$, but would trigger a puncture detection around $72mm$ as well. By using image data, the windows shown in the figure limit the search region eliminating the false positive. This puncture detection algorithm was implemented in C++ and it's implementation using pseudo code is shown in Algorithm 1

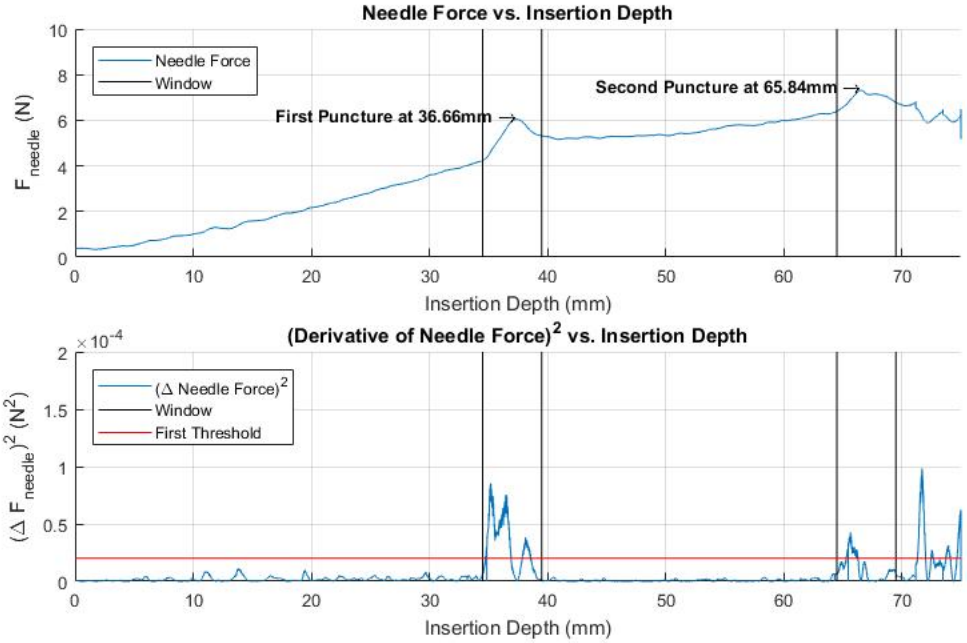

Figure 4.3: A graphical representation of membrane puncture detection. A needle insertion trial data into a phantom of layered samples soft-stiff-soft. The black vertical lines represent the window provided from imaging the phantom. Both membrane punctures were detected at 36.66mm and 65.84mm, with the windowing successfully able to filter out a false positive after the second puncture.

```
if a membrane is selected in imaging for puncture detection then
    proceed with needle insertion;
    if the needle tip is within the estimated window then
        start watching the needle force;
        if the square of the derivative of needle force is greater than first
         threshold then
            first threshold crossed;
        end
        if first threshold crossed then
            multiply the derivative of the needle force squared by the sign of
             the derivative;
            if the signed squared derivative of force crosses below zero then
                second threshold crossed, PUNCTURE DETECTED;
            end
        end
    end
end
```

Algorithm 1: Double threshold technique to determine when membrane puncture has occurred within the estimated window

4.4 Materials for Function Validation

To accurately reflect needle forces and have realistic results for haptic development with intent towards clinical translation, mechanical properties of phantoms and realistic forces seen in the target procedure must be replicated. Tissue phantoms were constructed with different concentrations of Plastisol liquid polyvinyl chloride (PVC) and PVC Softener from M-F Manufacturing (Fort Worth, TX, USA). Use of this material for developing tissue phantoms was described in [109] and also used in [86, 110] to mimic soft tissue for needle insertion experiments.

4.4.1 Tissue Phantom Characterization

The Young's Modulus of excised prostate tissue has been reported in the range of $16.0 \pm 5.7kPa$ for healthy and $40.6 \pm 15.9kPa$ for cancerous tissue by Hoyt et al. [111], while Ahn et al. [110] reported $17.0 \pm 9.0kPa$ and $24.1 \pm 14.5kPa$ for healthy and cancerous respectively. Samples with concentrations of Plastisol/Softener of 100%/0%, 80%/%20 and 60%/40% were molded and each was tested using ultrasound elastrography to determine the Young's Modulus directly. Testing was performed at Brigham and Women's Hospital using an ultrasound machine from GE (Boston, MA, USA) model LOGIQ E9. Ten measurements were taken for each sample and the relationship between %softener added and the Young's Modulus changed linearly. Figure 4.4 shows the experimental setup used to collect Young's Modulus data, while 4.5 shows

the linear results, with the measurements taken summarized in Table 4.1.

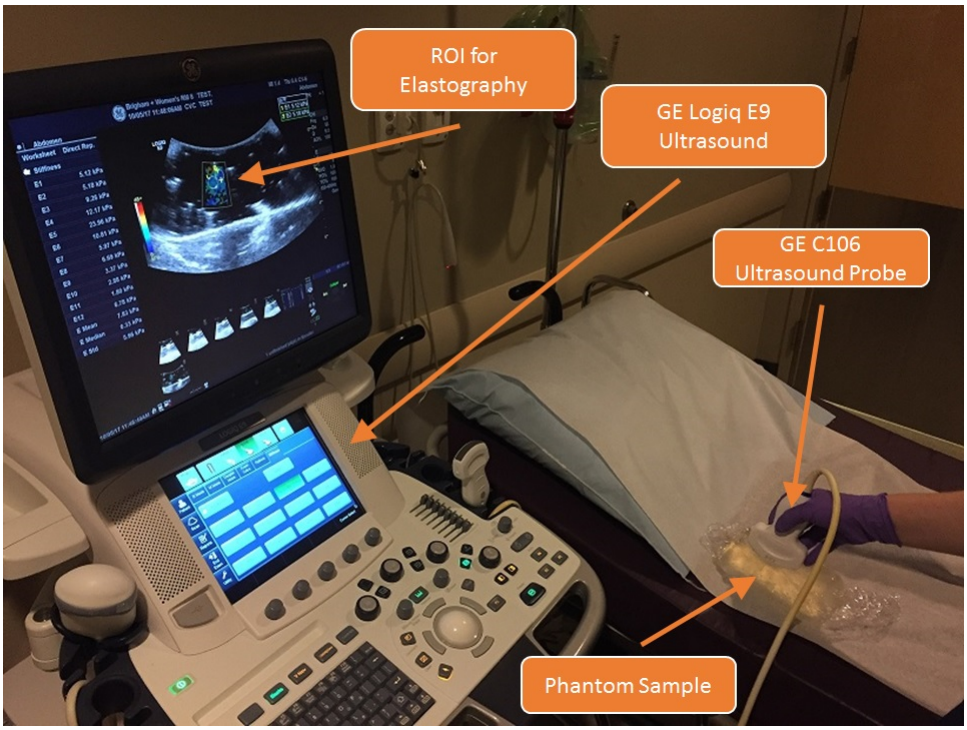

Figure 4.4: Characterization of materials for phantom construction using ultrasound elastography. Several concentrations of liquid Plastisol PVC and PVC softener were tested at Brigham and Women's hospital to determine their mechanical properties for phantom construction.

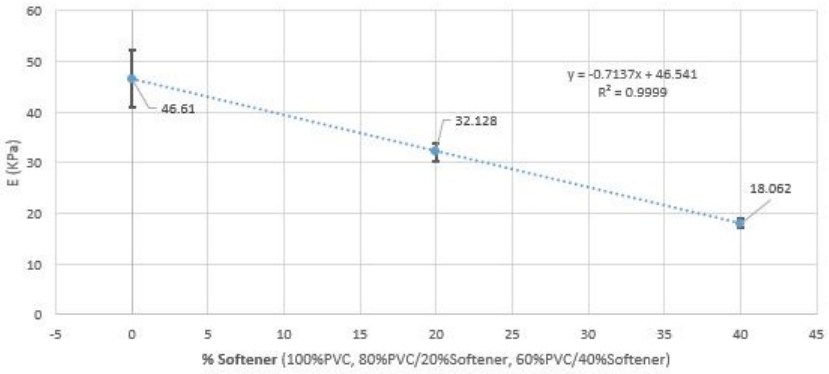

Figure 4.5: The results of material characterization using ultrasound elastography. The Young's Modulus changed proportionately to the concentration of PVC softener added.

Table 4.1: Ultrasound elastography results for mixed PVC concentration samples (kPa)

%PVC/%Softener	**1**	**2**	**3**	**4**	**5**	**6**	**7**	**8**	**9**	**10**	**Mean**	**StDev**
60/40	18.37	17.27	18.52	17.97	18.71	16.37	19.16	18.8	17.73	17.72	18.06	0.08
80/20	33.42	28.79	33.02	30.69	32.1	31.24	35.18	31.25	31.7	33.89	32.13	1.73
100/0	52.42	44.88	41.34	41.73	57.31	51.45	50.87	43.06	40.81	42.23	46.61	5.57

4.4.2 Interaction Forces during Needle Insertion

Along with the Young's Modulus, needle interaction forces seen during insertions in phantoms of this material must mimic froces seen in clinical interventions. Using an $18AWG$ needle, Podder et al. [112] measured an average *in vivo* needle force of $8.87N$ outside and $6.28N$ inside the prostate respectively, citing the differences due

to softer tissue within the prostate. After consideration of the elastography results alongside preliminary tests of needle forces seen during insertions, two concentrations were chosen to move forward, a 70%/30% ($\sim 25kPa$) concentration to mimic perio-prostatic tissue, along with a 60%/40% ($\sim 18kPa$) concentration for characterization experiments requiring variable tissue stiffness. Here forward samples of these concentrations will be referred to as the *stiffer* sample for 70%/30% concentration and *softer* sample for the 60%/40% concentration.

A series of constant velocity automated needle insertions were performed into the selected stiffer and softer phantoms in the lab. Five insertions were performed at constant velocities of $2mm/s$, $6mm/s$ and $10mm/s$, with results plotted in Fig. 4.6. Forces were seen in range of the *in vivo* data presented previously [112], with average forces in the stiffer phantom reaching between $5.5N$ and $6.5N$, while the softer phantom reached between $1.5N$ and $2.5N$ across all velocities. Additionally, increased insertion velocity showed an increase in average needle force throughout the length of the phantom, with increased velocity appearing to have more effect on the forces seen in softer phantom.

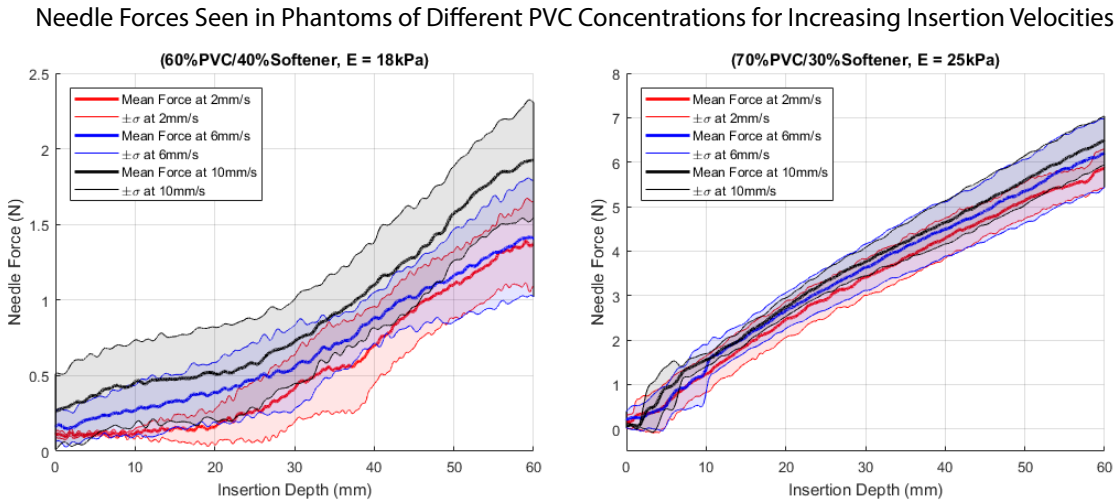

Figure 4.6: The $\sum F_{needle}$ seen during insertions at constant velocities $2mm/s$, $6mm/s$ and $10mm/s$ into phantoms of different concentrations. Forces seen on the phantom of 60%/40% Plastisol to Softener concentration reached an average max force near $2N$ for insertions at $10mm/s$, while those in the 70%/30% phantom reached almost $7N$

4.4.3 Heterogeneous Phantom Development

After the material concentrations were chosen and characterized through preliminary insertions, heterogeneous phantoms mimicking pelvic structures were constructed. First, anonymized MRI images from clinical prostate biopsy procedures were used to segment periprostatic structures. Using 3DSlicer, each structure can be segmented throughout the entire set of image slices and a 3D reconstruction can be

developed. A sample slice of an image set along with the 3D reconstruction created from it is shown in Fig. 4.7. The needle path of a biopsy taken can be determined through selecting the needle artifact in each slice using the CurveMaker plug-in for 3DSlicer.

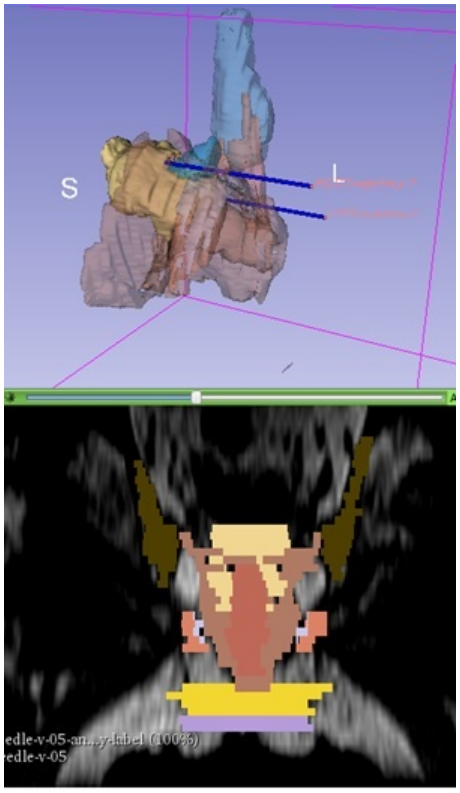

Figure 4.7: Segmentation of anatomical structures in 3D slicer. Bottom: 2D segmentation of each structure, Top: the 3D composite image of structures defined in each slice.

After the region was fully segmented, .STL files of individual structures were used to created Computer Aided Design (CAD) models of molds for each. These molds were 3D printed and individual structures were molded using the 70%/30%

concentration, with pigmented dyes to create heterogeneous phantoms with distinguishable characteristics. The 3D printed molds for the prostate, corpus spongiosum and bulbospongiosus are shown on the left of Fig. 4.8. The figure also shows a set of structures molded from these molds and a heterogeneous phantom molded using the individual structures.

Figure 4.8: Molds of anatomical structures created from segmenting anonymized MR images. Left) The 3D printed molds, Center) structures molded from PVC, Right) a heterogeneous phantom assembled from the molds.

4.5 Validation Studies

The system was developed and validated in the lab setting. The insertions were performed on an optical table in view of two perpendicularly mounted camera as seen in Fig. 4.9. The puncture detection algorithm was tested on two sets of phantoms, both three layered with a thin polyimide sheet placed between each layer to act as a

membrane. The difference between the phantom sets were the order of layers, with one being soft-stiff-soft, and the other stiff-soft-stiff. The "soft" and "stiff" characteristics of the layers correspond to those in the previous section.

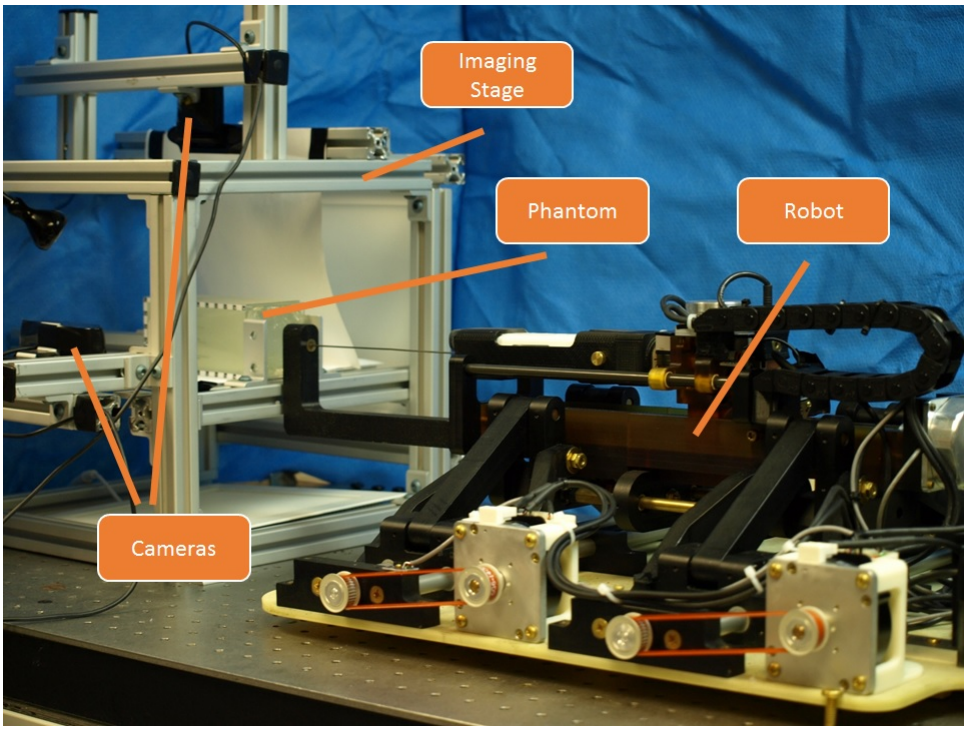

Figure 4.9: The in-lab experimental setup for membrane puncture detection. The robot is secured to an optical table along with an imaging stage which holds the phantom and two perpendicularly mounted cameras.

Twenty-five cooperatively controlled needle insertions were performed into each type of phantom. The first hypothesis was that detecting puncture will be more difficult for transitions occurring at a greater insertion depth and the second hypothesis was that detecting puncture from the soft sample to the stiff sample will be more difficult than from stiff to soft. The results are summarized in Table 4.2.

The results indicate that detection of membranes deeper along the insertion axis may be inherently harder to detect because overall needle force is greater, so the difference seen by a membrane puncture may not be significant enough to trigger detection. Furthermore, the second hypothesis stating detection of puncture from a softer tissue to a stiffer one would be more difficult than vice versa was confirmed, when this transition occurs deeper in insertion. This hypothesis was made considering the work by [81], where it was found that a needle traversing an internal tissue boundary can cause rupture (i.e. significant force change), if the tissue of the new tissue layer is significantly lower than that of the current layer.

Table 4.2: Success of Puncture Detection During Cooperatively Controlled Needle Insertions

Type	**Location**	**Success Rate**
soft $\rightarrow$ stiff	shallow ($< 50mm$)	88%
soft $\rightarrow$ stiff	deep ($> 50mm$)	68%
stiff$\rightarrow$ soft	shallow ($< 50mm$)	88%
stiff$\rightarrow$ soft	deep ($> 50mm$)	80%

4.6 Discussion and Conclusions

In this chapter the cooperative control algorithm was presented. This algorithm determines the needle insertion speed based on the difference between the applied input force and the force seen on the needle within the tissue. It is based on a decaying exponential with variable decay constant λ. By changing λ the effects of the difference between the difference of forces can be altered, allowing for a faster insertion speed early on in insertion and higher sensitivity when the forces approach each other. The control loop used to implement cooperative control was shown, in which the input force and target depth are the two inputs and the needle force and needle tip position are the two outputs.

Additionally, a technique for puncture detection using a paired imaging and force sensing technique was presented. With an encoded robotic insertion axis, puncture of a specific membrane cannot be guaranteed exclusively with kinematic output due to needle deflection and anatomical shift. By pairing imaging information to provide an estimate of membrane location with real-time force data, accurate detection of membrane puncture can be observed without the necessity for complex probabilistic models. Furthermore, pairing imaging with force sensing to localize puncture of a specific membrane can assist in localization within an anatomical structure, if a haptic response is provided upon detection. This response could vary based on requirement, for instance the needle could be made to stop upon a puncture event or could be automatically withdrawn slightly to account for tissue relaxation after puncture. [75].

To obtain meaningful results for clinical translation, tissue phantoms mimicking mechanical properties of the periprostatic region were developed and characterized. Characterization was performed with ultrasound elastography to mimic the Young's modulus while needle insertion tests were performed to match the forces seen during clinical procedures. Once the materials were characterized, heterogeneous phantoms were created by segmenting anatomical structures from anonomized MR images and 3D printing molds for individual structures.

Chapter 5

Targeting via Image Based Feedback

5.1 Introduction

This chapter focuses on closed-loop image-guided robotic needle tip placement and active compensation for deviations from an initial straight-line needle insertion trajectory. Here we introduce the methodology with in-lab validation, and extension of this work to in-bore MRI trials is presented in Chapter 6. Compensation is accomplished through rotational bevel tip positioning and control is completely independent from the imaging modality used. Registration and feature localization are described in reference to the laboratory setup, using a standalone software application to determine needle tip and target localizations. This information is passed one-way downstream

to the robot controller via the OpenIGTLink communication protocol, an open network interface for image-guided therapy [113]. A description for closed-loop active compensation based on rotational bevel tip positioning is presented, which accepts transforms of coordinate registered tip and target locations enabling it to be agnostic to the imaging system used. In-lab validation results for targeting both stationary and shifted targets are presented.

5.2 Registration

With an ultimate goal of MRI feedback for accurate needle tip placement, in-lab validation of the robotic system was performed using two perpendicularly mounted cameras to act as a proxy for multi-planar MR images. Registration is performed prior to any targeting through a marker rigidly attached to the robot and in view of the image frame, with Equation 5.1 showing the sequential multiplication of transformations required to register the imaging systems coordinate frame to the current pose of the robot. In Equation 5.1, ${T_{RobotPose}^{RobotBase}}^{-1}$ is the transformation from the current pose of the robot to the robot home coordinate frame, $T_{Registration}^{RobotBase}$ is a constant matrix describing the transformation from the robot home frame to the registration marker, while ${T_{Registration}^{Image}}^{-1}$ is also a constant matrix describing the transformation from the registration marker rigidly attached to the robot to the imaging coordinate frame.

$$T_{Image}^{RobotPose} = T_{RobotPose}^{RobotBase\,-1} T_{Registration}^{RobotBase} T_{Registration}^{Image\quad -1} \tag{5.1}$$

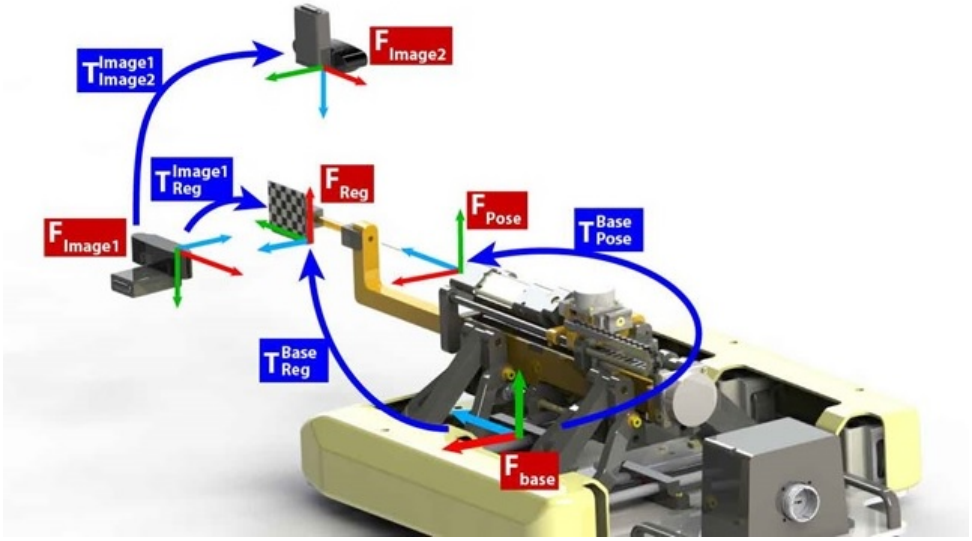

Figure 5.1: The coordinate systems and frame transformations used for robot to image-guidance registration. The checkerboard marker used to register the the robot to the cameras is removed before needle insertion begins.

5.3 Feature Localization

The active compensation technique is agnostic to imaging modality, and in previous work we have demonstrated needle tracking in MRI coupled with active scan plane geometry control [94]. With the focus here on developing active compensation during cooperatively controlled insertions in the lab, we use a standalone software application using two orthogonal USB cameras, models C920 from Logitech (Lau-

sanne. Switzerland); this serves as a proxy for medical imaging to provide real-time 3D coordinates of the needle tip and target within the robot workspace. Each image has a resolution of 640 x 480 pixels and two-dimensional localization of the moving needle tip is found by analyzing pairs of sequential video frames using the dense optical flow algorithm [114]. For the purposes of demonstrating the active compensation technique, the target point is either selected manually or segmented by color in the camera images, while target orientation is set to a nominally straight trajectory from the entry point. The output of both needle and target localization are homogeneous transforms for the position and orientation of each.

Validating the accuracy of feature localization must be performed to confidently use the needle tracking outputs for robot control. A series of five controlled needle insertions were performed into a homogeneous phantom made with the 70%/30% ratio of plastisol and softener to test the accuracy of needle localization. Error was found by subtracting a ground truth coordinate found by manual selection of the needle tip in each video frame from the coordinate calculated through the optical flow needle tracking algorithm. With camera resolution 640x480 pixels, the root mean square (RMS) error over the length of all insertions was $10.78 pixels_{rms}$ along the needle insertion path and $1.05 pixels_{rms}$ perpendicular to the insertion path, corresponding to $2.65 mm_{rms}$ and $0.12 mm_{rms}$ at the phantom boundary respectively. Figure 5.2 illustrates the tracking error found throughout insertions over all trials. Error along the axis of needle insertion is greater because the insertion itself creates substantially

more motion along that axis as opposed to perpendicular motion from deflection.

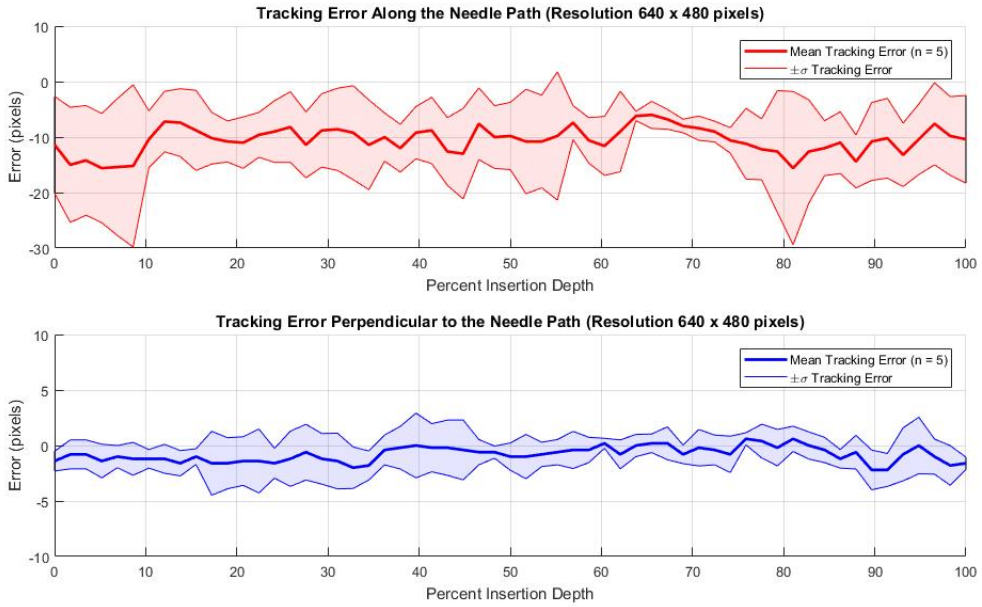

Figure 5.2: Error in 2D localization of the needle tip from optical flow measurements and manually-selected baseline tip coordinates. Top: the error along the path of needle insertion, bottom: shows error perpendicular to the path of needle insertion.

5.4 Active Compensation

5.4.1 Registering Localized Features

The robot controller continuously receives the localization transforms, T_{Tip}^{Image} and T_{Target}^{Image}, throughout insertion and pre-multiplies them by the $T_{Image}^{RobotPose}$ to determine

their position and orientation with respect to the current pose of the robot at each instance. Equations 5.2 and 5.3 below show the calculation of $T_{Tip}^{RobotPose}$, the current transformation of the tracked needle tip pose with respect to the current pose of the robot, and $T_{Target}^{RobotPose}$, the current transformation between the tracked target and current pose of the robot, using $T_{Image}^{RobotPose}$ found in Equation 5.1. Finally Equation 5.4 describes using $T_{Tip}^{RobotPose}$ and $T_{Target}^{RobotPose}$ to find T_{Target}^{Tip}, the transformation from tracked needle tip to tracked target with respect to the current robot pose.

$$T_{Tip}^{RobotPose} = T_{Image}^{RobotPose} T_{Tip}^{Image} \tag{5.2}$$

$$T_{Target}^{RobotPose} = T_{Image}^{RobotPose} T_{Target}^{Image} \tag{5.3}$$

$$T_{Target}^{Tip} = T_{Tip}^{RobotPose^{-1}} T_{Target}^{RobotPose} \tag{5.4}$$

5.4.2 Determining Direction of Compensatory Effort

Calculating T_{Target}^{Tip} at each instance provides the information needed to determine the desired direction of compensatory effort relative to a reference frame at the needle tip. With insertion defined along the Z-direction, the direction of rotational effort

in the plane normal to insertion can be found using the arctangent of the X and Y positions of T_{Target}^{Tip} as shown in Equation 5.5.

$$\theta_d = atan2(y(T_{Target}^{Tip}), x(T_{Target}^{Tip})) \tag{5.5}$$

5.4.3 Incorporating CURV Steering

In our case the imaging software is able to estimate needle tip orientation, therefore the rotational component of T_{Target}^{Tip} be used to employ a variable curvature needle compensation technique, where both direction and magnitude of desired effort can be implemented. A Gaussian based model employing Continuous Rotation and Variable (CURV) curvature [115] was used for all insertion trials; a variation of the duty-cycle approach [62] wherein the needle continuously rotates with an angle-dependent angular velocity. In this model for rotational bevel positioning, θ is the current rotational angle with θ_d the desired angle of bevel position for compensatory effort. Angular velocity ω at each rotational position is calculated using Equation 5.6 with the two parameters c and α corresponding to the Gaussian width and magnitude of compensatory effort respectively.

$$\omega(\theta, \theta_d) = 1 - \alpha e^{-\frac{(\theta-\theta_d)^2}{2c^2}} \tag{5.6}$$

A larger α generates a greater drop from the nominal rotational velocity, leading

to more deflection in the desired direction θ_d, while increasing c widens the total range of angular position where rotation occurs below the nominal velocity. Figure 5.3 illustrates the angular velocity profile for the CURV approach to active compensation. To note, the scope of this work is not comparing different approaches to steering of the needle trajectory; though the authors chose to employ the CURV approach, other bevel tip based curvature models such as the duty cycle [62] technique could be readily implemented instead. Additionally, Tsumura et al. [116] showed histological differences in tissue damage between needle insertion with continuous unidirection rotation vs bidirectional rotation, with bidirectional showing less damage. It was also not in the scope of this research to recreate that work, but it was noted and the CURV compensatory approach can be used in both uni- and bidirectional implementations.

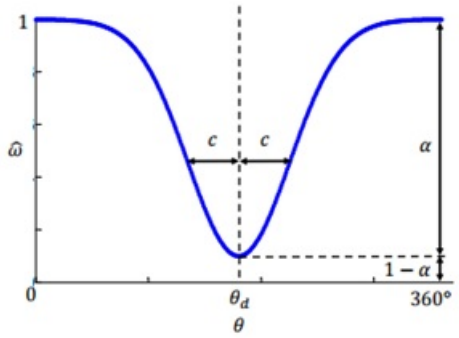

Figure 5.3: Angular velocity, ω , of the needle during Continuous Rotation and Variable (CURV) rotational compensation. This Gaussian based model is dependent on the current rotational position, θ, the desired direction of compensatory effort, θ_d, the desired Gaussian width c, and the magnitude of desired compensatory effort, α.

5.4.4 Determining CURV Parameters

In our case θ_d was calculated throughout insertion using Equation 5.5 and c was set to 10^o for all insertions. The magnitude of compensatory effort α was calculated throughout insertion by the two-dimensional difference between the target point and projection of the needle tip orientation onto the target plane, thus selecting the intermediate value between maximum curvature of a given needle in a given tissue and a straight line trajectory. Euler angles were extracted from the $T_{Tip}^{RobotPose}$ transform to determine the rotations of needle tip orientation about each of the X, Y, Z axes of the needle insertion coordinate frame, where insertion was performed along the Z-direction. The locations of the projected needle tip position on the target plane were found with Equations 5.7 and 5.8, using trigonometric relationships of the angles of rotation about the X and Y axes normal to the insertion direction, Rot(X) and Rot(Y) respectively.

$$X_{projected} = RemainingInsertionDepth tan^{-1}(Rot(Y) \tag{5.7}$$

$$Y_{projected} = RemainingInsertionDepth tan^{-1}(Rot(X)) \tag{5.8}$$

Furthermore, the X and Y values of the current needle tip position were used directly as projections of the current needle position on the target plane, and the in-plane magnitude of $Error_{projected}$ was calculated using Equation 5.9.

$$Error_{projected} = \sqrt{(X_{Error} + X_{Projected})^2 + (Y_{Error} + Y_{Projected})^2} \tag{5.9}$$

Finally, the instantaneous value of α was set using Equation 5.10, the ratio of $Error_{projected}$ to the maximum deflection attainable using our 18G needle, $Error_{max}$. For this experimental setup, $Error_{max}$ was experimentally determined to be $9.31mm_{rms}$ by performing ten needle insertions with no needle rotation to a depth of $125mm$, typical of all insertion trials performed. Figure 5.4 illustrates the components required to calculate $Error_{projected}$ inside the experimental setup.

$$\alpha = \frac{Error_{projected}}{Error_{max}} \tag{5.10}$$

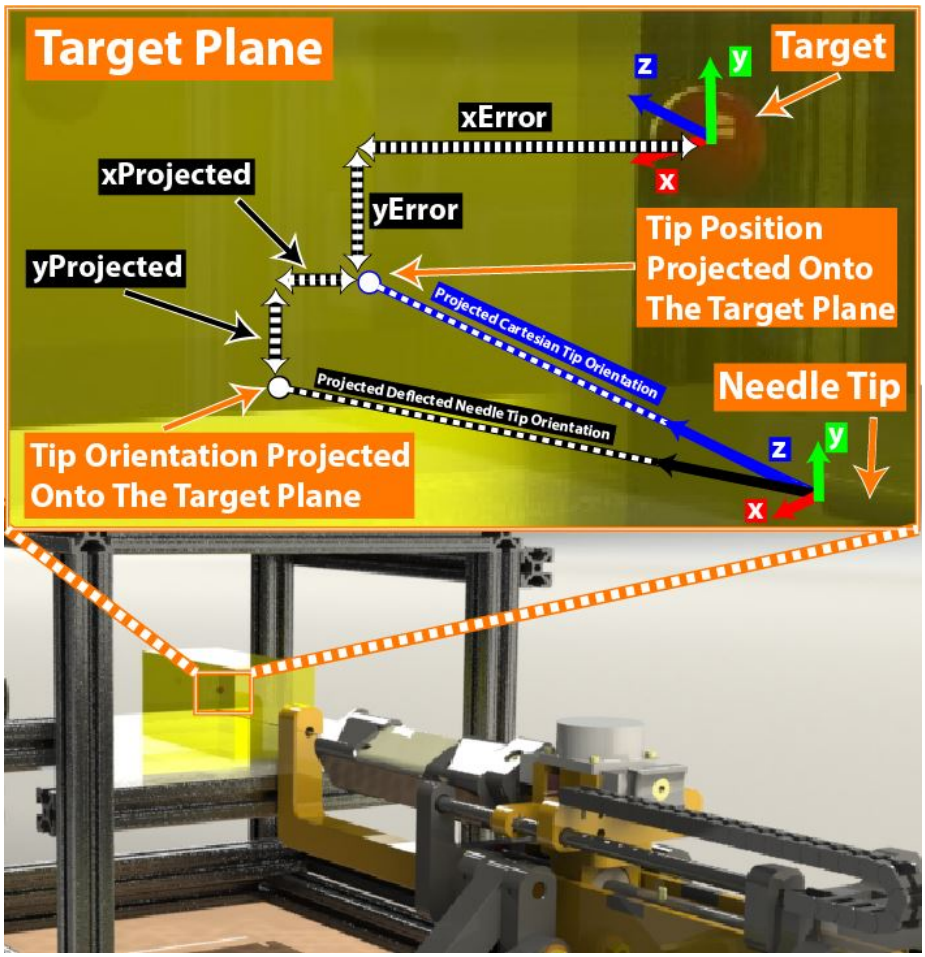

Figure 5.4: Dynamically determining the magnitude of desired steering compensation α using the needle tip position and orientation. The X and Y positions of the needle tip are projected along the Cartesian z-axis to the target plane as the current X_{Error} and Y_{Error} between tip and target. Additionally, the instantaneous needle tip orientation is extended to the target plane, where $X_{Projected}$ and $Y_{Projected}$ are found using the Euler angles determined from the rotation matrix of T^{Tip}_{Target} along with the remaining insertion depth. The magnitude of total instantaneous $Error_{projected}$ is determined by Equation 11, the two-dimensional Pythagorean theorem of $(X_{Error} + X_{Projected})$ and $(Y_{Error} + Y_{Projected})$

5.5 Validation Studies

5.5.1 Stationary Targets

Two targeting experiments were performed, the first on a static target and then on a shifted target mimicking tissue deformation and target deflection. In all insertion cases the needle was inserted until it reached the target depth based on visual confirmation of tip location using the needle tracking software. For the case of static targets, the robot was positioned to put the needle tip at the desired entry point aligned along a straight line trajectory toward the target location, and insertions were performed in three conditions: 1) autonomous insertion with no rotation to characterize $Error_{max}$, the needle deflection without active compensation, 2) autonomous insertion with image-guided active compensation, and 3) hands-on user directed cooperative insertion with image guided active compensation. The hypothesis was that targeting accuracy would improve with active compensation and that targeting accuracy would not be negatively affected when moving from an autonomous to cooperative insertion. In each trial a different target within the phantom was selected to avoid errors in a needle following a previous insertion track, and the result for all conditions was the position error between the needle tip and target at the target plane, orthogonal to the initial needle alignment axis.

Ten targeted insertions were performed with and without closed-loop image-guided active compensation and the average in-plane targeting error was found to be $9.30mm_{rms}$

and $3.79mm_{rms}$ for the no compensation and active compensation cases, respectively. Subsequently, five participants (3 males, 2 females, aged 23-53, all right handed, all novice to the task) each performed ten cooperatively controlled needle insertions with active compensation and Table 5.1 describes the in-plane targeting accuracy for each participant. Figure 5.5 illustrates the comparison of targeting accuracy between the autonomous no rotation, autonomous with active compensation, and all hands-on cooperative cases with active compensation.

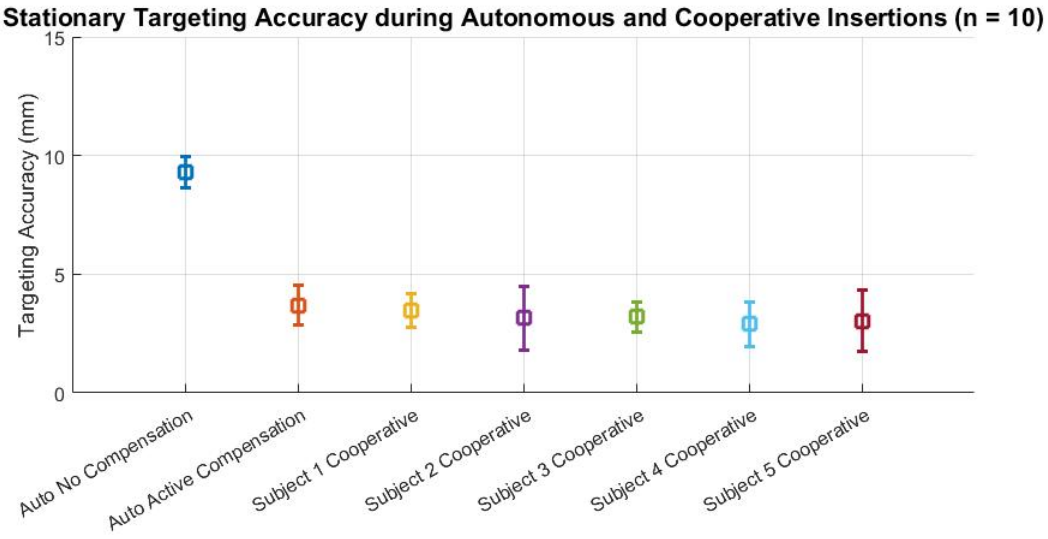

Figure 5.5: Comparison of targeting accuracy (n=10) between autonomous insertions with no rotational of bevel tip positioning, autonomous insertions with closed-loop image-guided active compensation through rotational bevel tip positioning, and 5 subjects performing hands-on cooperatively controlled needle insertions with active compensation.

Table 5.1: Stationary targeting accuracy for insertions under cooperative control

Subjects	Mean (mm)	St. Dev. (mm)
1	3.50	0.71
2	3.15	1.36
3	3.20	0.62
4	2.90	0.95
5	3.04	1.28

For each of the insertion sets with active compensation, paired t-tests were performed to compare the data. Paired t-tests were performed and Table 5.2 illustrates there was no statistically significant difference ($p > 0.05$) between the targeting accuracy during autonomous insertion with any of the user directed cooperative cases, in addition to no statistical significance between the targeting accuracy seen between each pair of users. Across all insertions the average target depth was $125.23mm_{rms}$ and the average targeting accuracy with active compensation was found to be $3.56mm_{rms}$.

Table 5.2: Statistical outcomes from paired t-tests on stationary targeting accuracy across insertion conditions

	Autonomous	Subject 4	Subject 3	Subject 2	Subject 1
Subject 1	0.253	0.085	0.247	0.298	0.514
Subject 2	0.383	0.098	0.383	0.443	
Subject 3	0.803	0.698	0.880		
Subject 4	0.549	0.448			
Subject 5	0.802				

5.5.2 Shifted Targets

The second targeting experiment evaluated the response of the system to target shift during cooperative insertions. As the error seen in the non-compensatory case of the first experiment was $9.30mm_{rms}$, it was expected the system could compensate with comparable targeting accuracy to target shifts below this value. Twenty targeted cooperative insertions were performed in a similar manner to the first experiment, with a target shift introduced once the needle made contact with the phantom. The shift was introduced virtually in the target plane perpendicular to the insertion axis, with both direction and magnitude assigned randomly using polar coordinates. The direction of shift was open to all 360^o and magnitude was randomly assigned be-

tween $1 - 10mm$. Results from the first experiment showed there was no statistically significant degradation from the autonomous to the user's case, and no significant variation between each user. Thus, each individual subject was not brought back to perform the second experiment because the first experiment showed the accuracy is not dependent on the user. Figure 5.6 shows the targeting accuracy for each insertion with respect to the amount of target shift, sorted by magnitude of the randomly assigned shift.

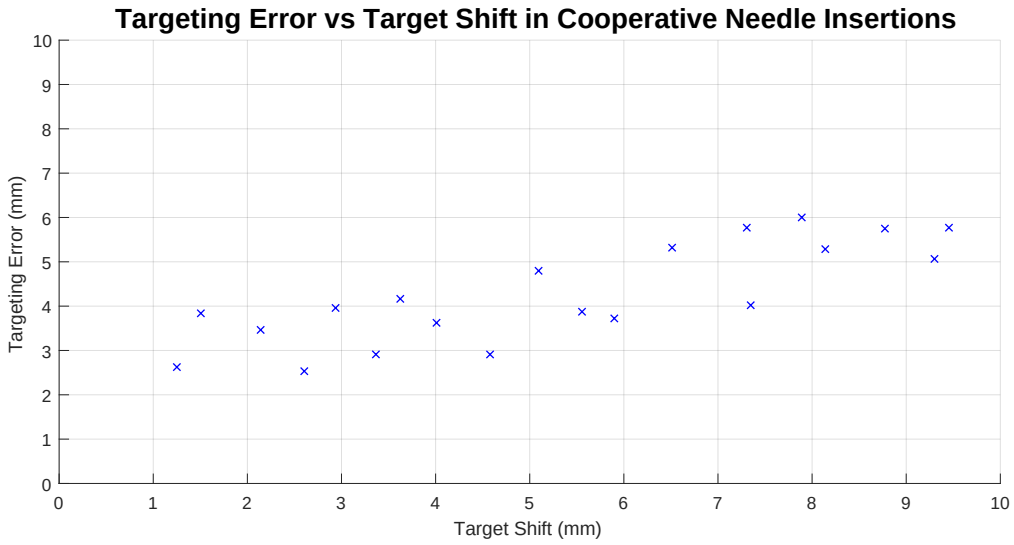

Figure 5.6: Targeting accuracy vs. in-plane target shift magnitude for twenty cooperatively controlled needle insertions with a randomized shift introduced upon needle contact with the phantom. The direction and magnitude of target shift was randomly generated in polar coordinates to be on the target plane perpendicular to the needle insertion axis at a magnitude between $1 - 10mm$.

5.6 Discussion and Conclusions

In this work we presented an imaging-agnostic method to provide closed-loop active compensation for unmodeled needle deflection and target shift during cooperatively controlled needle insertions. Two experiments were performed and the results of the first experiment appear to suppose the following considerations:

- closed-loop active compensation through autonomous rotational bevel tip positioning can improve the targeting accuracy when compared to open-loop manual needle insertion
- targeting accuracy when using closed-loop autonomous rotational bevel positioning does not degrade when moving from an autonomous insertion to a user directed cooperative insertion
- targeting accuracy during insertion under cooperative control is robust to different individuals performing the insertions

Additionally, the results from the second experiment suggest targeting accuracy comparable to the stationary case can be achieved for target shifts approximately up to $5mm$, which in a clinical scenario can still lead to more biopsies collected during the first insertion, shortening procedure time and limiting patient discomfort.

The controller is structured to determine compensation parameters from streamed homogeneous frame transformations representing needle tip and target received via

OpenIGTLink from any capable imaging source. The robot autonomously updates rotational bevel position based on these inputs to direct the needle tip towards the target. As opposed to an open-loop insertion, active compensation is robust to registration error, distortion of images, and swelling or target shift. Here we performed tests in the lab setting using perpendicular cameras to act as a proxy for multiplanar MR imaging, as we have previously shown needle localization in MRI [94]. This system was developed to be used in the lab and is adoptable by other researchers, only requiring two low cost USB cameras to implement with the tracking algorithm available open source on github (https://github.com/WPI-AIM/NeedleTracker).

As was shown in the experiment, active compensation improved accuracy. This experiment was intended to demonstrate that the improvement in accuracy can be maintained even when the physician is still directly in the loop, thus also enhancing the safety of the procedure. In a separate experiment, a case with no compensation was performed under autonomous insertion to illustrate that active compensation does in fact increase overall targeting accuracy, but each participant did not perform the task without active compensation. Figure 5.5 shows the targeting error is greatly reduced when using closed-loop active compensation as compared to a non-compensatory no rotation insertion case. The average targeting error was found to be $3.56mm_{rms}$ in all cases with active compensation, considerably less than the average $6.6 \pm 5.1mm$ error found via open-loop manual needle insertions during clinical trials using the robot base for target alignment [36]. Furthermore, there was no statisti-

cally significant difference in the targeting accuracy between autonomous and user directed cooperative insertions. The remaining error can likely be attributed to the initial bevel tip position when entering the phantom, and any plastic deformation of the needle that may have occurred throughout repeated insertion trials.

Regarding cooperative insertions toward shifted targets, the results indicate that the system does compensate for target shift, with accuracy degrading as shift increases towards $Error_{max}$. This outcome is understandable for a system using a relatively stiff needle typical of clinical biopsy where aggressive needle poses and s-curve conformations as seen in research of thin flexible needles are not possible. In this case, if a deflection has begun in one direction it is much harder to overcome the initial curvature already present in an undesired direction. This becomes important due to the randomized location of the target shift in the experiment. If the needle entered the phantom with the bevel tip facing a certain way and began deflecting, a random shift to a location opposite the initial trajectory line, to a distance and angle unlikely to occur anatomically, would cause the final targeting accuracy to degrade and not be reflective of what could be possible with this system clinically.

Chapter 6

Development of a Clinical Workflow for Robotic Needle Placement Under Cooperative Control

6.1 Introduction

This chapter introduces the system integration and validation in the clinical environment. Continuing the path of clinical translation for the cooperative system, the intent was to maintain the same procedural work flow the physicians and nurses are accustomed to in clinical trials. In order to accomplish this goal, the systems

developed in the lab needed to be integrated into the clinical workflow and tested. The procedure carried out during final system validation remains almost identical to the MRI-guided targeted biopsy described in [117]. The preliminary steps to prepare for needle insertion were:

1) Robot preparation outside of the scanner bore (hardware testing, homing and sterile draping)

2) Placement of the robot into the slots on the patient board and locked into place

3) Phantom placement in the typical targeting region of the robot

4) Imaging of the fiducial Z-Frame

5) Registration of the robot into the scanner coordinate frame

Once the robot was prepared for functional testing the following six major steps of biopsy collection illustrated in 6.1 are:

1) Image acquisition of the desired targeting volume

2) Segmentation and target selection using surgical planning software 3DSlicer

3) Trajectory generation from insertion point to target

4) Robot controller validation of robot motion

5) Robot base positioning for the 2D insertion plane

6) Pressing the foot pedal safety switch and performing the hands on robotic needle insertion

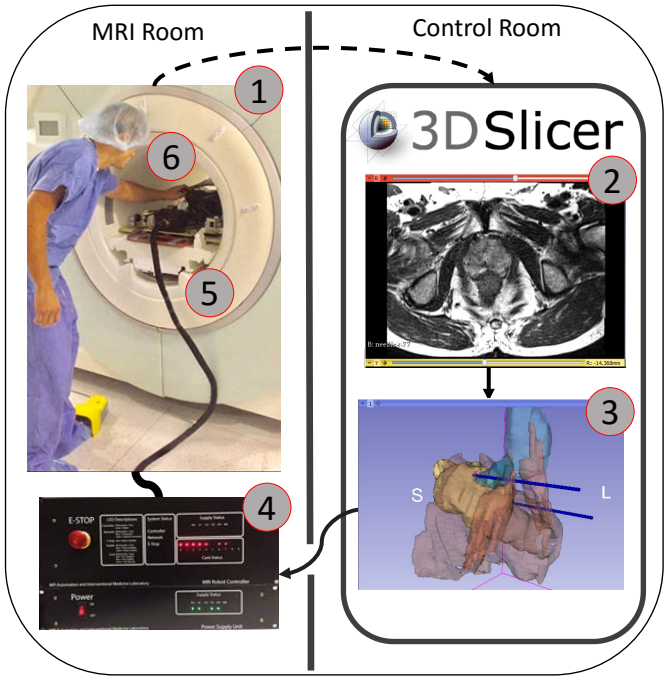

Figure 6.1: The major steps involved in performing an in-bore cooperatively controlled needle insertion. 1) Localization imaging of the target volume, 2) Target selection using surgical planning software 3DSlicer, 3) Trajectory generation from insertion point to target, 4) Controller validation of robot motion, 5) Robot base positioning for the 2D insertion plane, and 6) Performing the hands on robotic needle insertion.

In order to maintain the clinical workflow, both the hardware and software developed as subsystems in the laboratory needed to be integrated together and with the standard protocols in the operating room. Clinical integration, the effect of the

system on the SNR of MR images, and validation experiments were performed in the Advanced Multi-Modality Image Guided Operating (AMIGO) Suite at Brigham and Women's Hospital.

6.2 Hardware Integration

Hardware integration into the clinical environment involves placement of the manipulator inside the scanner bore. The robotic manipulator is placed inside the scanner bore on a patient board mounted to the MRI table. The patient board has slots for the robot to slide into and lock in place, as well as leg supports to maintain the patient position throughout the procedure. Figure 6.2 shows an exploded view of the robot, patient board and scanner.

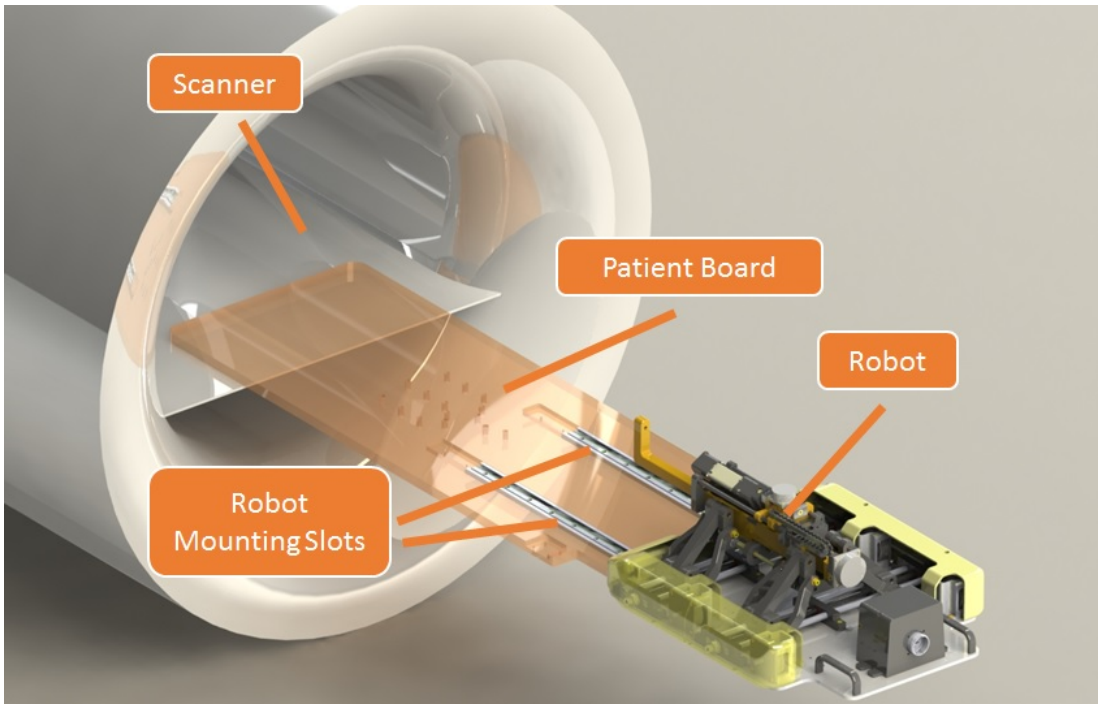

Figure 6.2: Integration of the robot, patient board and MR scanner. The robot slides into slots on the patient board and is locked in place with thumb screws. The patient board is rigidly mounted to the scanner bed.

The robot is connected to the controller via the shielded cable described earlier in this dissertation, as the control box sits against the wall outside the 5 Gauss line. The foot pedal safety switch is connected the the controller via a fiber optic cable and is placed at the entrance the to bore. An imaging coil covers the typical targeting region for prostate interventions, and this location is registered to the isocenter of the scanner. The robotic hardware was integrated in the MRI room and ready for targeted needle insertion as shown in Fig. 6.3.

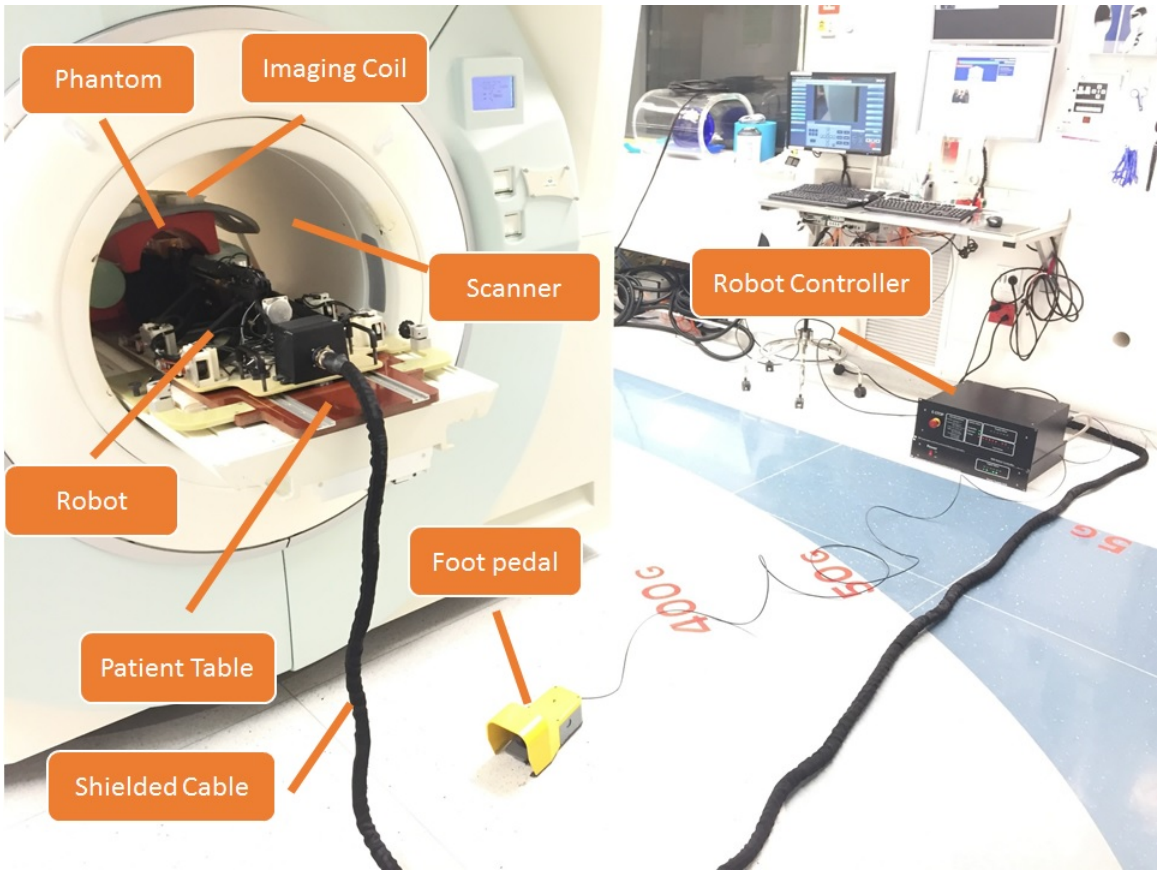

Figure 6.3: Hardware integration of the robot system into the clinical environment. The robot sits on the patient board inside the MR scanner. The phantom is placed in the typical targeting region of the robot and covered with the body imaging coil, typically used in prostate interventions. The robot is connect to the controller via a shielded cable and the foot pedal switch must be pressed for the motors to be enabled.

Outside the scanner room the control console can be seen in Fig. 6.4. The scanner console pushes MR images to the workstation running 3DSlicer and the robot control GUI interface. This machine interfaces with the controller via fiber optic

communication through the scanner room wave guide.

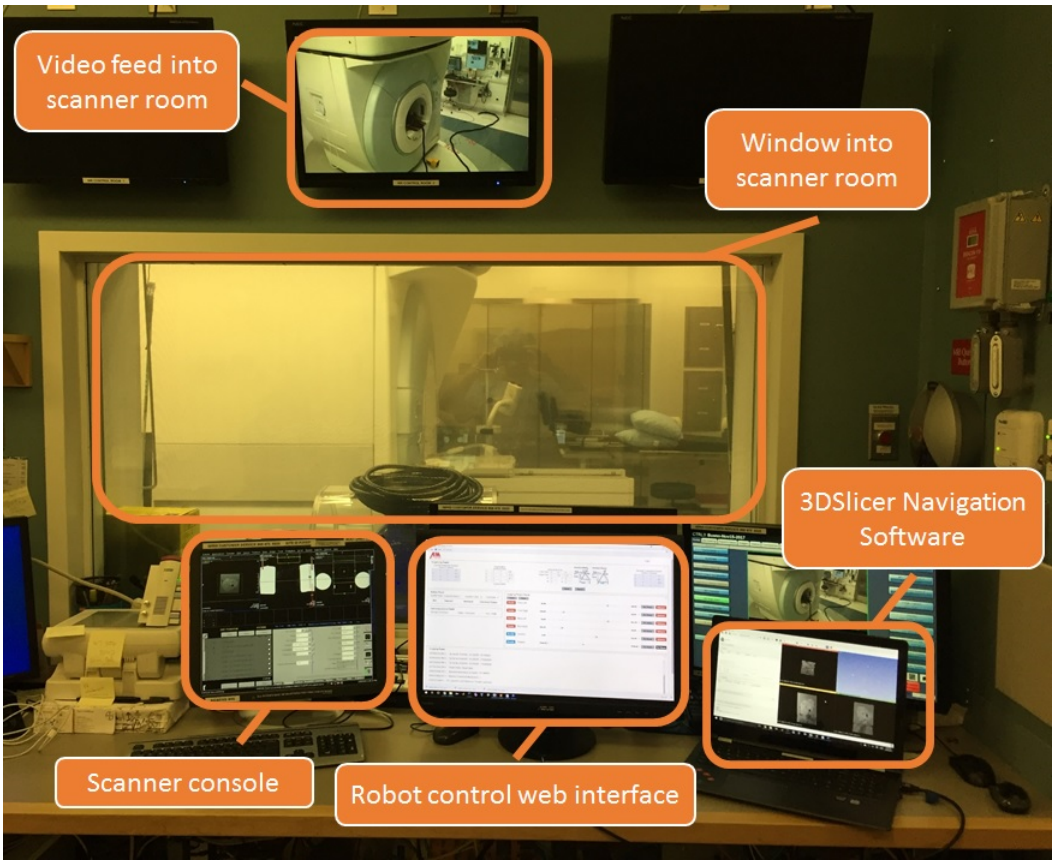

Figure 6.4: The scanner console and control station. The robot control web interface and 3DSlicer navigation software run on a workstation alongside the scanner console, which pushes DICOM images to 3D slicer for surgical planning. A shielded window provides a view into the scanner room and cameras inside the room provides obstructed views to the console.

6.3 Software Integration

Cooperative insertion, membrane detection and active compensation were are all developed as individual subsystems. Once sufficiently tested they needed to be integrated into a single system capable of providing all desired functionality to a cooperative biopsy procedure. Furthermore, integration of robot homing, registration and manual jogging in both joint and task space was required.

This was accomplished using a web-based graphical user interface (GUI), where a local web server runs on the robot controller and the front-end web GUI is open on the control console. The web GUI displays all robot specific information including current and desired task space positions, the registration transform, joint level encoder position and force sensor values. Figure 6.5 shows an annotated image of the GUI highlighting where all information is presented.

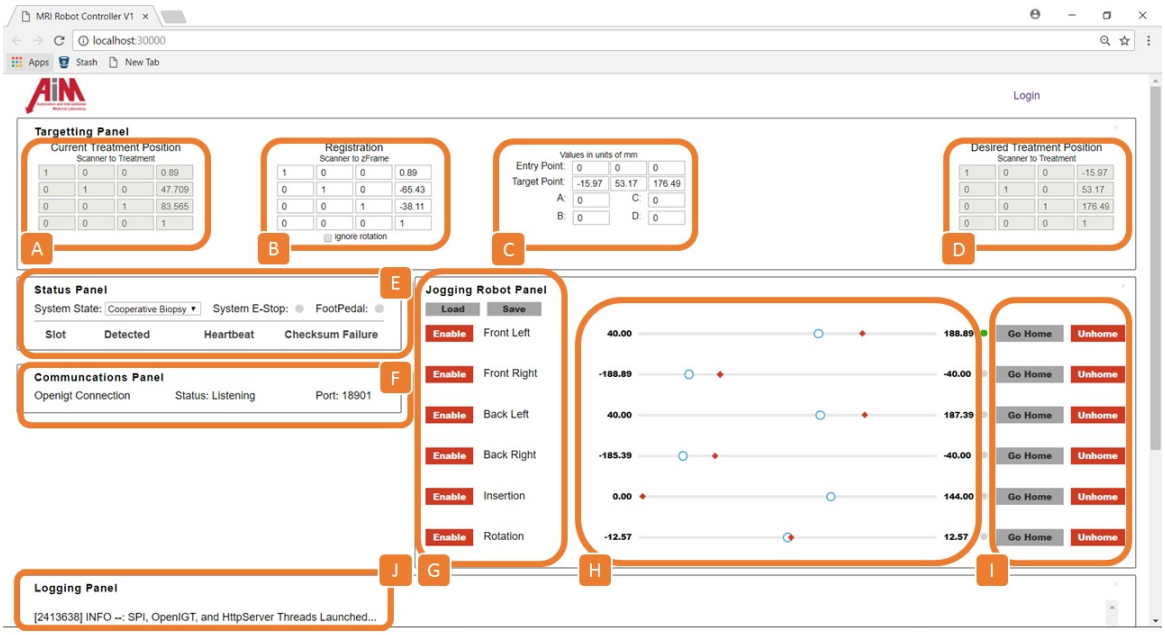

Figure 6.5: The web GUI used for control of the robotic system. The components of the GUI are: A) the current treatment position, in this case the current needle tip position, B) the registration transform used to map the robot kinematics into the scanner coordinate frame, C) user defined entry and target points for task space robot control, D) the desired treatment position, the target location and orientation, E) the robot status panel, where the drop down menu controls robotic system state for different functionality, F) the communications panel, showing the status of open network connections, G) individual axis enable and disable buttons, H) joint positions for each axis (red), target positions for each axis (blue), I) buttons to send each joint to its home position or set the current position as home, J) logging panel to display sensor values and status reports.

The system state selection menu inside the Status Panel (E) is where the robot modes are changed, and the following options are available:

- **Manual Control**

  This state allows for manual jogging of each robot axes in joint space, or complete task space movements based on user defined targets. All sensor data is continuously updated in this state. Furthermore, the Current Treatment Position, Registration and Desired Treatment Position transforms are also continuously updated and this state is used during the registration procedure.

- **Homing**

  The homing procedure localizes the robot position through a series of motions to touch off limit switches for the insertion and each of the base axes. With continuous rotation, this axis is homed manually to set the bevel tip to the rotational location corresponding to the zero position. The procedure starts with homing insertion to ensure the needle is fully retracted before moving the base. Once insertion reaches its retraction limit the axis is stopped and the encoder value set to zero. Due to the robot kinematics and the available travel distance for each joint, a step-wise homing procedure was implemented. To home the robot base: 1) all four joints move to the left and the FrontLeft and BackLeft joints touch off on their respective limit switches at the outside range of their travel. If one touches off before the other the joint stays at the limit switch until the other reaches, 2) once both have touched off the entire robot

moves to the right, and the same procedure occurs on for the FrontRight and BackRight joints on the outside of their travel, 3) once both of the right side joints have touched off the robot base is fully localized and each joint moves to its home position to center the robot between outside limits. Figure 6.6 illustrates the homing procedure for the 4-DoF base.

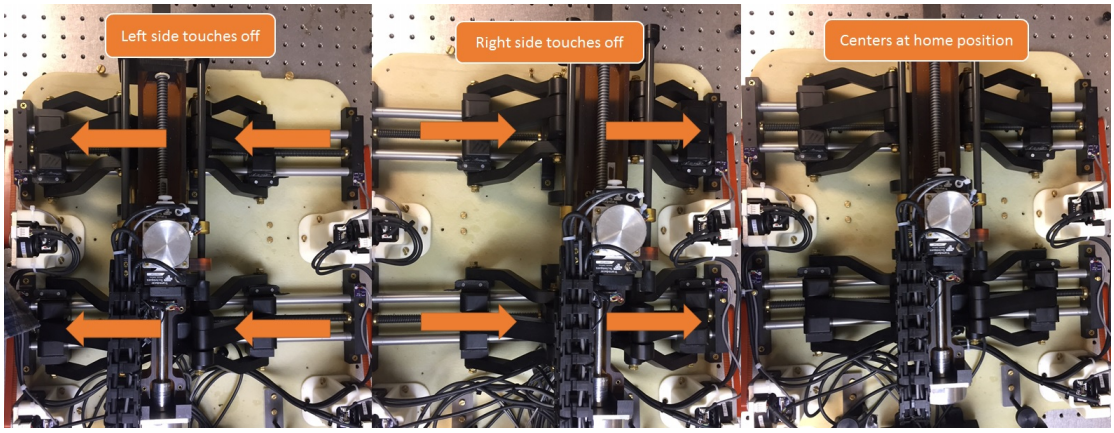

Figure 6.6: Illustration of the robot homing procedure. Due to the available travel of the robot, homing the base must take place in three steps. Left: The robot moves to the left and touches off the FrontLeft and BackLeft joints on limit switches at the outside of their travel. Center: The robot moves to the right and touches off the FrontRight and BackRight joints on the outside of their travel, Right: The robot is fully localized and moves to the home position.

- **Cooperative Biopsy**

  The Cooperative Biopsy state is where each developed subsystem is integrated into a functional procedure for prostate biopsy. This system state is dependent

on communication via an imaging source to provide a target depth, localized needle tip positions as well as any predefined membranes to detect. The robot must be homed, registered and have a valid socket connection to the imaging source for the procedure to continue. If each of these conditions is satisfied the controller receives the nominal depth of any membranes defined by a user to detect, as well as a continuous stream of localized needle tip and target positions. At this point the user presses the foot pedal to align the base and then performs the cooperative needle insertion. Active compensation autonomously rotates the needle using the CURV approach, and if puncture of a desired membrane is detected the predefined response to this detection is performed. Once the needle reaches the target depth as defined in imaging, the insertion is stopped and a biopsy core can be taken.

Integration of individual subsystems was performed in the Web GUI, but full integration within a clinical scenario was required in order to run final system validation. The full integration of the robotic system into the clinical environment for targeted MRI-guided biopsy is illustrated in Fig. 6.7. The MR images were pushed from the scanner console to the workstation in the Digital Imaging and Communication in Medicine (DICOM) format, the international standard for transmitting and storing medical images.

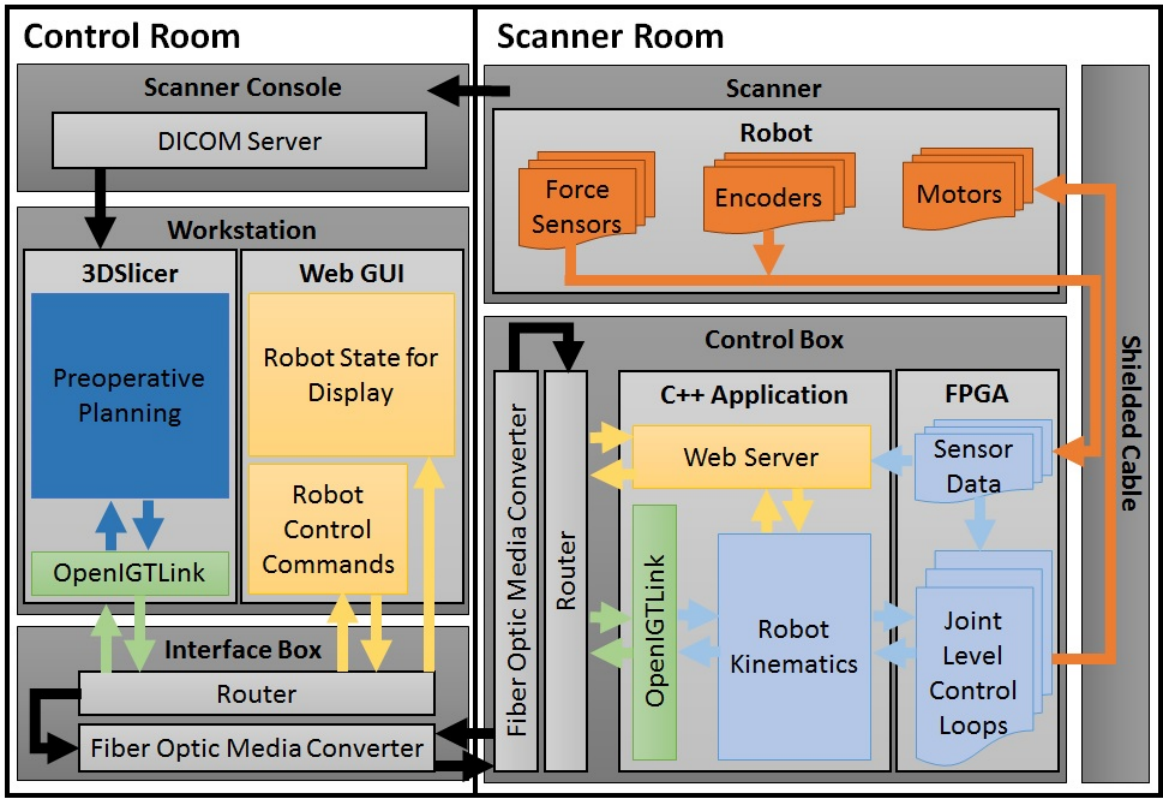

Figure 6.7: Software integration of the system into the clinical environment. In the control room the scanner console pushes DICOM images to the workstation running 3DSlicer navigation software and the web GUI for robot control. The web GUI both displays the robot state and allows for direct control of the robot in both joint and task space. The control box is located inside the scanner room and communicates to the workstation via a fiber optic cable through the scanner room wave guide. Surgical planning information is passed via OpenIGTLink while the web GUI interface communicates to a web server running on the control box. The robot is inside the scanner bore and the MR images arrive at the scanner console to be pushed to the workstation.

6.4 SNR Evaluation

Mechatronic systems within the MRI can cause significant image degradation. Poor image quality may result in incorrect localization of needle tip and target as well as planning locations for puncture detection. Each subsystem was specifically selected for use in the MR environment and the effect of the total robot and controller system on the SNR of MR images was evaluated. To test the SNR, a gelatin phantom developed under an American Association of Physicists in Medicine (AAPM) guidance was used, similar to that in [118] and [106]. The phantom measures $90mm \times 90mm \times 60mm$ and was mixed 15:1 water to gelatin by weight and can be seen in Fig. 6.8.

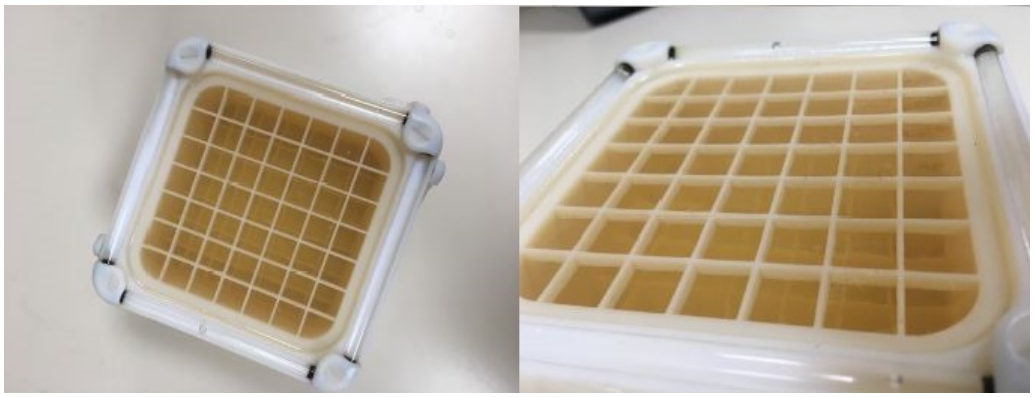

Figure 6.8: The phantom used for SNR testing was filled with 15:1 water to gelatin by weight and is based on a standard by the American Association of Physicists in Medicine.

SNR evaluation was performed at Brigham and Women's Hospital and the phantom was placed in the typical targeting region of the robot and not moved between conditions. To capture the MRI images, radiofrequency (RF) imaging coils are used

as receivers and placed as close to the desired imaging volume as possible. The Spine Matrix and Body Matrix coils traditionally used for imaging in prostate biopsy were used and the testing setup is shown in Fig. 6.9. Tests were conducted in four different conditions:

- **Baseline:** The robot and its controllers are not present in the MRI room
- **Robot Present:** the robot is present inside the MRI bore and is connected to the controller but the power remains off
- **Robot Powered:** The robot is present inside the MRI bore and is connected to the controller, the controller is powered on but the motors are not moving
- **Robot Moving:** the robot is present inside the MRI bore and is connected to the controller, the power is on and the motors are moving.

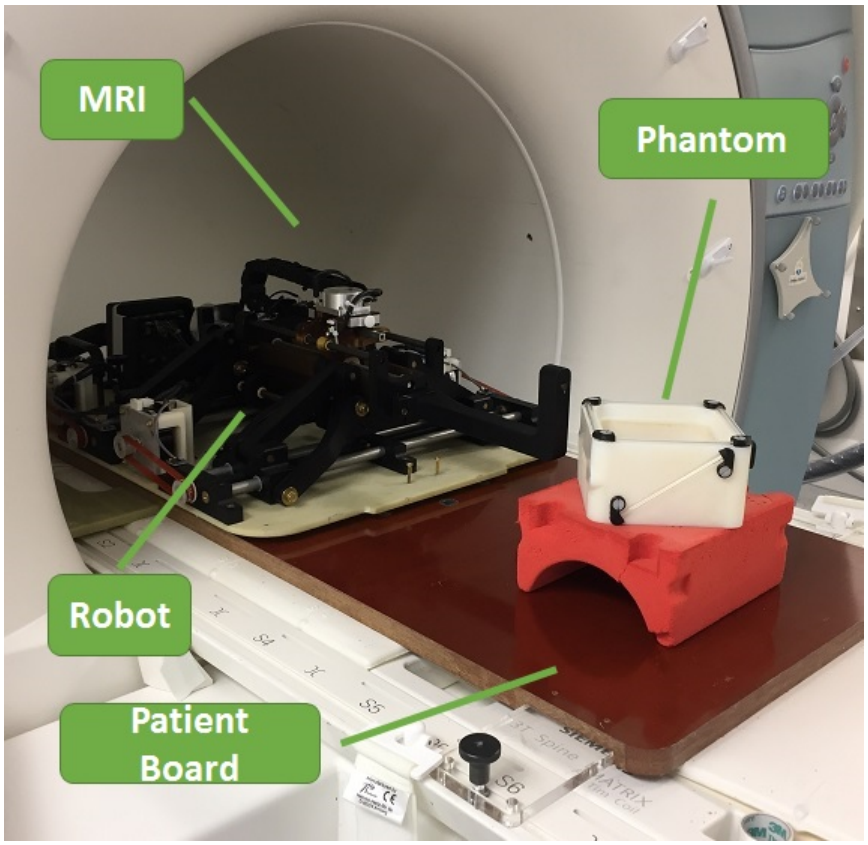

Figure 6.9: The robot and phantom in position during SNR testing. The phantom is placed in the typical targeting region for prostate biopsy.

SNR was evaluated using standard imaging protocols, T1-weighted spin echo and T2-weighted dual spin echo sequences from the American College of Radiology (ACR) for quality control tests. These sequences differ by the repetition and echo times of pulses, where T1 is the longitudinal relaxation time, which determines the rate at which excited protons return to equilibrium, and T2 is the transverse relaxation time, which determines the rate at which excited protons reach equilibrium or go out of phase with each other [119].

Table 6.1 shows the parameters for both image sequences and Fig. **??** shows representative slices of the images used to calculate SNR in each condition. Signal intensity was calculated using Equation 6.1, signal noise with Equation 6.2, with SNR calculated as shown in Equation 6.3, based on the National Electronics Manufacturing Association (NEMA) standard in [120], and similarly to [43, 106, 118]. Paired t-tests were used to determine statistical significance of any signal changes seen across conditions.

Table 6.1: MRI parameters for the image sequences used to test SNR

Sequence	**ACRT1**	**ACRT2**
Repetition Time (ms)	500	2000
Echo Time (ms)	20	20/80
Field of View (mm)	$250x250$	$250x250$
Matrix	$256x256$	$256x256$
Number of Slices	11	11
Slice Thickness (mm)	5	5
Flip Angle (degrees)	90	90
Receiver Bandwidth (kHz)	16.6	16.6

$$S_s = \frac{\underset{u,v:ROI}{mean}\left(p^{Is}_{u,v}\right) + \underset{u,v:ROI}{mean}\left(p^{Js}_{u,v}\right)}{2} \tag{6.1}$$

$$N_s = \frac{\underset{u,v:ROI}{std}\left(p^{Is}_{u,v} - p^{Js}_{u,v}\right)}{\sqrt{2}} \tag{6.2}$$

$$SNR_s = \frac{S_s}{N_s} \tag{6.3}$$

Plots of the SNR results for the T1 and T2(80ms echo) are shown in Fig. 6.10 In the T1-weighted scans there was no statistical significance between baseline images ($p = 0.518$), followed by a statistically significant drop of approximately 10% of signal in the Robot Present case ($p = 0.006$). For the remaining conditions there was no statistical significance of signal loss between the Robot Present-Robot On, Robot Present-Robot Moving, and Robot On-Robot Moving cases ($p = 0.355, p = 0.174, p = 0.242$, respectively).

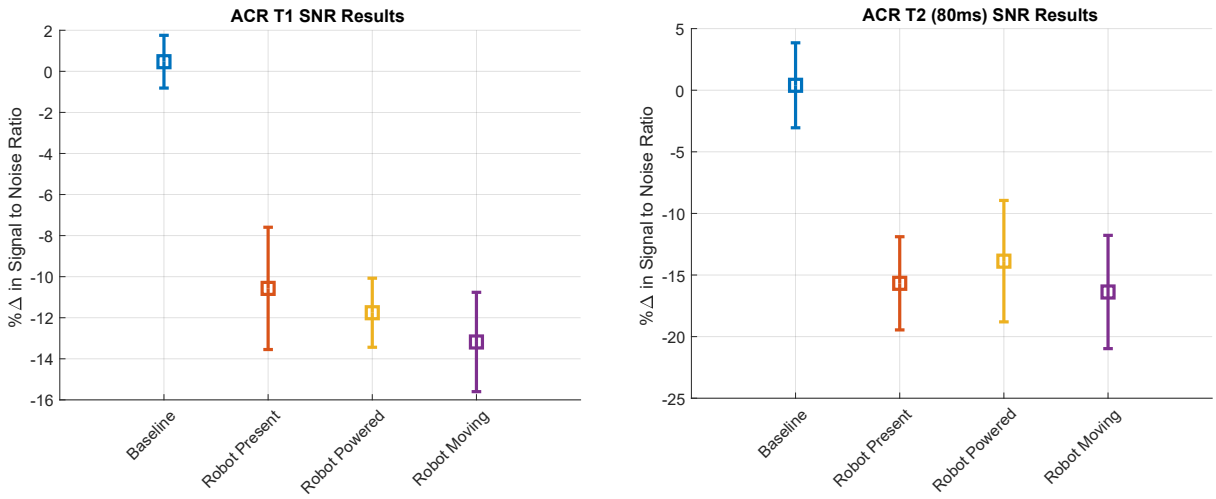

Figure 6.10: The results of the SNR analysis. There was a statistically significant drop in image signal from the baseline to the robot present case, with no statistically significant difference seen between the robot present case and either of the robot on or robot moving cases.

In the T2-weighted scans there was also no statistical significance between baseline images ($p = 0.872, p = 0.832$), for the 20ms echo and 80ms echo, respectively. Similarly to T1, for each echo time there was an approximate 15% drop in signal for the Robot Present case with statistical significance, ($p = 0.003$) for 20ms, ($p = 0.004$) for 80ms, followed by no statistical significance between the three cases thereafter ($p = 0.540, p = 0.426, p = 0.457$) for the 20ms echo, and ($p = 0.182, p = 0.725, p = 0.375$) for the 80ms echo. These results show that the presence of the robot in the MR bore degrades the image SNR between 10% and

15%, but there is no further statistically significant loss by powering on the robot or moving the motors during a scan sequence.

6.5 Final System Validation

6.5.1 Experimental Method

The experimental method used to validate the system is presented below. The workflow, initially presented in Chapter 1, is shown again in Figure 6.11 as the basis for validating the system in a clinical scenario. Each of the three major sections shown in the figure: Single Occurrence, Performed Once Per Target and Continuous Image Acquisition are detailed in the sections below.

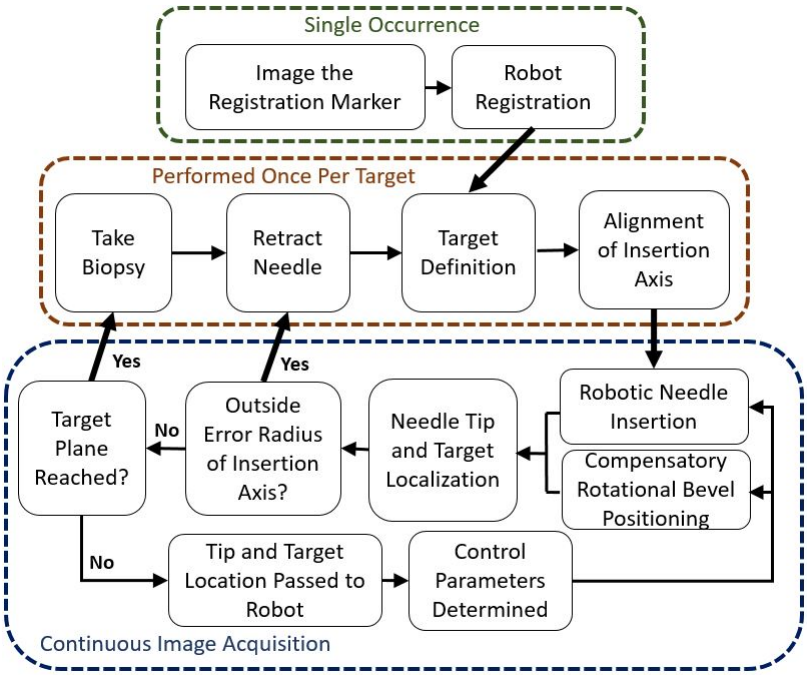

Figure 6.11: The system workflow for collecting an image-guided targeted biopsy using cooperatively controlled needle insertion with active compensation for unmodeled needle deflection and target shift.

6.5.1.1 Heterogeneous Phantoms for System Validation

Heterogeneous phantoms based on the characterization from Chapter 4 were used for all in-bore validation trials. Separate phantoms were used in the two experiments performed and Fig. 6.12 shows an image of each. On the left is a layered phantom used for validation of membrane puncture detection under real-time imaging. Two and three layered phantoms were used, consisting of PVC layers of the stiff 70%/30% and soft 60%/40% concentrations with a polyimide layer placed between each. On the right is the phantom used in targeting experiments, three anatomical structures

were molded using the 70%/30% concentration of PVC and softener: the prostate, the corpus spongiosum and the bulbospongiosus. The softer 60%/40% concentration used to suspend these structures in an anatomical position. Additionally, plastic beads were molded into the prostate to target and a layer of polyimide were molded at the face of the prostate act a membrane capsule at that depth.

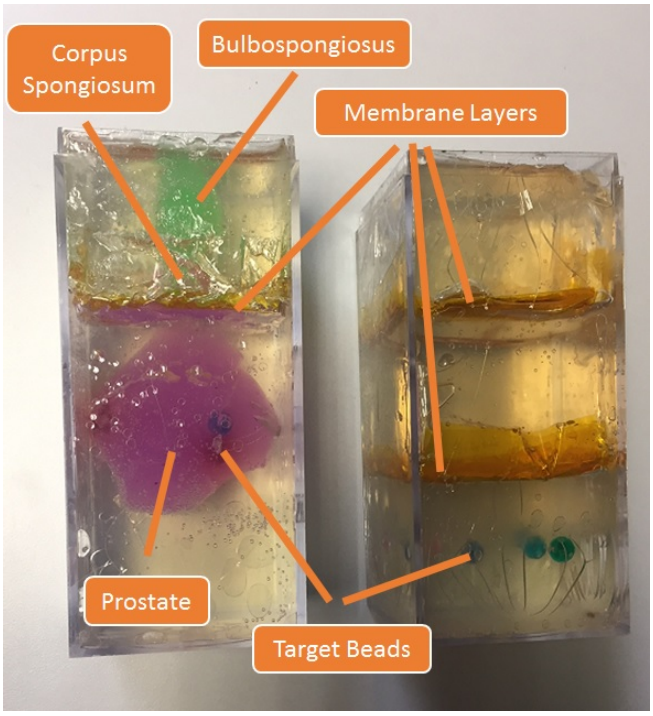

Figure 6.12: The phantoms used in experimental in-bore system validation. Left: layered phantom for membrane puncture detection validation, Right: molds of the prostate, corpus spongiosum and bulbospongiosus were assembled into their anatomical positions for targeting, with plastic beads in the prostate as targets and a layer of polyimide at the face of the prostate to act as a capsule layer.

6.5.1.2 Anatomical Description for Surgical Navigation

There are three cross sections used in anatomical description, the coronal, sagittal and transverse planes. These planes correspond to anatomical coordinate axes where the coronal plane is perpendicular to the anterior-posterior axis, the sagittal plane is perpendicular to the left-right axis and the transverse plane is perpendicular to the inferior-superior axis. Figure 6.13 shows the three anatomical planes dividing the body shown in the anatomical position, described as upright with upper limbs at the body's sides and palms facing forward. These planes are used in medical imaging and surgical navigation, where the right-handed coordinate systems Left-Posterior-Superior (LPS) and Right-Anterior-Superior (RAS) are used to define locations within the body. All calculations performed in these experiments using 3DSlicer navigation software were done using the RAS coordinate system.

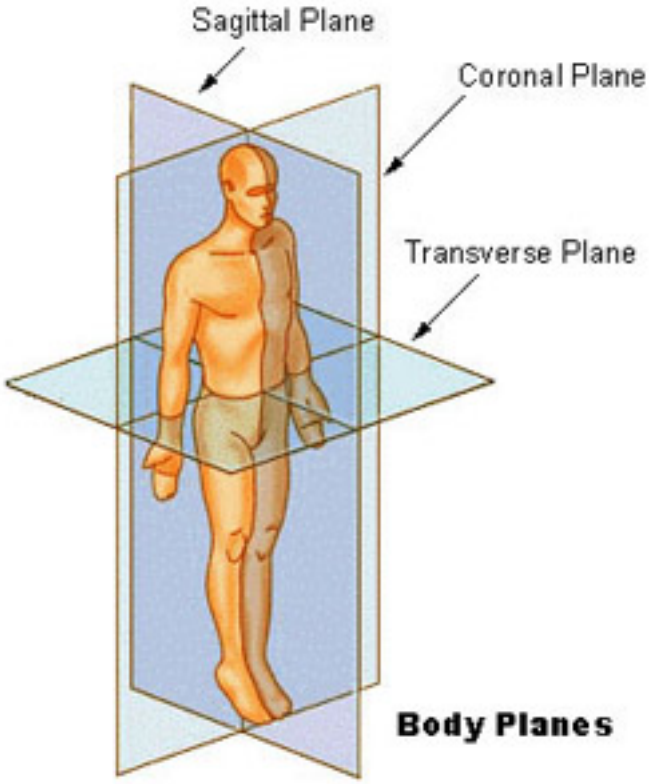

Figure 6.13: The anatomical planes used in surgical navigation. ©National Cancer Institute

6.5.1.3 MR Images for Feedback Guidance

The MR images taken throughout the experiment were pushed from the scanner console to the workstation in the DICOM format and viewed in 3DSlicer. Two imaging sequences used in the experiments were a T2 weighted Turbo Spin Echo (TSE) for needle localization and the BEATT RT real-time sequence used during membrane puncture detection. Table 6.2 details the parameters for each imaging sequence.

Table 6.2: MRI parameters for image sequences used during system validation

Sequence	**T2 TSE**	**BEAT IRTTT**
Repetition Time (ms)	3200	433.5
Echo Time (ms)	96	1.6
Field of View (mm)	$160x160$	$293x293$
Matrix	$256x256$	$128x128$
Number of Slices	28	1
Slice Thickness (mm)	3	5

6.5.1.4 Sterilization and Draping

The sterilization and draping techniques used in the clinical trials of robot-assisted biopsy were largely maintained. Similar to those trials, the needle guided was removable and was to be sterilized by autoclave prior to the procedure. The rest of the robot can be covered in a sterile plastic drape and the needle guide fastened to the robot through the drape. An additional consideration in this case as opposed to the manual needle insertion case was the attachment of the needle to the needle driver. The two needle coupling components must be sterilized by autoclave as well and fastened to the robot on top of the drape as shown in Fig. 6.14.

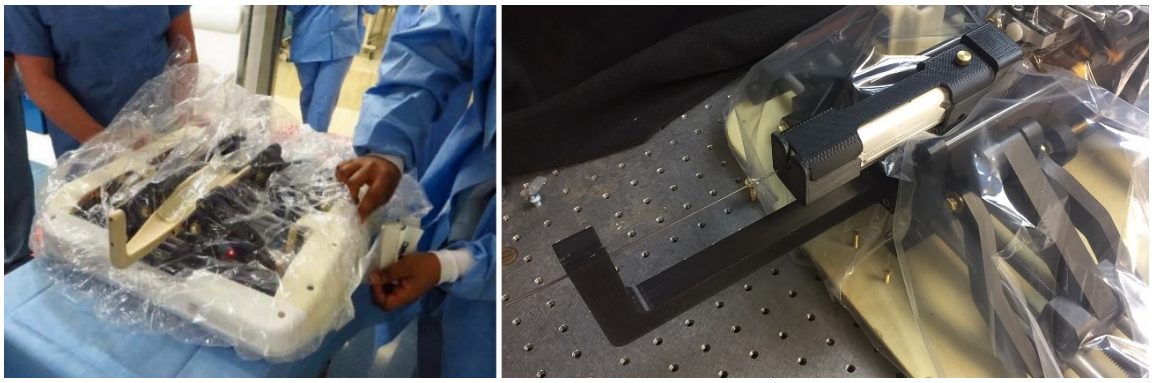

Figure 6.14: Left) the robot base draped during clinical trials, Right) the robot and needle driver covered by a sterile drape. Only sterilization of the needle coupling components is changed from the clinical procedure.

6.5.1.5 Registration

A fiducial Z-Frame was used to register the robot to the scanner coordinate system. First introduced as a single-image registration method by [121] for use with CT, this techniques used fiducial tubes configured into three perpendicular Z shapes. By filling these tubes with an MR visible contrasting agent, use of the Z-Frame can be extended into MRI interventions such as in [122] as well as in the clinical trials of robot-assisted biopsy in [36] on which this work was built.

The Z-Frame used in this system consists of nine MR visible fiducial markers arranged in perpendicular "Z" configurations within a 3D printed mount. With a set of image slices showing all nine fiducial markers a detection algorithm locates the

centroid of each fiducial point within the slices. Once each of these is found the 6-DoF position and orientation of the fiducial frame is known in the scanner coordinate frame. With the Z-Frame rigidly attached to the robot it follows that the kinematic motion of the robot can now be expressed in scanner coordinates as well. Figure 6.15 shows the Z-Frame, the assembly as seen on the robot and an MR image slice showing each of the nine fiducial markers.

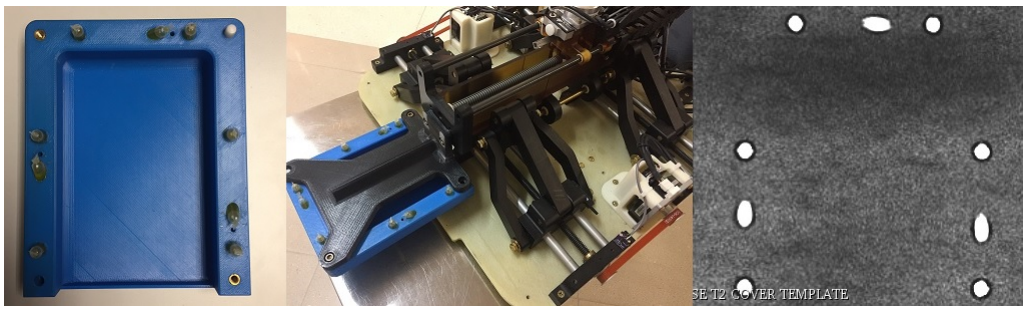

Figure 6.15: The Z-Frame used for robot-scanner registration. Left) The 3D printed Z-Frame which holds nine MR visible fiducials in perpendicular "Z" configurations, Center) the Z-Framer attached to the robot, Right) an MR image slice showing the fiducial markers used to register the robot location to scanner coordinates.

With the Z-frame rigidly attached, the robot was placed on the patient board inside the MR bore as described in 6.2. The transformation from the robot home coordinate frame to the Z-frame coordinate frame, $T^{Home}_{Z-frame}$, is known from kinematic values of the robot. Imaging the Z-frame gives the transformation from the isocenter of the scanner to the Z-frame, $T^{Scanner}_{Z-frame}$. With these two transformations the robot home coordinate frame can be registered to the scanner coordinate frame by the mul-

tiplication in Eq. 6.4. Figure 6.16 shows the coordinate frames and transformations used to register the robot location to the MRI scanner.

$$T_{Home}^{Scanner} = T_{Z-frame}^{Scanner} {T_{Z-Frame}^{Home}}^{-1} \tag{6.4}$$

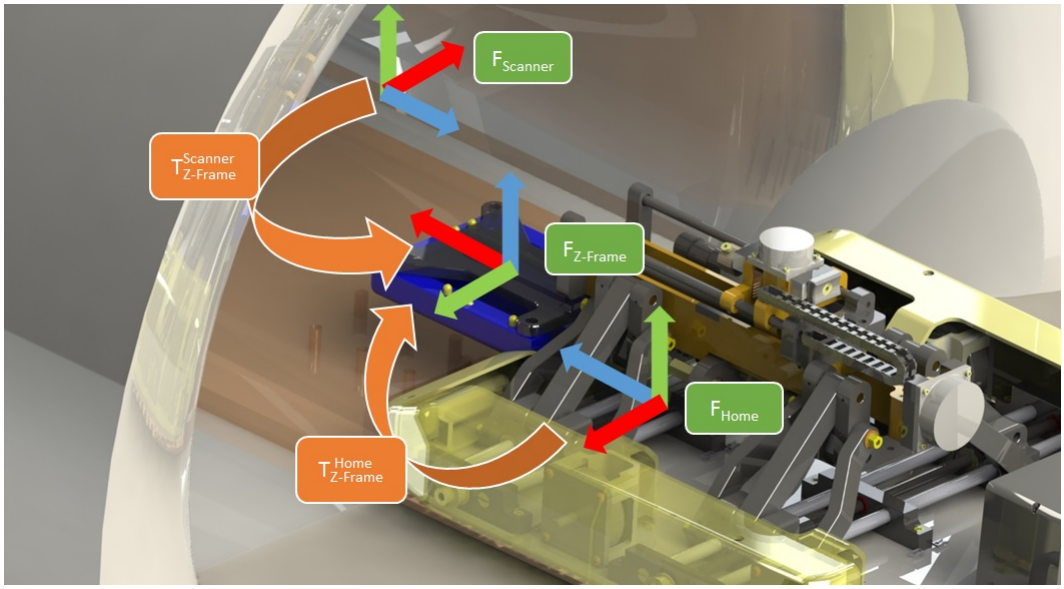

Figure 6.16: Coordinate systems and transformations necessary to register the robot to the scanner coordinate frame. Transformations shown are between robot home and the the fiducial Z-Frame, as well as the scanner isocenter and the fiducial Z-Frame. With these two transformations the robot home can be registered to scanner coordinates.

6.5.1.6 Preoperative Planning

Once registration was performed the Z-frame was removed, the needle guide attached back into place and the biopsy gun put in place on the robot. Additionally, the phantom to be used in the experimental trial was placed in the typical targeting region of the robot and covered with the body imaging coil as seen in Fig. 6.17.

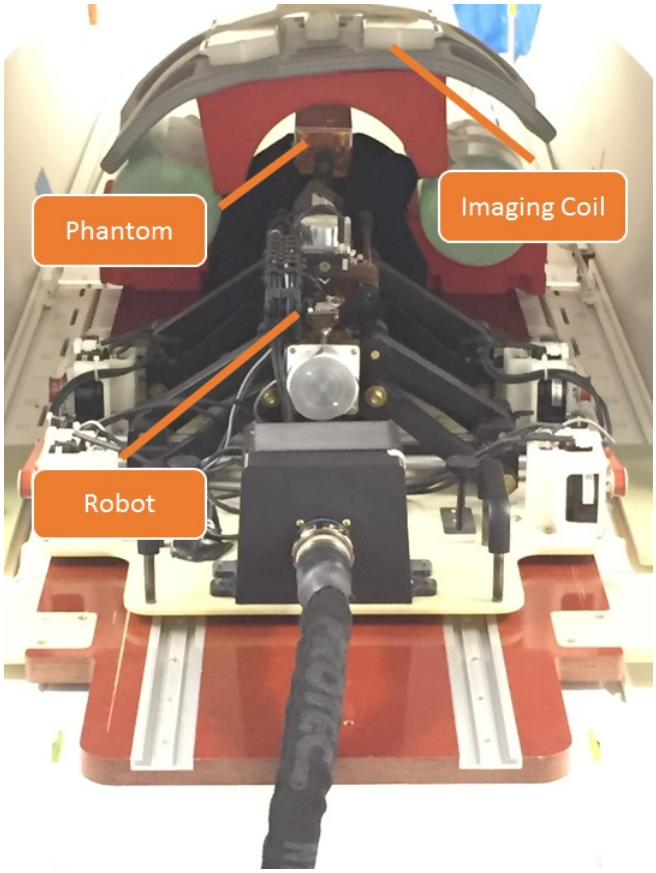

Figure 6.17: The in-bore experimental setup. The phantom was placed in the typical targeting region for prostate interventions and the same imaging coil as in clinical biopsy was used.

After the phantom was secured the scanner bed was moved to place the phantom

at the isocenter of the bore. A set of preoperative images was taken to segment the anatomical structures present, identify the target and determine any membranes to detect throughout insertion. The preoperative images were sent from the scanner console to 3DSlicer, and the target as well as membranes were identified by placement of a fiducial marker at their location. All three of the X, Y, Z values of the target fiducal marker were sent the robot control application, where as only the estimated depth of the membrane location was sent to the controller. Figure 6.18 is the annotated 3DSlicer interface, showing the heterogeneous phantom, target point, membrane depths, and the OpenIGTLink connection to the controller box.

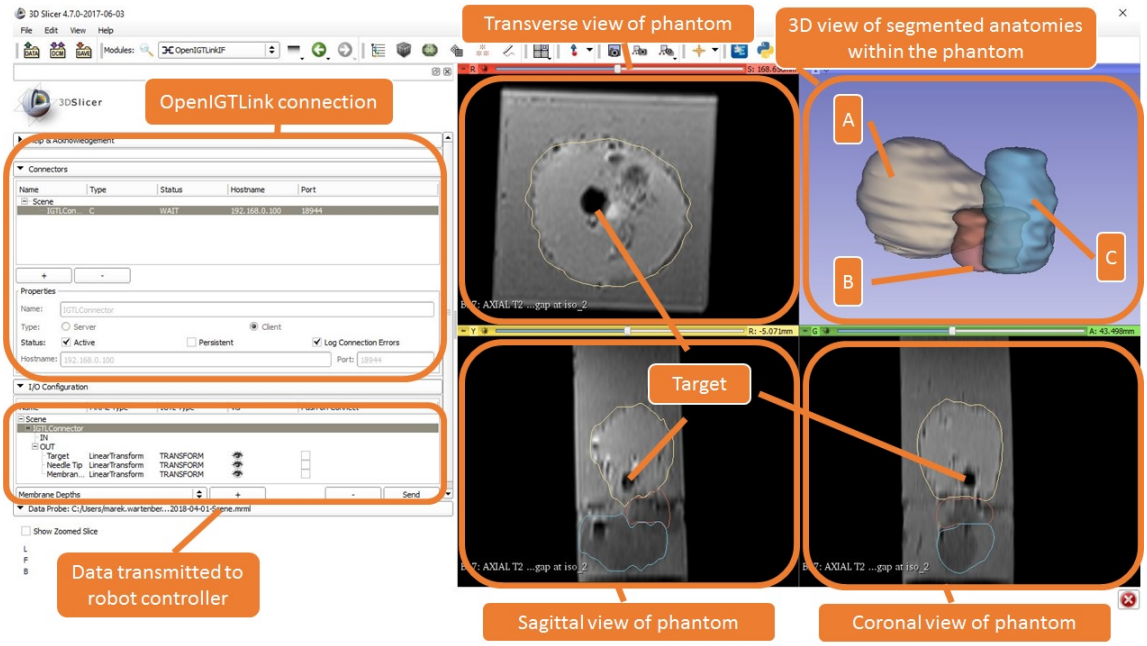

Figure 6.18: Preperative Planning in 3DSlicer. Three views in each of the anatomical planes is shown, as well as a 3D view of the segmented structures. The structures segmented for this experiment were A: prostate, B: corpus spongiosum and C: bulbospongiosus. An OpenIGTLink network connection is opened with the controller box and information of target, needle tip and membrane depths passed one-way to the control software.

6.5.1.7 Closed-Loop Needle Insertion

After preoperative planning was complete and the target point was sent to the robot controller and the foot pedal safety switch was pressed and the robot base moved to align the needle to a straight line trajectory to the target. With the needle aligned to an initial straight light trajectory a cooperative needle insertion began. In

the case of puncture detection with the multi-layered phantoms a continuous insertion was performed under real-time imaging. For targeting using the anatomical phantom an input force was applied to insert the needle a stepwise distance of approximately $5 - 10mm$. An intraoperative T2 weighted TSE scan was taken, the images sent to 3DSlicer, the needle tip and target localized and the updated positions sent to the control box. Using this updated information, the cooperative and compensatory control parameters were determined as described in Chapters 4 and 5 respectively. Insertion continued in this manner under cooperative control until the needle reached the target depth, continuously updating the control parameters for cooperative insertion and active compensation. The control software logged when a membrane was detected, and an enhanced haptic response in the form of a short insertion jitter was provided to the user upon detection. Once the target was reached a final set of images were taken and the in-plane targeting error was determined at the target depth.

6.5.2 Results

6.5.2.1 Puncture Detection Under Real-Time Imaging

Ten trials of continuous needle insertion through layered phantoms were performed, five on a phantom with a single transition: soft to stiff, and five on a phantom with a double transition: soft-stiff-soft. Figure 6.19 shows an MR image of the three layered phantom with the layers different PVC concentrations clearly vis-

ible. The depth of each membrane transition was passed to the robot controller via OpenIGTLink from 3DSlicer. Throughout these insertions, the system detected all 5 punctures of the single transition phantom and 9/10 punctures of double transition phantom, only missing one of the deep ($> 50mm$) transitions, providing a haptic response in each detected case.

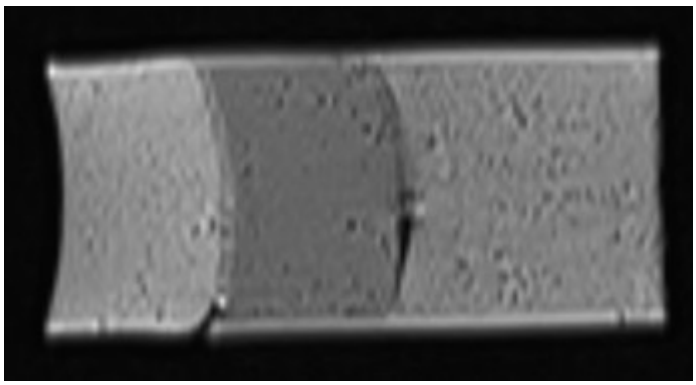

Figure 6.19: An MR image of the multi-layered phantom used for in-bore validation of membrane puncture detection

6.5.2.2 Closed-Loop Targeting using MR Image-Feedback

In-bore actively compensated cooperative needle insertions were performed towards five stationary targets with an added membrane to detect during each insertion. Each of these trials closely mimicked the validation studies performed in the lab where the CURV algorithm was used and the direction of desired compensatory was updated throughout insertion. Figure 6.20 shows two MR images during needle insertion, with puncture detected in each of the five cases and a haptic response felt by the user.

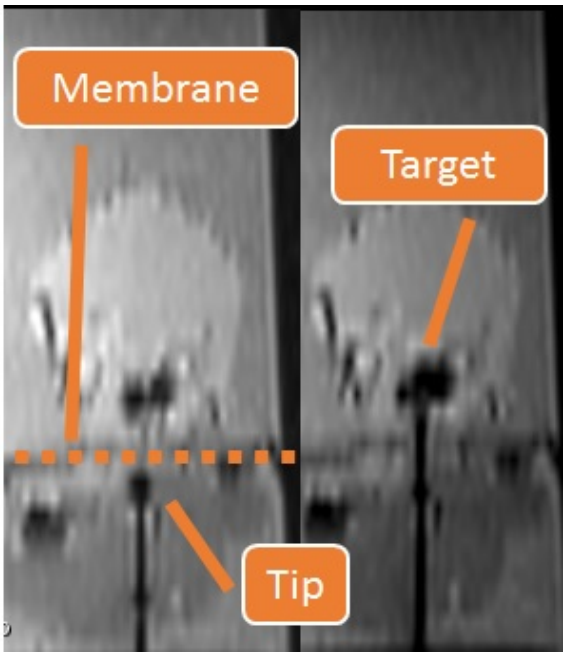

Figure 6.20: MR images showing targeting before and after membrane puncture. Coronal images of a needle insertion into a heterogeneous phantom with a polyimide layer to act as a membrane. Puncture was successfully detected in each of the five in-bore insertion trials using the algorithm described in Chapter 4.

Similarly to the in lab tests described in Chapter 5, final targeting error was defined as in-plane error between the needle tip and target calculated at the target depth, as this was the error criteria used in clinical trials of the robot base. The coordinates of each target point and final tip location were directly available in 3DSlicer, and the in-plane magnitude between the two points was identified as the targeting error. The in-plane targeting error across all trials was $3.42 mm_{rms}$.

The anatomical structures of the phantom were segmented from MR images to create a 3D visualization of the phantom. Using the final confirmation image of each

needle insertion, the needle trajectories were plotted in 3DSlicer using the CurveMaker module. A 3D visualization of the segmented structures and each insertion trajectory towards its target is shown in Fig. 6.21.

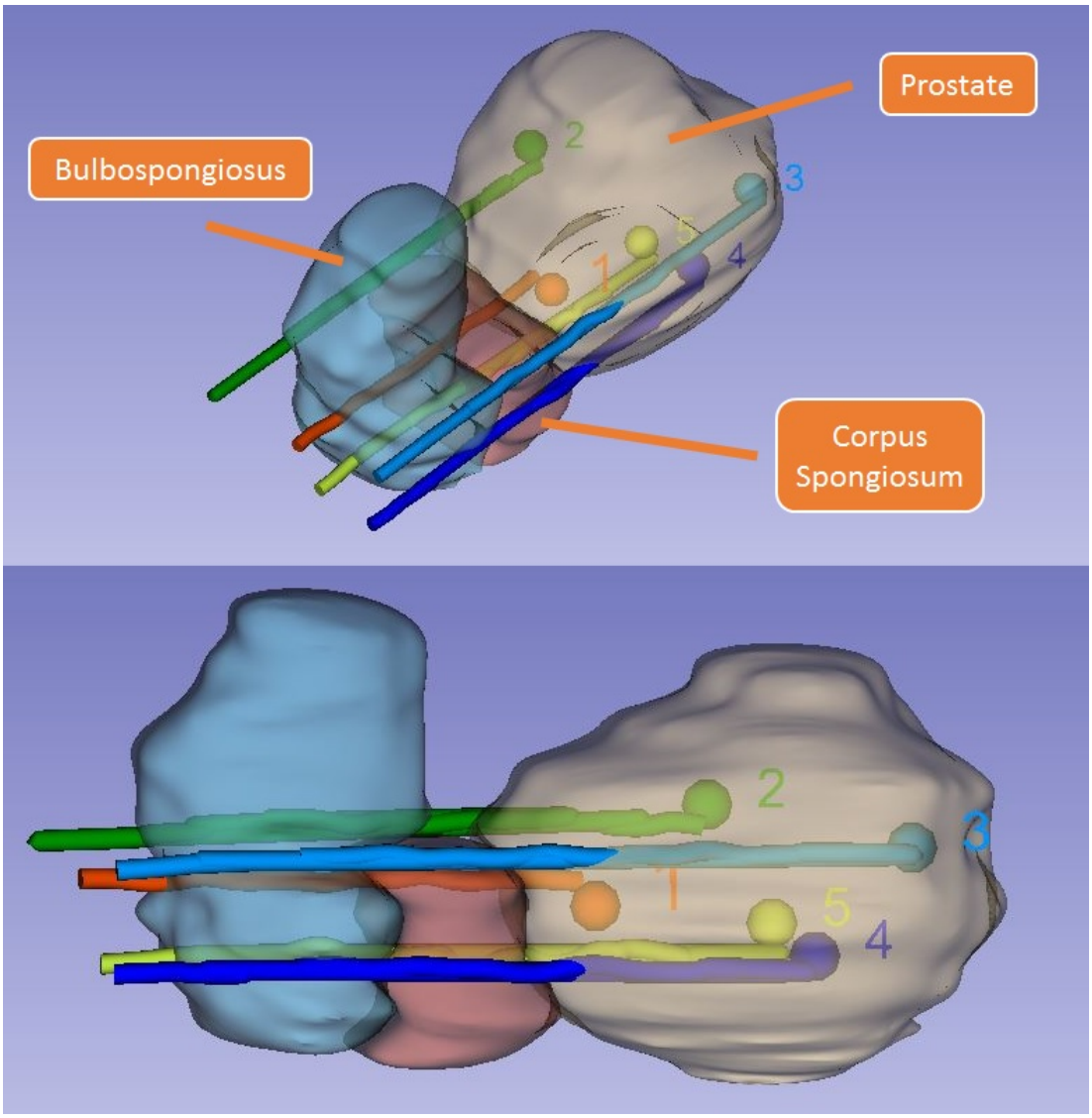

Figure 6.21: In-bore needle insertion trajectories. Each of the five needle trajectories performed during in-bore validation testing. These insertions were performed into a heterogeneous phantoms made with molded anatomical structures that were segmented from anonymized MR images.

6.6 Discussion and Conclusions

System integration was performed to prepare for clinical translation, and the workflow to collect an MRI guided targeted biopsy using the robot base was largely implemented. The same patient board was used, the robot and control boxes maintained their previous positions, and the cooperative controlled needle driver requires the user to perform the hands-on insertion directly at the surgical site.

SNR analysis was evaluated for the complete system and showed a 10% to 15% drop in signal quality when the robot was place in the MR-bore, much less that the 80% seen without shielding, and the 40% - 60% degredation that has been previously seen even with shielding [26, 123].

With several new functional robotic subsystems developed, a web GUI was used to integrate control of the robot into a single application. The system state of the robot was chosen from the GUI, and all sensor data was displayed for the user. The 3DSlicer navigation software communicated to the robot controller via OpenIGTLink, and the C++ application ran high level code to determine the desired robot function.

Final system validation took place in the AMIGO suite at Brigham and Women's Hospital. Cooperative needle insertions were performed into heterogeneous phantoms characterized to mimic periprostatic tissue. A polyimide layer was molded into the phantom to act as a membrane and the system was able to detect puncture in each case. During targeting trials under cooperative insertion, rotational bevel tip position was set using the CURV steering method for active compensation from an

initial straight line trajectory. The final targeting error across all five insertions was $3.42mm_{rms}$, comparable to the $3.56mm_{rms}$ targeting error found during in-lab tests towards a stationary target.

Chapter 7

Conclusions and Future Extension

The goal of this research was to increase the interventional outcomes of targeted prostate biopsy. If a target is not reached with sufficient accuracy a physician often retracts the needle without taking a sample and must restart with a new attempt, lengthening procedure time, increasing cost and causing unnecessary discomfort to the patient.

Full robotic control of needle insertion is expected to be the most accurate way to place a needle tip for biopsy, but this leap from the clinical standard of practice would likely be met with caution from both acting physicians as well as regulatory bodies. Instead, through user directed control via a cooperative insertion paradigm, a physician would maintain full control of the procedure directly at the procedure site, while adding the benefit of robotic accuracy. Continuous haptic feedback can be provided via force sensing of needle interaction with tissue, returning the tactile

forces used by the physician for anatomical localization, which would typically be lost when migrating to robotic insertion. Furthermore, an enhanced haptic response can be provided during a hands-on cooperative insertion, for instance a scaled force for event based detection of membrane puncture.

From a tissue interaction stand point, a cooperative insertion is just a variable velocity insertion, therefore as long as accurate feature localization is provided to update rotational bevel positioning, the targeting accuracy should be comparable whether performed with autonomous or cooperative insertion. This dissertation showed a method for closed-loop image-guided active compensation of unmodeled needle deflection and target shift, showing no statistical difference between targeting accuracy under autonomous robotic needle insertion versus user directed hands-on cooperative needle insertion.

The work performed in completion of this dissertation was with respect to clinical translation and each subsystem was integrated to function within the clinical environment. Physician consultation and observation of procedures performed using the standard clinical practice shaped the design requirements for all aspects of the robotic system, and how it was integrated to maintain as close as possible the current clinical workflow.

7.1 Summary of Work and Contributions

A summary of contributions and the work performed throughout completion of this dissertation is presented. This is followed by the impact of the work, some lessons learned and how this work can be extended in the future.

- **Scientific Contributions**

  - **Complete Robotic System for Prostate Biopsy** A robotic alignment base previously used in clinical trials of robot assisted biopsy was fitted with a custom needle driver suitable for use within the MR-bore and configured for cooperatively controlled robotic needle insertion. This needle driver collects both user input and needle-tissue interaction force to incorporate robotic accuracy of needle placement while providing feedback to the physician in ultimate control of the procedure. The system architecture includes the robotic manipulator, a shielded robot controller and a workstation outside the scanner room running a control application along with surgical navigation software 3DSlicer.

  - **Cooperative Control Algorithm For Robotic Needle Insertion** Employing the developed needle driver, insertion is performed through user initiated hands-on cooperative control. Input and needle-tissue interaction forces are collected and the output velocity is a non-linear relationship between the two. This relationship is scalable by an exponential

decay constant, allowing for faster insertion early in insertion and higher sensitivity when the forces approach each other. This configuration can restore the tactile feedback surgeons surrender in exchange for robotic accuracy, in addition to adding augmented feedback to enhance perception not able to be detected by the user alone.

  - **Paired Force Sensor and Image Based Membrane Puncture** As the forces on the needle are being collected for cooperative control, this information can be used to provide an augmented haptic feedback at detection of a membrane puncture. Due to needle deflection and target shift, kinematic motion of the robot cannot guarantee a specific depth has been reached. In addition, force sensor data could provide false detection of a membrane puncture if used exclusively. By pairing a location of estimated membrane depth via imaging, a window can be created to monitor the force sensor data for a puncture event. Additionally, anatomically representative tissue phantoms were created by 3D printing molds of segmented structures from anonymized MR images. These molds were filled with PVC concentrations characterized to mimic the mechanical properties of periprostatic tissue to accurately validate puncture detection and targeting accuracy.

- **Engineering Contributions**

– **Active compensation through autonomous rotational bevel tip positioning** During cooperative insertion, the system is designed to autonomously rotate the needle to position the bevel tip in the directly of desired deflection. Insertion through multiple layers of different tissue will inherently deflect the needle from an initial straight-line trajectory, and image-feedback can be used to rotate the needle to compensate for this. Information of needle tip and target localization is passed one-way downstream from the image-guidance software to the robot controller via the OpenIGTLink communication protocol, and the robot controller is agnostic to the imaging source providing this information.

– **System Integration and Validation** Integration of hardware and software subsystems was performed for experimental validation of the system in the clinical environment. The system hardware was designed to maintain a similar workflow as seen in clinical trials and the needle driver design inherently maintained sterilization techniques used. A web GUI was used for control of software subsystems, and this was integrated with the surgical navigation software and the MRI scanner console in the complete system architecture. The full robotic system was tested inside the MR-bore, performing targeted needle insertions under cooperative control with autonomous rotational bevel tip positioning for active compensation, along with paired imaging and force sensor membrane puncture detection.

7.2 Impact, Lessons Learned and Future Work

The research presented in this dissertation addresses several major challenges. As the second leading cause of cancer related death among men in the United States, prostate cancer diagnosis must be improved. Current techniques of serial biopsy core retrieval under TRUS is susceptible to under sampling leading to repeat biopsy procedures and under diagnosis of clinically significant prostate cancer. The work performed throughout completion of this dissertation aims to address this.

Impact

The biggest impact of this work is attempting to address a real-life problem with a real-life solution. With slight modifications to this already built and validated system, cadaver and pre-clinical animal trials could be performed within the next year, with in-human trials within the next two to three. Moving from serial sampling of the prostate to a targeted biopsy of a specific suspicious location decreases the length, cost and recovery time of the procedure. Furthermore, retrieval of biopsy cores from these suspicious locations rather than pseudo-randomly throughout the prostate can avoid unnecessary repeat procedures where no cancer is detected but levels of PSA continue to rise.

This work specifically builds upon clinical trials of robot assisted prostate biopsy, where the insertion was still performed manually by the physician and suffered from

decreased targeting accuracy due to unmodeled needle deflection and target shift. Development of a robotic needle driver capable of rotational bevel tip positioning of the clinical biopsy gun for active compensation can decrease the interference of these unmodeled sources of error on final needle tip placement. Furthermore, incorporating a cooperatively controlled needle insertion as opposed to fully autonomous biopsy retrieval, the physician remains as the surgical site in full control of the procedure.

Lessons Learned

Most of the lessons learned throughout completion of this dissertation are based on the collaborative engineering approach. Not only should physicians and engineers communicate early on to accurately develop specifications, but design should happen from a full-systems approach and each system should be developed concurrently from predefined specifications. A great example of this is accounting for cable management in robot design. There is certainly more that goes into moving from a CAD design to a full system, but nothing explains the difference between a compartmentalized and a full-systems approach quite like incorporating cable management early on in design. Often overlooked, physical routing of cables must also take into account kinematic motion of a robot, include strain relief, be maintainable and not affect maintenance of other components. Additionally, this requires a specification of the electrical design early on, as the wire gauges and number of cables traveling to different locations in the system must be known. It follows that integrated circuits and microprocessors also require certain electrical specifications so control system requirements are then

necessary to develop early on as well. Through simply starting with consideration of cable management, it is concluded early on that a full-systems approach is necessary produce a high-quality finished product on budget in a timely manner.

Specific lessons regarding development of this system were learned, and if starting over a few considerations would be made. Most importantly, actuation of the needle driver would likely be implemented via timing belts rather than a lead screw. A lead screw was chosen to build off the robot base design, allowing for non-backdrivable insertion with enough force to overcome needle-tissue interaction up to $150mm$ deep. In redesign of the needle driver, a pulley and timing belt implementation would likely be pursued to: 1) reduce the impact of the system on image SNR by eliminating the aluminum lead screw near the imaging volume, 2) shrink the overall size of the needle driver, 3) increase variability of insertion speeds, and 4) provide a safer option for emergency needle retraction. As the system is currently configured, in an emergency the entire robot must be slid back to remove the needle from the body. Instead, a pulley and timing belt implementation would allow for easier decoupling of the insertion axis for emergency retraction.

Future Work

As the effort in this dissertation was towards clinical translation, future work continues this path forward. Prior to this work the robotic system simply aligned a needle guide in which a physician would perform a manual needle insertion through. Now the system is capable of cooperative insertion alongside closed-loop autonomous needle

rotation. A cooperatively controlled robotic biopsy is more likely to gain acceptance by physicians over teleoperation due to maintaining proximity to the surgical site, but regulatory hurdles regarding robotic needle insertion still exist. To move from the current state to clinical trials, the system would benefit from a new National Institutes of Health (NIH) R01 grant intended specifically for clinical translation.

The current robotic system framework is suitable for clinical use and function was validated in-bore at Brigham and Women's Hospital in Boston, MA. With a new R01 grant some modifications could be made to the system to further increase the chance of regulatory approval, such as: 1) redesign the needle driver for increased safety as described in the previous section, 2) replace the force sensors and encoders with fiber optic counterparts, 3) replace the aluminum lead screws in the base with ceramic versions to limit metallic components and increase SNR, 4) add a dynamic needle model to pair with active compensation to increase the accuracy of needle tip localization, 5) implement more robust exception handling for undesired behaviors, 6) develop motion planning for collision detection, and 8) push verified functionality down to FPGA.

Additionally, a redesign of the needle driver should incorporate a clutch to easily allow for disengagement of the insertion motor. This would create a system for biopsy with hands on encoded insertion, without robotic control. This could be a first step in regulatory approval, a controlled hands-on insertion pushed along the linear guides with autonomous rotational compensation.

With these modifications made the system could be ready for cadaver and pre-clinical animal trials within one year. Following a set of successful animal trials with positive interventional outcomes, approval from an Institutional Review Board (IRB) followed by an application for an Investigational Device Exception (IDE) from the Food and Drug Administration (FDA) could lead into clinical trials within the next two to three years.

References

[1] R. L. Siegel, K. D. Miller, and A. Jemal, "Cancer statistics, 2015," *CA: A Cancer Journal for Clinicians*, vol. 65, no. 1, pp. 5–29, 2015.

[2] A. C. Society, "Cancer facts and figures 2018," *America Cancer Society*, 2018.

[3] G. S. Fischer, I. Iordachita, C. Csoma, J. Tokuda, S. P. DiMaio, C. M. Tempany, N. Hata, and G. Fichtinger, "Mri-compatible pneumatic robot for transperineal prostate needle placement," *Mechatronics, IEEE/ASME Transactions on*, vol. 13, no. 3, pp. 295–305, 2008.

[4] N. C. Institute, "Development and preliminary evaluation of a motorized needle guide template for mri-guided targeted prostate biopsy," *National Institutes of Health*, vol. NIH, no. 12-1576, 2012.

[5] J. E. McNeal, "Regional morphology and pathology of the prostate," *American Journal of Clinical Pathology*, vol. 49, no. 3, pp. 347–357, 1968.

[6] R. J.Cohen, B. A. Shannon, M. Phillips, R. E. Moorin, T. M.Wheeler, and K. L.Garrett, "Central zone carcinoma of the prostate gland: A distinct tumor type with poor prognostic features," *The Journal of Urology*, vol. 179, no. 5, pp. 1762 – 1767, 2008.

[7] P. Mohan, H. Ho, J. Yuen, W. S. Ng, and W. S. Cheng, "A 3d computer simulation to study the efficacy of transperineal versus transrectal biopsy of the prostate," *International Journal of Computer Assisted Radiology and Surgery*, vol. 1, pp. 351–360, 2007.

[8] G. Kelloff, P. Choyke, and D. Coffey, "Challenges in clinical prostate cancer:

Role of imaging," in *American Journal of Roentgenology*, vol. 192, no. 6, pp. 1455–1470, 2009.

[9] M. Han, D. Chang, C. Kim, B. Lee, Y. Zuo, K. H-J, D. Petrisor, B. Trock, A. Partin, R. Rodriuguez, H. Carter, M. Allaf, J. Kim, and D. Stoianovici, "Geometric evaluation of systematic transrectal ultrasound guided prostate biopsy," in *Journal of Urology*, vol. 188, no. 6, pp. 2404–2409, 2012.

[10] B. Djavan and M. Margreiter, "Biopsy standards for detection of prostate cancer," *World Journal of Urology*, vol. 25, no. 1, pp. 11–17, 2007.

[11] H. Hricak, P. L. Choyke, S. C. Eberhardt, S. A. Leibel, and P. T. Scardino, "Imaging prostate cancer: A multidisciplinary perspective," *Radiology*, vol. 243, no. 1, pp. 28–53, 2007.

[12] J. F. Schenck, F. A. Jolesz, P. B. Roemer, H. E. Cline, W. E. Lorensen, R. Kikinis, S. G. Silverman, C. J. Hardy, W. D. Barber, E. T. Laskaris, B. Dorri, R. W. Newman, C. E. Holley, B. D. Collick, D. P. Dietz, D. C. Mack, S. P. Souza, C. L. Dumoulin, R. D. Darrow, R. L. S. Peters, K. W. Rohling, R. D. Watkins, D. R. Eisner, S. M. Blumenfeld, and K. G. Vosburgh, "Superconducting open-configuration mr imaging system for image-guided therapy." *Radiology*, vol. 195, no. 3, pp. 805–814, 1995.

[13] M. P. Fried, L. Hsu, G. P. Topulos, and F. A. Jolesz, "Imageguided surgery in a new magnetic resonance suite: Preclinical considerations," *The Laryngoscope*, vol. 106, no. 4, pp. 411–417, 1996.

[14] F. Jolesz, "Image-guided procedures and the operating room of the future," *Radiology*, vol. 204, pp. 601–612, 1996.

[15] N. L. Robertson, Y. Hu, H. U. Ahmed, A. Freeman, D. Barratt, and M. Emberton, "Prostate cancer risk inflation as a consequence of image-targeted biopsy of the prostate: a computer simulation study," *European urology*, vol. 65, no. 3, pp. 628–634, 2014.

[16] R. C. Susil, C. Mnard, A. Krieger, J. A. Coleman, K. Camphausen, P. Choyke, G. Fichtinger, L. L. Whitcomb, C. N. Coleman, and E. Atalar, "Transrectal

prostate biopsy and fiducial marker placement in a standard 1.5t magnetic resonance imaging scanner," *Journal of Urology*, vol. 175, no. 1, pp. 113–120, 2006.

[17] D. Beyersdorff, A. Winkel, B. Hamm, S. Lenk, S. A. Loening, and M. Taupitz, "Mr imagingguided prostate biopsy with a closed mr unit at 1.5 t: Initial results," *Radiology*, vol. 234, no. 2, pp. 576–581, 2005.

[18] A. V. D'Amico, C. M. Tempany, R. Cormack, M. Hata, N. Jinzaki, K. Tuncali, M. Weinstein, and J. P. Richie, "Transperineal magnetic resonance image guided prostate biopsy," *Journal of Urology*, vol. 164, no. 2, pp. 385–387, 2000.

[19] K. M. Pondman, J. J. Ftterer, B. ten Haken, L. J. Schultze Kool, J. A. Witjes, T. Hambrock, K. J. Macura, and J. O. Barentsz, "Mr-guided biopsy of the prostate: An overview of techniques and a systematic review," *European Urology*, vol. 54, no. 3, pp. 517–527, 2008.

[20] D. N. Costa, I. Pedrosa, J. Francisco Donato, C. G. Roehrborn, and N. M. Rofsky, "Mr imagingtransrectal us fusion for targeted prostate biopsies: Implications for diagnosis and clinical management," *RadioGraphics*, vol. 35, no. 3, pp. 696–708, 2015.

[21] V. Kasivisvanathan, A. S. Rannikko, M. Borghi, V. Panebianco, L. A. Mynderse, M. H. Vaarala, A. Briganti, L. Budus, G. Hellawell, R. G. Hindley, M. J. Roobol, S. Eggener, M. Ghei, A. Villers, F. Bladou, G. M. Villeirs, J. Virdi, S. Boxler, G. Robert, P. B. Singh, W. Venderink, B. A. Hadaschik, A. Ruffion, J. C. Hu, D. Margolis, S. Crouzet, L. Klotz, S. S. Taneja, P. Pinto, I. Gill, C. Allen, F. Giganti, A. Freeman, S. Morris, S. Punwani, N. R. Williams, C. Brew-Graves, J. Deeks, Y. Takwoingi, M. Emberton, and C. M. Moore, "Mri-targeted or standard biopsy for prostate-cancer diagnosis," *New England Journal of Medicine*, vol. 0, no. 0, p. null, 2018.

[22] C. Filson, D. Margolis, J. Huang, S. Natarajan, P. Lieu, F. Dorey, and L. Marks, "Mr-us fusion biopsy: Importance of both systematic and targeted sampling to diagnose prostate cancer," *Journal of Urology*, vol. 193, no. 4, pp. e120–e121, 2015.

[23] G. A. Sonn, E. Chang, S. Natarajan, D. J. Margolis, M. Macairan, P. Lieu, J. Huang, F. J. Dorey, R. E. Reiter, and L. S. Marks, "Value of targeted prostate biopsy using magnetic resonance-ultrasound fusion in men with prior negative biopsy and elevated prostate-specific antigen," *European Urology*, vol. 65, no. 4, pp. 809–815, 2014.

[24] C. Filson, D. Margolis, J. Huang, S. Natarajan, P. Lieu, F. Dorey, R. Reiter, and L. Marks, "Mr-us fusion biopsy to diagnose prostate cancer: First 1000 men at ucla," *Journal of Urology*, vol. 193, no. 4, p. e564, 2015.

[25] T. Penzkofer, K. Tuncali, A. Fedorov, S.-E. Song, J. Tokuda, F. M. Fennessy, M. G. Vangel, A. S. Kibel, R. V. Mulkern, W. M. Wells, N. Hata, and C. M. C. Tempany, "Transperineal in-bore 3-t mr imagingguided prostate biopsy: A prospective clinical observational study," *Radiology*, vol. 274, no. 1, pp. 170–180, 2015.

[26] A. Krieger, S. E. Song, N. B. Cho, I. I. Iordachita, P. Guion, G. Fichtinger, and L. L. Whitcomb, "Development and evaluation of an actuated mri-compatible robotic system for mri-guided prostate intervention," *IEEE/ASME Transactions on Mechatronics*, vol. 18, no. 1, pp. 273–284, 2013.

[27] H. Elhawary, Z. T. H. Tse, M. Rea, A. Zivanovic, B. L. Davies, C. Besant, N. de Souza, D. McRobbie, I. Young, and M. Lamperth, "Robotic system for transrectal biopsy of the prostate: Real-time guidance under mri," *IEEE Engineering in Medicine and Biology Magazine*, vol. 29, no. 2, pp. 78–86, 2010.

[28] J. Cepek, B. Chronik, U. Lindner, J. Trachtenberg, and A. Fenster, "Development of an mri-compatible device for prostate focal therapy," in *Medical Image Computing and Computer-Assisted Intervention – MICCAI 2012*. Berlin, Heidelberg: Springer Berlin Heidelberg, 2012, pp. 455–462.

[29] D. Yakar, M. G. Schouten, D. G. H. Bosboom, J. O. Barentsz, T. W. J. Scheenen, and J. J. Ftterer, "Feasibility of a pneumatically actuated mr-compatible robot for transrectal prostate biopsy guidance," *Radiology*, vol. 260, no. 1, pp. 241–247, 2011.

[30] S. Zangos, K. Eichler, K. Engelmann, M. Ahmed, S. Dettmer, C. Herzog, W. Pegios, A. Wetter, T. Lehnert, M. G. Mack *et al.*, "Mr-guided transgluteal biopsies with an open low-field system in patients with clinically suspected prostate cancer: technique and preliminary results," *European radiology*, vol. 15, no. 1, pp. 174–182, 2005.

[31] S. Zangos, K. Eichler, A. Thalhammer, J. Schoepf, P. Costello, C. Herzog, M. Mack, and T. Vogl, "Mr-guided interventions of the prostate gland," *Minimally Invasive Therapy & Allied Technologies*, vol. 16, no. 4, pp. 222–229, 2007.

[32] A. F2503-13, "Standard practice for marking medical devices and other items for safety in the magnetic resonance environment," *ASTM International*, 2013.

[33] J. Futterer, S. Misra, and J. Macura, "Mri of the prostate: Potential role of robots," *Imaging in Medicine*, vol. 2, no. 5, pp. 583–592, 2010.

[34] J. Troccaz, M. Peshkin, and B. Davies, "Guiding systems for computeraided surgery: introducing synergistic devices and discussing the different approaches," *Medical Image Analysis*, vol. 2, no. 2, pp. 101–119, 1988.

[35] N. Patel, G. Li, W. Shang, M. Wartenberg, T. Heffter, E. Burdette, I. Iordachita, J. Tokuda, N. Hata, C. Tempany, and G. Fischer, "System integration and preliminary clinical evaluation of a robotic system for mri guided transperineal prostate biopsy (accepted)," *Journal of Medical Robotics Research*, 2018.

[36] J. Tokuda, K. Tuncali, N. Li, G an Patel, T. Heffter, G. Fischer, I. Iordachita, E. Burdette, N. Hata, and C. Tempany, "In-bore mri-guided transperineal prostate biopsy using 4-dof needle-guide manipulator," in *International Society for Magnetic Resonance in Medicine, Annual Meeting*, 2016.

[37] D. Comber and E. Barth, "Precision position tracking of mr-compatible pneumatic piston-cylinder using sliding mode control," in *ASME 2011 Dynamic Systems and Control Conference and Bath/ASME Symposium on Fluid Power and Motion Control*, 2011, pp. 45–51.

[38] M. van den Bosch, M. Moman, J. van Vulpen, E. Duiveman, L. van Schelven, H. de Leeuw, J. Lagendijk, and M. Moerland, "Mri-guided robotic system

for transperineal prostate interventions: proof of principle," *Phys. Med. Biol.*, vol. 55, pp. 133–140, 2010.

[39] V. Lagerburg, M. A. Moerland, M. K. Konings, R. E. van de Vosse, J. J. W. Lagendijk, and J. J. Battermann, "Development of a tapping device: a new needle insertion method for prostate brachytherapy," *Physics in Medicine and Biology*, vol. 51, no. 4, p. 891, 2006.

[40] B. Yang, U. Tan, A. McMillan, R. Gullapalli, and J. Desai, "Design and implementation of a pneuymatically-actuated robot for breast biopsy under continuous mri," in *Robotics and Automation, 2011 IEEE International Conference on*, 2011, pp. 674–679.

[41] D. Stoianovici, A. Patriciu, D. Mazilu, D. Petrisor, and L. Kavoussi, "A new type of motor: Pneumatic step motor," *IEEE/ASME Trans. Mechatronics*, vol. 12, no. 1, pp. 98–106, 2007.

[42] D. Stoianovici, D. Song, D. Petrisor, D. Ursu, D. Mazilu, M. Mutener, M. Schar, and A. Patriciu, "mri stealth robot for prostate interventions," *Minimally Invasive Therapy & Allied Technologies*, vol. 16, no. 4, pp. 241–248, 2007.

[43] D. Stoianovici, C. Kim, G. Srimathveeravalli, P. Sebrecht, D. Petrisor, J. Coleman, S. B. Solomon, and H. Hricak, "Mri-safe robot for endorectal prostate biopsy," *Mechatronics, IEEE/ASME Transactions on*, vol. 19, no. 4, pp. 1289–1299, 2014.

[44] Y. Chen, K.-W. Kwok, and Z. T. H. Tse, "An mr-conditional high-torque pneumatic stepper motor for mri-guided and robot-assisted intervention," *Annals of Biomedical Engineering*, vol. 42, no. 9, pp. 1823–1833, Sep 2014.

[45] S. Zangos, C. Herzog, K. Eichler, R. Hammerstingl, A. Lukoschek, S. Guthmann, B. Gutmann, U. J. Schoepf, P. Costello, and T. J. Vogl, "Mr-compatible assistance system for punction in a high-field system: device and feasibility of transgluteal biopsies of the prostate gland," *European Radiology*, vol. 17, no. 4, pp. 1118–1124, 2007.

[46] S. Zangos, A. Melzer, K. Eichler, C. Sadighi, A. Thalhammer, B. Bodelle, R. Wolf, T. Gruber-Rouh, D. Proschek, R. Hammerstingl, C. Mller, M. G. Mack,

and T. J. Vogl, "Mr-compatible assistance system for biopsy in a high-field-strength system: Initial results in patients with suspicious prostate lesions," *Radiology*, vol. 259, no. 3, pp. 903–910, 2011.

[47] S. P. DiMaio, S. Pieper, K. Chinzei, N. Hata, S. J. Haker, D. F. Kacher, G. Fichtinger, C. M. Tempany, and R. Kikinis, "Robot-assisted needle placement in open mri: System architecture, integration and validation," *Computer Aided Surgery*, vol. 12, no. 1, pp. 15–24, 2007.

[48] A. A. Goldenberg, J. Trachtenberg, W. Kucharczyk, Y. Yi, M. Haider, L. Ma, R. Weersink, and C. Raoufi, "Robotic system for closed-bore mri-guided prostatic interventions," *IEEE/ASME Transactions on Mechatronics*, vol. 13, no. 3, pp. 374–379, 2008.

[49] Z. T. H. Tse, H. Elhawary, M. Rea, B. Davies, I. Young, M. Lamperth *et al.*, "Haptic needle unit for mr-guided biopsy and its control," *Mechatronics, IEEE/ASME Transactions on*, vol. 17, no. 1, pp. 183–187, 2012.

[50] S. E. Song, J. Tokuda, K. Tuncali, C. M. Tempany, E. Zhang, and N. Hata, "Development and preliminary evaluation of a motorized needle guide template for mri-guided targeted prostate biopsy," *IEEE Transactions on Biomedical Engineering*, vol. 60, no. 11, pp. 3019–3027, 2013.

[51] Y. Koseki, T. Washio, K. Chinzei, and H. Iseki, "Endoscope manipulator for trans-nasal neurosurgery, optimized for and compatible to vertical field open mri," in *Medical Image Computing and Computer-Assisted Intervention — MICCAI 2002*, T. Dohi and R. Kikinis, Eds., 2002.

[52] T. R. Coles, D. Meglan, and N. W. John, "The role of haptics in medical training simulators: A survey of the state of the art," *IEEE Transactions on Haptics*, vol. 4, no. 1, pp. 51–66, 2011.

[53] C. G. L. Cao, M. Zhou, D. B. Jones, and S. D. Schwaitzberg, "Can surgeons think and operate with haptics at the same time?" *Journal of Gastrointestinal Surgery*, vol. 11, no. 11, pp. 1564–1569, Nov 2007.

[54] W. Bargar, A. Bauer, and M. Borner, "Primary and revision total hip replacement using the robodoc system," *Clinical Orthopaedics and Related Research*, vol. 354, pp. 82–91, 1998.

[55] M. Jakopec, S. Harris, F. Rodriquez y Baena, P. Gomes, J. Cobb, and B. Davies, "The first clinical application of a hands-on robotic knee surgery system," *Computer Aided Surgery*, vol. 6, pp. 329–339, 2001.

[56] A. Bettini, S. Land, A. Okamura, and G. Hager, "Vision assisted control for manipulation using virtual fixtures," *Robotics, IEEE transactions on*, vol. 20, no. 6, pp. 953–966, 2004.

[57] O. Schneider, J. Troccaz, O. Chavanon, and D. Blin, "Padyc: a synergistic robot for cardiac puncturing," in *Robotics and Automation. IEEE Conference on.* IEEE, 2000.

[58] G. Megali, O. Tonet, C. Stefanini, M. Boccadoro, V. Papaspyropoulos, L. Angelini, and P. Dario, "A computer-assisted robotic ultrasound-guided biopsy system for video-assisted surgery," 2001, pp. 343–350.

[59] R. J. Webster, J. S. Kim, N. J. Cowan, G. S. Chirikjian, and A. M. Okamura, "Nonholonomic modeling of needle steering," *The International Journal of Robotics Research*, vol. 25, no. 5-6, pp. 509–525, 2006.

[60] J. P. Swensen and N. J. Cowan, "Torsional dynamics compensation enhances robotic control of tip-steerable needles," in *2012 IEEE International Conference on Robotics and Automation*, 2012, pp. 1601–1606.

[61] M. Abayazid, R. J. Roesthuis, R. Reilink, and S. Misra, "Integrating deflection models and image feedback for real-time flexible needle steering," *IEEE Transactions on Robotics*, vol. 29, no. 2, pp. 542–553, 2013.

[62] J. A. Engh, D. S. Minhas, D. Kondziolka, and C. N. Riviere, "Percutaneous intracerebral navigation by duty-cycled spinning of flexible bevel-tipped needles," *Neurosurgery*, vol. 67, no. 4, pp. 1117–1123, 2010.

[63] D. S. Minhas, J. A. Engh, M. M. Fenske, and C. N. Riviere, "Modeling of needle steering via duty-cycled spinning," in *2007 29th Annual International*

Conference of the IEEE Engineering in Medicine and Biology Society, 2007, pp. 2756–2759.

[64] G. J. Vrooijink, M. Abayazid, S. Patil, R. Alterovitz, and S. Misra, "Needle path planning and steering in a three-dimensional non-static environment using two-dimensional ultrasound images," *The International Journal of Robotics Research*, vol. 33, no. 10, pp. 1361–1374, 2014.

[65] D. C. Rucker, I. Robert J. Webster, G. S. Chirikjian, and N. J. Cowan, "Equilibrium conformations of concentric-tube continuum robots," *The International Journal of Robotics Research*, vol. 29, no. 10, pp. 1263–1280, 2010.

[66] P. E. Dupont, J. Lock, B. Itkowitz, and E. Butler, "Design and control of concentric-tube robots," *IEEE Transactions on Robotics*, vol. 26, no. 2, pp. 209–225, 2010.

[67] F. Orlando, M. Kumar, K. Franz, B. Kohn, P. Hutapea, Y. Zhao, A. Dicker, Y. Yu, and T. Podder, "Control of shape memory alloy actuated flexible needle using multimodal sensory feedbacks," in *Jounal of Automation and Control Engineering*, vol. 3, pp. 428–434, 2015.

[68] S. C. Ryu, Z. F. Quek, J. S. Koh, P. Renaud, R. J. Black, B. Moslehi, B. L. Daniel, K. J. Cho, and M. R. Cutkosky, "Design of an optically controlled mr-compatible active needle," *IEEE Transactions on Robotics*, vol. 31, no. 1, pp. 1–11, 2015.

[69] E. Ayvali and J. P. Desai, "Accurate in-plane and out-of-plane ultrasound-based tracking of the discretely actuated steerable cannula," in *2014 IEEE International Conference on Robotics and Automation (ICRA)*, 2014, pp. 5896–5901.

[70] T. R. Wedlick and A. M. Okamura, "Characterization of pre-curved needles for steering in tissue," in *2009 Annual International Conference of the IEEE Engineering in Medicine and Biology Society*, 2009, pp. 1200–1203.

[71] D. Glozman and M. Shoham, "Image-guided robotic flexible needle steering," *IEEE Transactions on Robotics*, vol. 23, no. 3, pp. 459–467, 2007.

[72] S. P. DiMaio and S. E. Salcudean, "Needle steering and motion planning in soft tissues," *IEEE Transactions on Biomedical Engineering*, vol. 52, no. 6, pp. 965–974, 2005.

[73] V. G. Mallapragada, N. Sarkar, and T. K. Podder, "Robot-assisted real-time tumor manipulation for breast biopsy," *IEEE Transactions on Robotics*, vol. 25, no. 2, pp. 316–324, 2009.

[74] C. Rossa, N. Usmani, R. Sloboda, and M. Tavakoli, "A hand-held assistant for semiautomated percutaneous needle steering," *IEEE Transactions on Biomedical Engineering*, vol. 64, no. 3, pp. 637–648, 2017.

[75] C. Simone and A. M. Okamura, "Modeling of needle insertion forces for robot-assisted percutaneous therapy," in *Proceedings 2002 IEEE International Conference on Robotics and Automation (Cat. No.02CH37292)*, vol. 2, 2002, pp. 2085–2091.

[76] A. M. Okamura, C. Simone, and M. D. O'Leary, "Force modeling for needle insertion into soft tissue," *IEEE Transactions on Biomedical Engineering*, vol. 51, no. 10, pp. 1707–1716, 2004.

[77] H. M. Langevin, D. L. Churchill, J. R. Fox, G. J. Badger, B. S. Garra, and M. H. Krag, "Biomechanical response to acupuncture needling in humans," *Journal of Applied Physiology*, vol. 91, no. 6, pp. 2471–2478, 2001.

[78] M. C. Lewis, J. P. Lafferty, M. S. Sacks, V. S. Pallares, and M. TerRiet, "How much work is required to puncture dura with tuohy needles?" *BJA: British Journal of Anaesthesia*, vol. 85, no. 2, pp. 238–241, 2000.

[79] Y. Kobayashi, T. Sato, and M. G. Fujie, "Modeling of friction force based on relative velocity between liver tissue and needle for needle insertion simulation," in *2009 Annual International Conference of the IEEE Engineering in Medicine and Biology Society*, 2009, pp. 5274–5278.

[80] F. Mueller, "Biomechanical test report on hsw fine-ject needles," Tech. Rep, Tech. Rep., 2011.

[81] M. Mahvash and P. E. Dupont, "Fast needle insertion to minimize tissue deformation and damage," in *2009 IEEE International Conference on Robotics and Automation*, 2009, pp. 3097–3102.

[82] J. T. Hing, A. D. Brooks, and J. P. Desai, "Reality-based needle insertion simulation for haptic feedback in prostate brachytherapy," in *Robotics and Automation, 2006. ICRA 2006. Proceedings 2006 IEEE International Conference on*, 2006, pp. 619–624.

[83] D. van Gerwen, J. Dankelman, and J. van den Dobbelsteen, "Needle-tissue interaction forces - a survery of experimental data," *Medical Engineering and Physics*, vol. 34, no. 6, pp. 665–680, 2012.

[84] L. Barbe, B. Bayle, M. de Mathelin, and A. Gangi, "In vivo model estimation and haptic characterization of needle insertions," *The International Journal of Robotics Research*, vol. 26, no. 11-12, pp. 1283–1301, 2007.

[85] Y. Kobayashi, A. Onishi, T. Hoshi, K. Kawamura, and M. G. Fujie, "Modeling of conditions where a puncture occurs during needle insertion considering probability distribution," in *2008 IEEE/RSJ International Conference on Intelligent Robots and Systems*, 2008, pp. 1433–1440.

[86] S. Elayaperumal, J. H. Bae, B. L. Daniel, and M. R. Cutkosky, "Detection of membrane puncture with haptic feedback using a tip-force sensing needle," in *2014 IEEE/RSJ International Conference on Intelligent Robots and Systems*, 2014, pp. 3975–3981.

[87] J. H. Bae, A. K. Han, C. J. Ploch, B. L. Daniel, and M. R. Cutkosky, "Haptic feedback of membrane puncture with an mr-compatible instrumented needle and electroactive polymer display," in *2017 IEEE World Haptics Conference (WHC)*, 2017, pp. 54–59.

[88] S. E. Song, N. B. Cho, G. Fischer, N. Hata, C. Tempany, G. Fichtinger, and I. Iordachita, "Development of a pneumatic robot for mri-guided transperineal prostate biopsy and brachytherapy: New approaches," in *2010 IEEE International Conference on Robotics and Automation*, 2010, pp. 2580–2585.

[89] R. Seifabadi, N. B. J. Cho, S.-E. Song, J. Tokuda, N. Hata, C. M. Tempany, G. Fichtinger, and I. Iordachita, "Accuracy study of a robotic system for mri-guided prostate needle placement," *The International Journal of Medical Robotics and Computer Assisted Surgery*, vol. 9, no. 3, pp. 305–316, 2013.

[90] R. Seifabadi, S.-E. Song, A. Krieger, N. B. Cho, J. Tokuda, G. Fichtinger, and I. Iordachita, "Robotic system for mri-guided prostate biopsy: feasibility of teleoperated needle insertion and ex vivo phantom study," *International journal of computer assisted radiology and surgery*, vol. 7, no. 2, pp. 181–190, 2011.

[91] J. Tokuda, S. Song, G. Fischer, I. Iordachita, R. Seifabadi, N. Cho, K. Tuncali, G. Fichtinger, C. Tempany, and N. Hata, "Preclinical evaluation of an mri-compatible pneumatic robot for angulated needle placement in transperineal prostate interventions," *International Journal of Computer Assisted Radiology and Surgery*, 2012.

[92] H. Su, W. Shang, G. Cole, G. Li, K. Harrington, A. Camilo, J. Tokuda, C. Tempany, N. Hata, and G. Fischer, "Piezoelectrically actuated robotic system for mri-guided prostate percutaneous therapy," *Mechatronics, IEEE/ASME Transactions on*, vol. 20, no. 4, pp. 1920–1932, 2015.

[93] W. Shang, H. Su, G. Li, and G. S. Fischer, "Teleoperation system with hybrid pneumatic-piezoelectric actuation for mri-guided needle insertion with haptic feedback," in *Intelligent Robots and Systems (IROS), 2013 IEEE/RSJ International Conference on*. IEEE, 2013, pp. 4092–4098.

[94] N. Patel, T. Katwijk, P. Moreira, W. Shang, S. Misra, and G. Fischer, "Closed-loop asymmetric-tip needle teering under continuous intraoperative mri guidance," in *Engineering in Medicine and Biology 2015 (EMBC 2015). IEEE International Conference on*. IEEE, 2015, pp. 4869–4874.

[95] M. Li, B. Gonenc, K. Kim, W. Shang, and I. Iordachita, "Development of an mri-compatible needle driver for in-bore prostate biopsy," in *2015 International Conference on Advanced Robotics (ICAR)*, 2015, pp. 130–136.

[96] R. J. Cohrs, T. Martin, P. Ghahramani, L. Bidaut, P. J. Higgins, and A. Shahzad, "Translational medicine definition by the european society for

translational medicine," *New Horizons in Translational Medicine*, vol. 2, no. 3, pp. 86–66, 2014.

[97] E. M. Goldblatt and W.-H. Lee, "From bench to bedside: the growing use of translational research in cancer medicine," *American journal of translational research*, vol. 2, no. 1, p. 1, 2010.

[98] P. Nevoux, A. Ouzzane, H. U. Ahmed, M. Emberton, R. Montironi, J. C. Presti Jr, and A. Villers, "Quantitative tissue analyses of prostate cancer foci in an unselected cystoprostatectomy series," *BJU international*, vol. 110, no. 4, pp. 517–523, 2012.

[99] S. Eslami, W. Shang, G. Li, N. Patel, G. S. Fischer, J. Tokuda, N. Hata, C. M. Tempany, and I. Iordachita, "In-bore prostate transperineal interventions with an mri-guided parallel manipulator: system development and preliminary evaluation," *The International Journal of Medical Robotics and Computer Assisted Surgery*, 2015.

[100] G. R. Sutherland, I. Latour, A. D. Greer, T. Fielding, G. Feil, and P. Newhook, "An image-guided magnetic resonance-compatible surgical robot," *Neurosurgery*, vol. 62, no. 2, pp. 286–293, 2008.

[101] R. Kokes, K. Lister, R. Gullapalli, B. Zhang, A. MacMillan, H. Richard, and J. P. Desai, "Towards a teleoperated needle driver robot with haptic feedback for rfa of breast tumors under continuous mri," *Medical image analysis*, vol. 13, no. 3, pp. 445–455, 2009.

[102] H. Su, M. Zervas, C. Furlong, and G. S. Fischer, "A miniature mri-compatible fiber-optic force sensor utilizing fabry-perot interferometer," in *MEMS and Nanotechnology, Volume 4*. Springer, 2011, pp. 131–136.

[103] Y. Park, S. Elayaperumal, S. Ryu, B. Daniel, R. Black, B. Moslehi, and M. Cutkosky, "Mri-compatible haptics: Strain sensing for real-time estimation of three dimensional needle deflection in mri environments," in *International Society for Magnetic Resonance in Medicine (ISMRM), 17th Scientific Meeting and Exhibition*, 2009.

[104] G. Cole, J. Pilitsis, and G. S. Fischer, "Design of a robotic system for mri-guided deep brain stimulation electrode placement," in *2009 IEEE International Conference on Robotics and Automation*, 2009, pp. 4450–4456.

[105] G. Li, H. Su, G. A. Cole, W. Shang, K. Harrington, A. Camilo, J. G. Pilitsis, and G. S. Fischer, "Robotic system for mri-guided stereotactic neurosurgery," *IEEE Transactions on Biomedical Engineering*, vol. 62, no. 4, pp. 1077–1088, 2015.

[106] C. Nycz, R. Gondokaryono, P. Carvalho, N. Patel, M. Wartenberg, J. Pilitsis, and G. Fischer, "Mechanincal validation of an mri compatible stereotactic neurosurgery robot in preparation for pre-clinical trials," in *2017 IEEE/RSJ International Conference on Intelligent Robots and Systems*, 2017.

[107] A. Welford, "Choice reaction time: Basic concepts," *Reaction times*, pp. 73–128, 1980.

[108] A. R. Peon and D. Prattichizzo, "Reaction times to constraint violation in haptics: comparing vibration, visual and audio stimuli," in *2013 World Haptics Conference (WHC)*, 2013, pp. 657–661.

[109] N. Hungr, J.-A. Long, V. Beix, and J. Troccaz, "A realistic deformable prostate phantom for multimodal imaging and needle-insertion procedures," *Medical Physics*, vol. 39, no. 4, pp. 2031–2041, 2012.

[110] B.-M. Ahn, J. Kim, L. Ian, K.-H. Rha, and H.-J. Kim, "Mechanical property characterization of prostate cancer using a minimally motorized indenter in an ex vivo indentation experiment," *Urology*, vol. 76, no. 4, pp. 1007 – 1011, 2010.

[111] K. Hoyt, B. Castaneda, M. Zhang, P. Nigwekar, P. di Sant'Agnese, D. R. JV Joseph and, J Strang, and J. Parker, "Tissue elasticity properties as biomarkers for prostate cancer," *Cancer Biomarkers*, vol. 4, pp. 213–225, 2011.

[112] T. Podder, D. Clark, J. Sherman, D. Fuller, E. Messing, D. Rubens, J. Strang, R. Brasacchio, L. Liao, W.-S. Ng, and Y. Yu, "In vivo motion and force measurement of surgical needle intervention during prostate brachytherapy," *Medical Physics*, vol. 33, no. 8, 2006.

[113] J. Tokuda, G. S. Fischer, X. Papademetris, Z. Yaniv, L. Ibanez, P. Cheng, H. Liu, J. Blevins, J. Arata, A. J. Golby, T. Kapur, S. Pieper, E. C. Burdette, G. Fichtinger, C. M. Tempany, and N. Hata, "Openigtlink: an open network protocol for image-guided therapy environment," *The International Journal of Medical Robotics and Computer Assisted Surgery*, vol. 5, no. 4, pp. 423–434, 2009.

[114] G. Farneback, "Two-frame motion estimation based on polynomial expansion," *Image Analysis*, pp. 363–370, 2010.

[115] G. Li, "Robotic system development for precision mri-guided needle-based interventions," *PhD Dissertation, Dept. of Mechanical Engineering, WPI*, 2016.

[116] R. Tsumura, Y. Takishita, Y. Fukushima, and H. Iwata, "Histological evaluation of tissue damage caused by rotational needle insertion," in *2016 38th Annual International Conference of the IEEE Engineering in Medicine and Biology Society (EMBC)*, 2016, pp. 5120–5123.

[117] J. Tokuda, K. Tuncali, I. Iordachita, S.-E. Song, A. Fedorov, S. Oguro, A. Lasso, F. M. Fennessy, C. M. Tempany, and N. Hata, "In-bore setup and software for 3t mri-guided transperineal prostate biopsy," *Physics in Medicine and Biology*, vol. 57, no. 18, pp. 5823–5480, 2012.

[118] D. Stoianovici, C. Jun, S. Lim, P. Li, D. Petrisor, S. Fricke, K. Sharma, and K. Cleary, "Multi-imager compatible, mr safe, remote center of motion needle-guide robot," *IEEE Transactions on Biomedical Engineering*, vol. PP, no. 99, pp. 1–1, 2017.

[119] D. Preston, "Magnetic resonance imaging (mri) of the brain and spine: Basics," 2006.

[120] N. E. M. A. Std., "Determination of signal-to-noise ratio (snr) in diagnostic magnetic resonance imaging."

[121] R. C. Susil, J. H. Anderson, and R. H. Taylor, "A single image registration method for ct guided interventions," in *Medical Image Computing and Computer-Assisted Intervention – MICCAI'99*, C. Taylor and A. Colchester, Eds., 1999.

[122] G. S. Fischer, I. Iordachita, C. Csoma, J. Tokuday, P. W. Mewesy, C. M. Tempanyy, N. Hatay, and G. Fichtinger, "Pneumatically operated mri-compatible needle placement robot for prostate interventions," in *2008 IEEE International Conference on Robotics and Automation*, 2008, pp. 2489–2495.

[123] G. S. Fischer, A. Krieger, I. Iordachita, C. Csoma, L. L. Whitcomb, and G. Fichtinger, "Mri compatibility of robot actuation techniques – a comparative study," in *Medical Image Computing and Computer-Assisted Intervention – MICCAI 2008*, 2008, pp. 509–517.